University of Naples "Federico II"
Physics Department

degree of
Doctor of Philosophy
in
"Fundamental and Applied Physics"

December 2005

Ultrashort pulsed laser ablation of solid targets

Dr. Marco Vitiello

To life,

a so strange and

inconceivable mystery....

TABLE OF CONTENTS

CONCLUSIONS

APPENDIX A

Magnetic films of nanoparticles by ultrashort pulsed laser deposition

INTRODUCTION

Ultrashort, sub-picosecond pulsed laser ablation technique is currently attracting a great deal of attention both for fundamental physics and for technological applications.

The first investigations on the interaction of Ti:sapphire femtosecond (fs) laser pulses with solid targets were mainly devoted to the study of the modifications of irradiated samples. These studies are still establishing fs laser ablation as the state-of-art technique for optimal control of material removal, due to its peculiarity to process virtually any material with high precision and minimal collateral damage. In a number of applications (micromachining, metal processing, surgical operation, and so on) advantages over nanosecond (ns) and picosecond (ps) laser pulses have been already demonstrated.

Ultrafast pulses offer significant potential advantage over conventional ns laser sources. The advantage of using fs radiation lies in:

i) the ability to decouple the ablated volume from the adjoining target mass.

ii) the lowering of threshold ablation fluence by a factor of about 10 compared to ns pulses; this means that even the most intractable materials, such as refractory metals, can be cleanly and congruently ablated.

A key benefit of ultrashort laser pulses lies in its ability to deposit energy into a material in a very short time period, before thermal diffusion can take place. Following linear or multiphoton absorption of the laser energy, electron temperatures can be quickly raised up to many thousands of degree Kelvin. With the subsequent energy transfer from the electron subsystem to the atomic lattice, material removal, ablation and plasma formation occur, as briefly discussed in chapter I. At laser pulse durations shorter than the typical electron to lattice relaxation times (about some ps), the system behaves roughly the same and the main properties of the plume are quite independent from material and laser parameters; then, we may say to be in the “ultrashort” regime.

On the contrary, for ns laser pulses ablation occurs from both the melted and the vapour phases, leading also to emission of particulate and liquid *micro-droplets*. Moreover, the long lasting material emission and the longer pulse length lead to laser-vapour interaction, limiting the control on the properties of the ablated particles. For ultrashort pulses, on the other hand, the ablation wave actually precedes the thermal relaxation wave and ablation occurs with minimal collateral damage to the target.

In spite of its enormous potentiality, there has been little work on the characterization of laser produced plasma and plume evolution as well as on film growth using ultrashort laser ablation, probably because of its relative infancy. Nanosecond lasers continue to prevail in Pulsed Laser Deposition technique due to their ease of handling and relative low cost. Notwithstanding, the recent advances in ultrashort laser technology have opened up the possibility to use easier to operate ultrashort tabletop laser sources, particularly attractive to study the laser-solid interaction process in the range of concern to ultrashort laser ablation and deposition.

Thus, one of the main goals of the present thesis is to elucidate some of the fundamental aspects regarding the laser-matter interaction in the not so widely studied ultrashort pulse regime. To do this, several experimental techniques as Optical Emission Spectroscopy, Langmuir probe, Fast Photography and Atomic Force Microscopy were employed to characterize the ultrashort laser ablated plumes from several, different target materials among metals and semiconductors, as reported in chapter III.

The experimental investigations revealed the presence in the ultrashort laser ablated plumes of nanoparticles with mean radii of about 10-20 nm, whatever the target material is. Thus, in addition to the timeliness of ultrashort laser ablation as a novel material processing technique and to the extreme interest around the physical mechanisms governing the process, the understanding of nanoparticles production mechanisms in vacuum attracted great attention and became also one of the main goals of the present thesis.

In fact, nanoparticles production by laser ablation technique is currently performed by means of ns laser systems, just by letting the plume to expand in an inert gas atmosphere: the collisions between the ablated atoms and the background gas give rise to vapour condensation and, then, to cluster formation. On the contrary, ultrashort laser ablation provides nanoparticles directly in vacuum without any backing atmosphere, thus appearing as an extremely versatile technique to particles production.

Actually, as we already mentioned, during nanosecond laser ablation, under suitable experimental conditions, production of *micrometric* particles as liquid droplets coming from the melted target material has been frequently reported, while Atomic Force Microscopy (AFM) allowed us to check the actual *nanometric* character of the aggregates produced by ultrashort pulses. The limited sizes and the quite narrow size distributions of nanoparticles found for each investigated material and experimental condition confirm the extreme novelty of the process and open new perspectives in the field of laser-matter interaction.

Moreover, all the techniques currently employed to synthesize nanoparticles require to find for each material a set of optimal experimental parameters to get an efficient production, thus being strongly material dependent; for instance, with ns laser ablation technique is necessary to achieve time by time the right balance between the gas pressure and the target to deposition substrate distance, while chemical and electrochemical techniques need of specific reagents and reactions for a good material processing. On the contrary, as evidenced by both optical measurements and AFM, ultrashort laser ablation provides nanoclusters directly from the target material, in vacuum, without any further experimental improvement, thus turning out to be an universal route for nanoparticles production from any target material (metals, semiconductors, multicomponents and so on) and appearing as a very powerful and promising technique for technological applications.

Apart from the wide experimental investigations, some numerical techniques were employed to study the processes of material excitation and removal under ultrashort laser irradiation. In particular, Molecular Dynamics technique was used in collaboration with the group of Prof. Petar Atanasov of the Institute of Electronics of the Bulgarian Academy of Sciences to simulate the ultrashort laser ablation process. The model was able to reproduce the main features of ultrashort laser ablation, as nanoparticles ejection and expansion as well as the presence in the plume of several, different species (ions, atoms and nanoparticles), thus turning out to be a valid instrument to study the processes occurring during ultrashort pulsed laser ablation in vacuum and to get a theoretical explanation of our experimental results.

On the other hand, a Monte Carlo approach was developed to get the spatial distribution of energy inside the bulk material as a consequence of both linear absorption and electron thermal diffusion mechanisms. The calculated spatial distributions were then used to predict the subsequent relaxation, through adiabatic thermodynamic pathways, of specific areas of the target during plume expansion, thus revealing the co-presence of several, different ablation mechanisms at the fluences of concern here.

Finally, it clearly turns out that a deep characterization of the plume properties and dynamics is of great present interest both to elucidate the main properties of all the ejected particles (ions, atoms and nanoparticles) and to shed a light on their formation mechanisms, as widely reported in the next chapters.

In chapter I a general overview of the theoretical background is reported, while chapter II is dedicated to the description of the experimental apparatus. Chapters III and IV are devoted to the presentation of the main experimental and numerical results, respectively. Finally,

Appendix A briefly deals with the main properties of the nanoparticles films produced during the present thesis, thus underlining the extreme potentiality of ultrashort laser ablation as a deposition technique of new materials for nanoscience applications.

CHAPTER I

Ultrashort pulsed laser ablation: mechanisms and processes

The processes governing ultrashort pulsed laser ablation are not completely understood at the moment. Actually, several studies on the mechanisms of laser absorption and material excitation, as well as its removal and expansion, has been done, but none of them can be considered exhaustive.

This chapter describes the basic processes occurring during the irradiation of solid targets with ultrashort, subpicosecond laser pulses. The detailed course of the very complex phenomenon occurring during the interaction depends strongly on the parameters of the laser pulse and the target material. Typical intensities used in the femtosecond laser ablation and deposition experiments are in the range of 10^{12}-10^{14} W/cm^2. At these intensities, the basic processes occurring during laser ablation such as excitation, melting and material removal are temporally separated allowing a separate description of each of them.[1] Excitation takes place on a timescale comparable with the duration of the laser pulse (<< 1ps), as a consequence of absorption of photons by the electronic subsystem of the material. This stage is then followed by melting, which roughly occur in the picosecond regime, and by the removal of material (ablation), whose establishment may require up to several nanoseconds. The expansion of the formed plasma plume, then, follows on much longer timescales.

Consequently, following ref. 1, in the next sections we describe separately these three regimes, which can be considered temporally separated: 1) optical excitation of the system; 2) lattice modifications; 3) material removal and expansion. Each of them is discussed in the framework of several competing mechanisms, which time by time come into play for metals and/or semiconductors.

I.1. **Absorption of the laser light and excitation of the system.**

I.1.1. *Metals.*

For metals, absorption and reflection of ultrashort light pulses obey the laws of linear metal optics up to intensities of 10^{15} W/cm^2.[2,3] Optical absorption is usually dominated by free carrier

absorption, i.e. electrons in the conduction band absorb photons through Inverse Bremsstrahlung and gain energy. In the visible and infrared spectral region, for most metals the linear absorption coefficient α is in the range (5-10)×10^5 cm^{-1}, resulting in an optical absorption depth α^{-1} of the order of ≈10-20 nm. Nevertheless, in some cases the hot, non-equilibrium electrons can penetrate deeply into the material due to ballistic transport.[4] For example, in the case of gold the non-equilibrium electrons have ballistic velocities of the order of 10^6 m/s leading to a ballistic range of ≈100-120 nm for ≈100 fs pulses.

The absorption is responsible for the generation of a highly non-equilibrium state of excited electrons, which relax by electron–electron collisions on a timescale of typically few hundreds of fs determined by the collision rate, governed by the density of states (DOS) at the Fermi level. Consequently, the conversion takes much longer for noble metals than for transition metals.[4] Several theoretical and experimental studies reported the relaxation of an optically excited non-Fermi-Dirac distribution to a hot Fermi-Dirac distribution through e-e scattering.[5,6] This picture assumes that electrons first thermalize among themselves and subsequently lose energy to the lattice. That is strictly true as the absorbed energy density increases. In fact, the higher is the delivered energy the faster is the relaxation process, owing to several factors. First, if a larger energy density is deposited into the material, the temperature of the thermal part of the distribution increases more rapidly. This, in turn, increases the number of available electrons with which the non-thermal electrons can scatter, that is, increases the scattering rate. Moreover, as the thermalization process between the rapidly heating thermal component and the non-thermal part of the distribution goes on, the non-thermal part becomes more and more composed only of the higher energy electrons, which have the shortest energy relaxation time. All these factors lead to a decrease in the thermalization time as the excitation density increases.

When an equilibrium electron temperature (T_e) and a Fermi distribution are established, the diffusion of hot electrons is driven by the temperature gradient. Due to the relatively small electronic heat capacity, peak electronic temperatures of thousands of Kelvin above the equilibrium melting point can be reached. Ballistic transport of non-thermalized electrons and diffusive transport of thermalized electrons into the bulk take place,[7] while simultaneously heat is transferred from the electronic system to the initially cold lattice by electron-phonon coupling on a timescale of few picoseconds. This stage is usually described by the Two Temperature Model (TTM),[8] which consists of the diffusion equations for the electrons and lattice, coupled by a term proportional to the temperature difference of the two reservoirs (electrons and lattice) multiplied by the strength of the electron–phonon interaction, g. The assumption that the

electron–phonon coupling can be reduced to one linear coupling term of the form $g(T_e - T_l)$ is the essence of the model, which can be written as:

$$C_e \frac{\partial T_e}{\partial t} = -\frac{\partial}{\partial z}\left(k_e \frac{\partial T_e}{\partial z} \right) - g(T_e - T_l) + S(z,t)$$
$$C_l \frac{\partial T_l}{\partial t} = -\frac{\partial}{\partial z}\left(k_l \frac{\partial T_l}{\partial z} \right) + g(T_e - T_l) \qquad (1.1)$$
$$S(z,t) = I(t) A \alpha \exp(-\alpha z)$$

where C_e, k_e and C_l, k_l are the electron and lattice capacity and thermal conductivity, respectively, while *S(z, t)* is the laser heating source term, characterized by the laser intensity *I(t)*, the surface absorptivity *A* and the material absorption coefficient α. Since heat diffuses much faster through the electron subsystem, in eq. (1.1) the lattice thermal conductivity can be neglected.

The two-temperature model (TTM) can be successfully applied to predict threshold fluences for melting. Even the ballistic motion can be incorporated into the TTM by altering the source term.[4] TTM essentially consists of a system of coupled differential equations, which in general cannot be solved analytically. It is necessary to separately analyze the stages of electron heat diffusion and electron-lattice coupling, due to the almost different timescales which characterize them; the set of assumptions imposed to solve the system determines time by time the applicability of the specific model.

Nolte et al. proposed an analytical solution to the TTM equations by splitting the laser-matter interaction process in two distinct stages: material excitation during the laser irradiation and material relaxation at the end of the laser pulse of duration τ_L.[9] During the first stage, they considered the temporal evolution of the electron temperature distribution to follow the laser temporal profile, while considering its spatial behaviour to be determined by both optical absorption and electron heat diffusion. On the other hand, the lattice temperature distribution is assumed to be linearly linked to the electron temperature distribution. Thus, they looked for the following solution

$$T_e(z,t) = \exp\left(\frac{t}{\tau_L} \right) \Omega(z)$$
$$\Omega(z) = a \exp(-\alpha z) + b \exp(-\beta z) \qquad (1.2)$$
$$T_l = \kappa T_e$$

with the assumption that the laser intensity grows exponentially with time ($t < 0$) as $I(t) = I_0 \exp(t/\tau_L)$, before being switched off at $t = 0$. Here *a*, *b*, κ and β are unknown parameters which can be determined by imposing initial and boundary conditions (at the surface $z = 0$). As a result, the decay parameter β is just the inverse of the electron thermal penetration depth, $\Lambda = \beta^{-1} = \sqrt{D\tau_{eff}}$, being $D = k_e / C_e$ the electron thermal diffusivity and τ_{eff} some electron effective relaxation time (for ultrashort pulses, it is just the characteristic time for thermal equilibration between the electron bath and the laser heating source).

At the end of the laser pulse, the system evolution is modelled through the TTM equations by neglecting at first the electron thermal diffusion. This gives the solutions ($t > 0$):

$$
\begin{aligned}
T_e(z,t) &= T_{eq} + \Delta T \frac{\tau_l}{\tau_e + \tau_l} \exp\left(-\frac{t}{\tau_{eq}}\right) \\
T_l(z,t) &= T_{eq} + \Delta T \frac{\tau_e}{\tau_e + \tau_l} \exp\left(-\frac{t}{\tau_{eq}}\right) \\
T_{eq} &= \frac{\tau_L \tau_{eq}}{\tau_l \tau_{eff}} T_e(z,0) = \frac{F_a}{C_l} \frac{\tau_l}{\tau_e + \tau_l} \frac{\beta^2 \alpha^2}{\beta^2 + \alpha^2} \left[\alpha^{-1} \exp(-\alpha z) - \beta^{-1} \exp(-\beta z)\right] \\
\Delta T &= T_e(z,0) - T_l(z,0) \\
\tau_{eq} &= \frac{\tau_e \tau_l}{\tau_e + \tau_l}
\end{aligned}
\qquad (1.3)
$$

where $\tau_e = C_e / g$ and $\tau_l = C_l / g$ are the electron cooling and the lattice heating times, respectively. Here, τ_{eq} could be considered as a characteristic timescale of the thermal equilibration between the electron and lattice subsystems, while T_{eq} clearly represents their final equilibration temperature. To allow for the electron thermal diffusion after the laser pulse, Nolte et al. suggested to phenomenologically replace τ_{eff} with $\tau_a = \tau_{eff} + \tau_{eq}$ in Eq. (1.3).

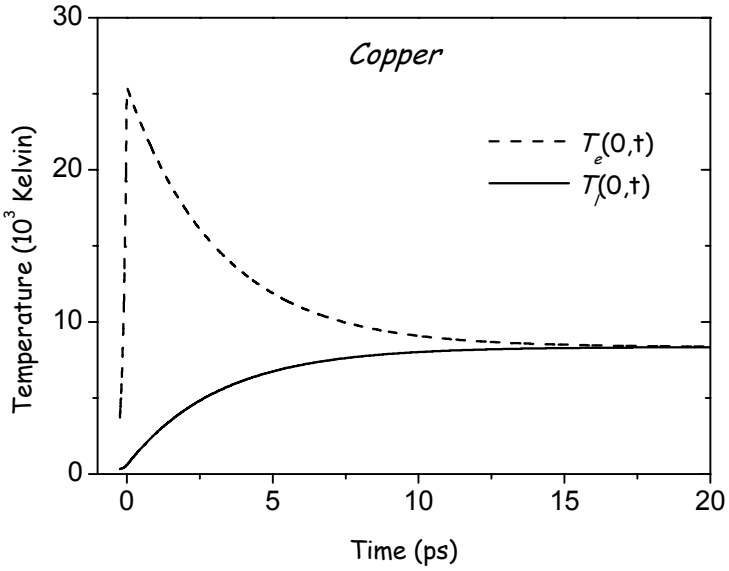

Fig. 1.1: Temporal distribution of electron (T_e) and lattice (T_l) surface temperature for a copper target irradiated by a 120 fs, 800 nm pulse at a laser intensity I_0=5x10^{12} W/cm^2.

In Fig. 1.1, the surface electron and lattice temperature behaviour in time is shown, calculated by joining at $t = 0$ the solutions of Eqs. (1.2) and (1.3), in the case of a copper target for a laser intensity of $I_0 = 5\times10^{12}$ W/cm^2. Such curves strongly depend on electron conductivity and, first of all, on the strength of the *e-ph* coupling constant *g*. The higher is the electron conductivity, the lower is the peak surface electron temperature due to a more efficient electron thermal diffusion into the bulk material. On the other hand, a higher value of *g* leads to a faster equilibration dynamics between the lattice and the electron baths towards the common equilibrium temperature. For instance, in Fig. 1.2 a comparison between the electron and lattice surface temperatures evolution is reported, calculated in the same conditions of Fig 1.1, for a nickel and a gold target. The transfer of energy to the lattice takes a much longer time for gold than for nickel due to the different values of the *e-ph* coupling constant ($g_{Ni}/g_{Au} \approx 18$). The material parameters used in Figs. 1.1 and 1.2 are taken from refs. 4, 10, and 11.

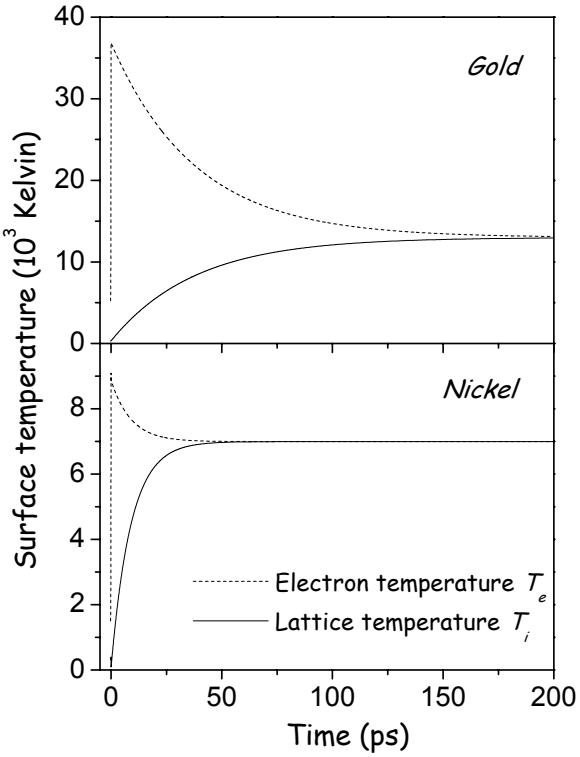

Fig. 1.2: Comparison between nickel and gold surface temperatures dynamics, in the same conditions as Fig. 1.1.

The behaviour predicted by Eq. (1.3) for the final equilibration temperature T_{eq} thus underlines the competition between two main absorption mechanisms of the laser light: an optical one, determined by the optical penetration depth α^{-1}, and a thermal one determined by the thermal penetration depth, which is related to the electron thermal conductivity. Such a predicted behaviour is useful to understand the presence of two different regimes in the dependence of the ablation depth/yield with respect to the laser fluence, which has been frequently reported by several experimental investigations.[9,10] When the optical penetration depth is greater than the thermal penetration depth (*low fluences*), ablation is driven by absorption into the skin depth; this corresponds to neglect in T_{eq} the second exponential trend. By increasing the laser fluence the thermal penetration depth increases up to become greater than the optical penetration depth. This second regime (*high fluences*) can be described by neglecting the first exponential trend in T_{eq}. Thus, Eqs. (1.2) and (1.3) give a quite comprehensive TTM description of the laser-solid interaction process during ultrashort laser light irradiation of metals, allowing a reasonable modelling and prediction of the different ablation regimes encountered by varying the energy delivered to the system.

It is worth noticing that the crucial point for any model of the ultrashort laser-solid interaction process lies in choosing the right approximations about the behaviour of the lattice and electrons parameters, such as heat capacities, thermal conductivities and so on, which are typically strongly temperature dependent.

I.1.2. *Semiconductors*

In semiconductors, the optical excitation of carriers can be pictured as follows. Initially, one-photon excitation generates electron-hole pairs by promoting electrons from the valence band to the conduction band through *interband* transitions, provided that the photon energy ($h\nu$) is higher than the material bandgap energy, E_g (*single photon absorption*). For intense laser pulses, one-photon excitation will saturate, due to band filling, but *multiphoton excitation* and *free-carrier absorption* (through *intraband* transitions) will create more, and more energetic, carriers.[12] Such processes are also the main absorption mechanisms when the photon energy is less than the material bandgap, $h\nu < E_g$. Since several photons must be absorbed "simultaneously," multiphoton absorption is not very probable compared with single photon absorption. However, its rate increases as I^N, where I is the laser intensity and N is the number of photons involved in the transition, thus becoming an important process when the exciting pulse is very short and intense. On the other hand, once carriers have been generated, they can absorb photons and move to higher energy states; this *free carrier absorption* increases the energy of the free carrier population but not the number of free carriers. The highly energetic carriers thus generated, in turn, can create additional carriers through *impact ionization*. In this process, which is due to Coulomb interactions between carriers, an excited electron loses energy and falls lower in the conduction band, while an excited hole could move higher in the valence band. As a result, the energy released excites an electron-hole pair. Therefore, impact ionization increases the number of free carriers but does not affect their total energy. Fig. 1.3 reports a schematics of the absorption processes just described.

Once the laser energy is delivered to the system, the carriers quickly relax through several processes occurring over different time scales. First of all, carrier-carrier scattering causes thermalization of the non-equilibrium electron distribution created by the laser pulse. This process occurs on a timescale of tens of fs and leads to a redistribution of the carriers energy over the conduction band. Afterwards, inelastic carrier-phonon scattering lowers the carriers energy and leads to the lattice heating. This process tipically occurs on a timescale of several ps

and, if the absorbed laser intensity is high enough, may induce a phase transition from the solid to the liquid, or directly to the vapour state.

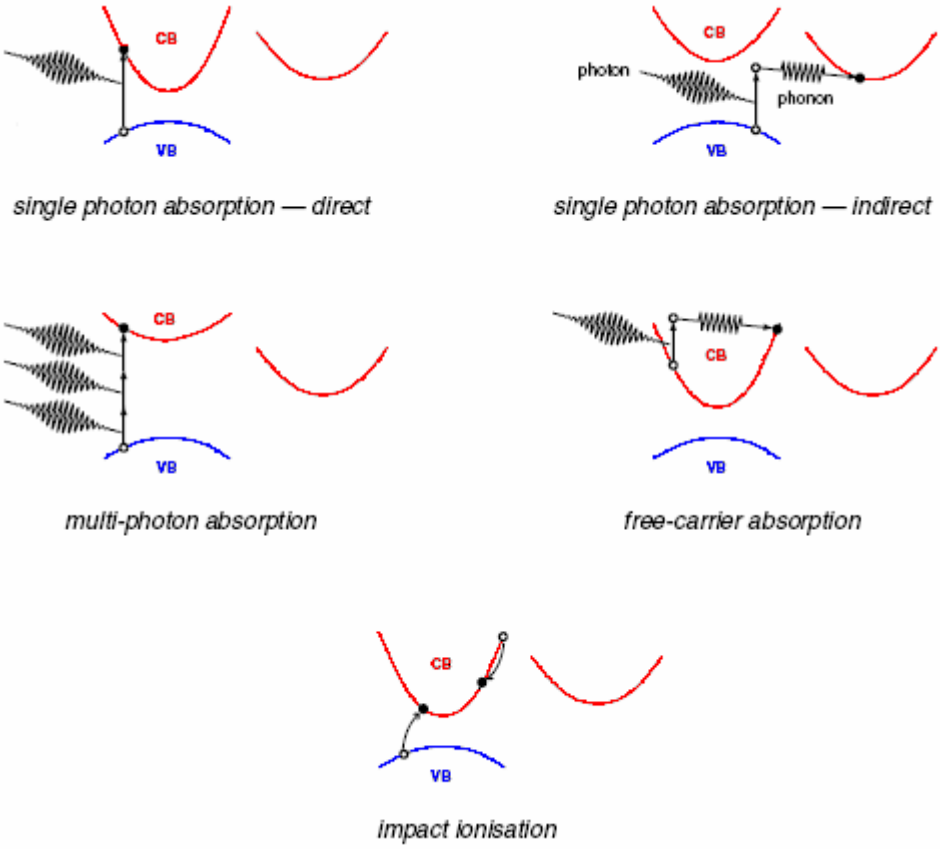

Fig. 1.3: Schematics of the absorption mechanisms occurring in a semiconductor after ultrashort pulsed laser irradiation. After ref. 13.

Carrier-lattice thermalization brings the temperatures of the free carriers and the lattice to the same value. The electrons form a Fermi-Dirac distribution around the Fermi level, whose width increases with temperature. However, if there is an energy gap, the free electrons and holes have Fermi-Dirac distributions about different Fermi levels. These distributions have the same temperature as that of the lattice, but there is still an excess of free carriers compared to the true thermodynamic equilibrium. These carriers can be removed in two ways: recombination of electrons and holes, or diffusion of carriers away from the photo-excited region. When an electron and hole recombine, the excess energy must be removed. There are several possible avenues for this energy, the primary ones being photon emission, other free carriers (*Auger recombination*) and defect or surface states. The first of these mechanisms is called *radiative recombination* while the last two are *non-radiative* processes.

At this point, it is worth noticing that during the years essentially two models were accounted for the experimentally observed phase transition induced by focusing intense laser radiation on semiconductors. The first one, known as the "thermal" model, describes the structural changes as a thermal melting process,[14] assuming that the hot equilibrated electron bath equilibrates with the lattice through electron phonon scattering; this, in turn, induces a thermal solid-to-liquid transition on a ps time scale. The other model, known as the "non-thermal" or "plasma" model, takes into account the destabilization of the covalent bonds due to the high electronic excitation. This process seems to induce an "ultrafast" melting, arising from a strong modification of the inter-atomic forces owing to laser-induced promotion of a large fraction (10% or more) of the valence electrons to the conduction band. The atoms, not screened any more, immediately begin to move and rapidly gain sufficient kinetic energy to induce a fast melting, lasting on a several hundreds of fs time scale — much faster than the several picoseconds required to convert the electronic energy into thermal motions. That is why, this mechanism is also referred as "electronic melting". This ultrafast photoexcitation can thus give the atoms enhanced mobility, without increasing their thermal energy; structural modifications can occur while the electronic and the lattice subsystems are not in thermal equilibrium with each other, even if each of them could be in internal quasi-equilibrium.

As experimentally demonstrated by several groups, these processes both characterize the ablation of semiconductors by ultrashort pulses, depending on the excitation energy.[15,16,17,18] These experiments validated previous theoretical studies,[14,19] which set a lower limit of approximately 10^{22} carriers/cm^3 to induce lattice instability; below this threshold, thermal effects result also to be important. During ultrashort irradiation of semiconductors materials, such a high carrier density is easily obtained owing to the extremely high laser intensity; for instance, in the case of GaAs a laser fluence (energy density on the target) of 0.15 J/cm^2 is required to induce ultrafast non thermal melting,[17] a value readily attainable by the common ultrashort laser sources available at the moment.

Normal thermal melting occurs heterogeneously by nucleation and growth of the liquid phase. The boundary separating the phases moves from the liquid into the solid. The times to melt a layer of solid material are relatively long, because the upper limit of the velocity of the solid–liquid interface should be of the order of the speed of sound. For example, it takes typically 50 to 100 ps to melt a 20 nm surface layer of silicon using picosecond laser pulses. On the contrary, non thermal melting due to surface instability occurs homogeneously, wherever the stability limit is exceeded.[17]

Because of the interplay of all these excitation and relaxation mechanisms, it is difficult to estimate the temporal evolution of the carrier density created by the laser pulse. It should be noted that, the reflectivity as well as the absorption coefficient change during the laser pulse irradiation as a consequence of the varying transient electron density. At the high intensities reached by focusing ultrashort laser radiation this can be also influenced by photo- and thermal emission of electrons from the target surface.[20,21] Energy balance equations for electrons and lattice subsystems, similar to the TTM diffusion equations but with the phonon excitation/relaxation separated into the optical and acoustic modes of the lattice response, have been used by Choi and Grigoropoulos in the case of a silicon target irradiated by 800 nm, ≈100 fs laser pulses. By solving this set of coupled equations, space and temporal evolutions of the electron and lattice temperatures for the first few ps of material evolution were obtained.[20] They found that carriers reach thermal equilibrium with the lattice subsystem on a time scale of about 10 ps, by emitting optical phonons and degenerating into acoustic phonons; moreover, after the laser irradiation a significant emission of electrons from the surface occurs, as a consequence of photo and thermal emission processes. On a longer time scale, all the relaxation mechanisms previously mentioned should be taken into account to correctly describe the main features of semiconductor response to the ultrashort laser irradiation.

I.1.3. *Dielectrics*

For dielectric materials with bandgap larger than the photon energy, multi-photon transitions are necessary to promote the initial creation of the free-carriers. The absorption is, then, enhanced by avalanche ionization once free carriers in the conduction band have been produced. For ultrashort laser pulses (≤ 100 fs), only multi-photon ionization could already produce the density of electrons required for breakdown and surface damage. In such a case, the resulting ablation of material is determined by the intrinsic properties of the sample (i.e. bandgap energy), and the process becomes highly deterministic in contrast to the stochastic nature of the long-pulse case.[22] The dynamics of femtosecond laser interactions with dielectrics have been recently discussed in refs. 23 and 24, while the resulting ablation process has been investigated experimentally and described theoretically in a number of papers.[25,26,27,28,29,30] We refer the interested reader to these studies for a detailed analysis of the main properties of ultrashort laser interaction processes with dielectrics since we are not going to deal with these materials in the present thesis.

I.2. **Material removal processes and expansion**

In the previous section, we showed that the thermalization of the laser energy in the irradiated material (metals and semiconductors) typically takes few picoseconds. This time interval is too short for significant expansion to occur. In fact, the expansion velocity of the atomic layers is determined by the pressure gradients set by the laser radiation inside the material, with respect to the external vacuum; this velocity is limited by the material sound velocity thus resulting, within a ps timescale, in a negligible expansion. Thus, ultrashort laser pulses heat a material to high temperature and pressure states, before significant expansion starts, often creating a supercritical material at solid density. The starting point to describe plume expansion dynamics can be considered as a solid density material with an initial temperature determined by the amount of deposited energy.

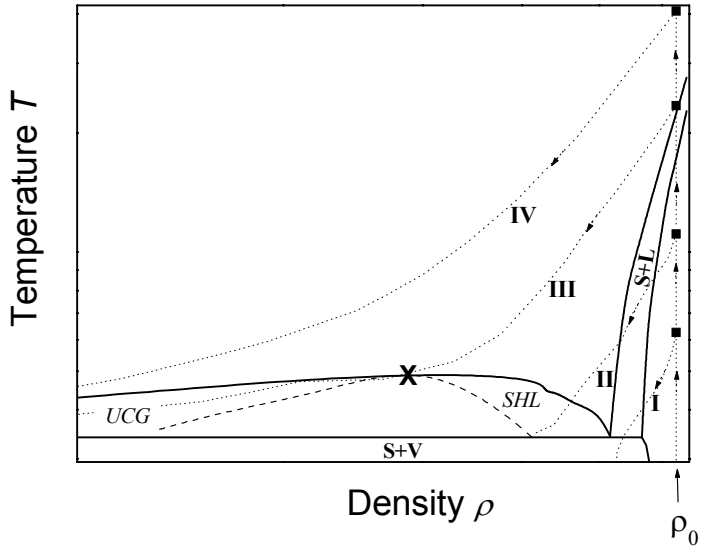

Fig. 1.3: Schematic temperature-density diagram of a material, and thermodynamic pathways following ultrashort laser irradiation in different regimes. S+L, S+V are the solid-liquid and the solid-vapor coexistence regions, respectively. *SHL* and *UCG* show the super-heated liquid and the undercooled-gas regions, respectively. The dashed line represents the spinodal. The cross (x) represents the critical point. The vertical dotted line indicates the isochoric heating occurring at near-solid density ρ_0. Once heated up at a certain temperature (■), then the material relaxes following a thermodynamic pathway depending on the initial temperature. In the figure four qualitative pathways corresponding to spallation **(I)**, phase explosion **(II)**; fragmentation **(III)**, and vaporization **(IV)**, respectively, are reported (see text for details).

The primary reaction of the system to the absorption of the pulse is to expand in order to relieve the important thermoelastic pressure build-up induced by the constant-volume heating

of the target. However, the material also relaxes by emitting strong pressure waves which could play an important role in the ablation process.

As shown by eqs. (1.2) and (1.3), the energy density inside the material following the laser irradiation decreases exponentially with depth, thus allowing the coexistence of various distinct ablation regimes. In fact, laser ablation in the short-pulse regime involves both thermal and mechanical processes, which are effective at different deposited energy densities and, hence, different depths under the surface of the target. Ablation typically occurs hundreds of picoseconds after the absorption of the pulse, much later than the time required for the equilibrium between electronic and atomic degrees of freedom to establish. Hence, the details of the complex non-thermal processes which occur shortly after the absorption of the pulse are not expected to play a crucial role in the material removal. Ablation should thus be dominated by the thermodynamics or by processes occurring on a mesoscopic scale.

Along this way, Perez and Lewis developed a Molecular Dynamics (MD) simulation to describe the relaxation of a two-dimensional Lennard-Jones fluid, after the irradiation by a femtosecond laser pulse.[31] They followed separately the evolution of the thermodynamic states of the condensed and gaseous phases, starting from the laser heating assumed to be instantaneous at the solid density, going through adiabatic plume expansion and decomposition, up to its final de-excitation. Thus, they were able to distinguish four different mechanisms to account for material ablation. Fig. 1.4 shows a schematic temperature-density diagram of a material and the thermodynamic pathways corresponding to the four different mechanisms following ultrashort laser irradiation. The characteristics of each of these processes are discussed in the following.

I. Photo-mechanical processes: Spallation

This results from the loss of stability of the solid target following the passage of a tensile pressure wave. After the laser energy delivery to the target, the surface temperature increases dramatically, and a strong compressive stress is generated on the surface and penetrates into the target. Spallation is the result of internal failure due to the creation of defects induced by tensile stresses and is effective at low fluences (close to the ablation threshold), when strong compressive pressure waves are running through the system, inducing fractures parallel to the surface of the

sample and ejection of complete layers of material which constitute the main part of the plume.

The isochoric heating takes the system to a supercritical state still in the solid phase space; then it relaxes by cooling down and enters the solid-vapour region of the phase diagram, below the triple point. These phase changes are driven by the stretching of the solid induced by the tensile compressive wave (negative pressure wave) propagating inside the material, which pushes the system into a mechanically unstable state which finally degenerates in the fracture of the solid. As fluence increases, the amplitude of the tensile wave propagating inside the sample decreases and eventually vanishes. As this occurs, the contribution of spallation to the total yield diminishes to the profit of homogeneous nucleation. Spallation-like ablation has been reported by several studies, as experiments on gels and biological tissues,[32, 33] or MD simulations of ablation of organic solids.[34,35]

II. Phase explosion

It comes from homogeneous nucleation of gas bubbles inside a superheated, metastable liquid. When the energy delivered to the system increases, relaxation can push the material into the liquid-vapour coexistence region up to crossing the binodal line between the triple point and the critical point.

Let's recall that if a non-equilibrium liquid system has enough time to relax towards an equilibrium state, its thermodynamic path in the phase diagram follows the binodal line, which is the coexistence locus between the liquid and vapour phases. On the contrary, when such a system is, for instance, rapidly heated it can undergo superheating (when its temperature exceeds the boiling point at the given pressure), thus entering the region of the metastable states which, in a temperature-density (T, ρ) phase diagram, is the region delimited by the binodal line and the spinodal line (see Fig. 1.4). In this region, the free-energy of the gas phase becomes lower than that in the liquid phase, which means that the homogeneous liquid is no longer the most stable configuration. For long enough waiting times or a high enough degree of metastability, gas bubbles are expected to form inside the metastable liquid by a process called *homogeneous nucleation*. For high nucleation rates, the liquid can rapidly decompose into an

equilibrium mixture of liquid droplets and monomers; in this case one speaks of *phase explosion.*[36] In a (T, ρ) diagram, the spinodal line and the line T=0 delimit the region of the unstable states which are thermodynamically prohibited. The closer is the system to the spinodal line (high degree of metastability), the higher is the nucleation rate and, thus the more efficient is the phase explosion mechanism.[37] Thus, if the system enters deeply in the metastable region, high nucleation rates are reached and ablation can be induced by the rapid transition from a superheated liquid state to a mixture of vapour and liquid droplets through phase explosion. The condensed phase gradually converts into gas by nucleation and growth of gas regions; since the timescale for this transformation to take place is very long, liquid droplets can persist in the plume for a very long time.

At this point, it should be noted that the emission of liquid droplets from the solid target could be obtained also through *heterogeneous nucleation*, where the new phase appears on the material surface, at impurity particles, etc. . Nevertheless, Kelly and Miotello pointed out that for high fluences and very short pulses the target is unable to boil because the time scale does not permit the necessary heterogeneously nuclei to form.[38] Thus, the system can be rapidly heated up to the thermodynamic critical point and even more, without experiencing any heterogeneous phase transition.[39]

Several authors suggested that a sufficient condition for homogeneous nuclei to form is that the system has to be heated up to 90% of the critical temperature T_C.[36, 38, 40, 41] Perez and Lewis pointed out that this criterion is rigorously correct for slow heating rates at nearly constant pressure but not for isochoric heating following short-pulse laser ablation because here the system is actually pushed away from the metastable region in the first place.[31] In this case, the occurrence of homogeneous nucleation depends, rather, on the relaxation path followed during the expansion by the ablated material and, in particular, on its degree of metastability (how deep in the metastable region the system enters). In fact, the rate of homogeneous nucleation (nuclei cm^{-3} s^{-1}) is given by

$$I_n \propto \exp\left(-\frac{\Delta G}{k_B T}\right) \tag{1.4}$$

where ΔG is the free-energy barrier for homogeneous nucleation to occur. Since this barrier vanishes at the spinodal line, the actual determining parameter for efficient nucleation is just the degree of "vicinity" to the spinodal.

It is worth noticing that the free energy vanishing in the vicinity of the critical point may result in the establishing of an another relaxation mechanism, known as *spinodal decomposition*[42]. It consists of the development of inhomogeneous structures inside the relaxing fluid as a result of thermodynamic instabilities (small density fluctuations). On a thermodynamic point of view, this mechanism is strongly different from classical nucleation theory and, up to now, it has been addressed as a fundamental ablation mechanism only by Vidal et al.[43]

III. Fragmentation of a highly strained supercritical fluid.

As the laser energy is further increased, the system relaxation path falls well above the critical point, thus leading to ablation outside the vapour-liquid metastable region. Nucleation cannot be addressed as the main ablation mechanism and, given the large number of clusters present in the plume, vaporization must also be excluded. Ablation is therefore not caused by a photothermal process but may have, in this case, a mechanical origin.

Fragmentation results from the conversion of the internal stress stored in the expanding target into surface energy: when the elastic energy stored in a region of the target is equal to the surface energy it would have if isolated, the excess elastic energy is converted into surface energy and fragments are created. The material decomposes into a collection of small clusters as a consequence of the extremely high stresses superimposed by the laser superheating. It does not require any change of phase, nor the crossing of a metastability or instability limit, and thus can occur in supercritical conditions where phase explosion and spinodal decomposition are not possible. The thermodynamic relaxation paths proceed above the critical point, then crossing the binodal curve at sub-critical densities, far enough from the critical point to avoid the instauration of any thermal decomposition process.

This phenomenon has been frequently observed in systems subjected to large strain rates, as small droplets under isochoric heating,[44] free-jet expansion of

liquids,[45] etc., as well as numerically described by means of hydrodynamic codes. In particular, Glover modelled the adiabatic plume expansion by means of the compressible non-dissipative equations for mass, momentum and energy conservation (the Euler equations) in the planar case for a silicon target[46].

The Euler equations must be augmented by an equation of state. Glover imposed self-similar solutions in the ideal gas approximation, thus finding that the material undergoes a very strong cooling due to expansion, with a quenching rate much higher than the rate at which the bulk surface is initially quenched. Besides, the plume is subjected to very strong velocity gradients due to its vacuum expansion, and the strain associated with them leads to mechanical bond breaking and, thus, to fragmentation. For the fragmentation process to develop, it is necessary to overcome the energy costs to create additional surface area. This allows an estimation of the mean cluster size (diameter *d*), simply by balancing the kinetic energy of expansion and the required energy for additional surface area creation, thus obtaining for spherical fragments[47]:

$$d = \frac{6}{S}$$
$$S = \left[\left(\frac{d\rho}{dt} \right)^2 \frac{3}{5\rho\gamma} \right]^{\frac{1}{3}} \qquad (1.8)$$

being *S* the surface to volume ratio and γ the surface energy. Eq. (1.8) gives mean fragment sizes of ≈10 nm for the typical lattice temperature attained during ultrashort laser irradiation. Similar results were found by MD simulation in ref. 31.

It is worth noticing that a more reliable description of the fluid relaxation paths could be obtained by substituting the ideal gas equation of state with a *caloric* equation of state (which is the equation of state for an ideal gas with a non constant pressure-to-volume specific heat ratio) or, even more, by the generalized Van der Waals equation of state.[48,49]

IV. Vaporization

If the energy delivered by the laser is high enough, the surface layers of the target are completely atomized since the corresponding thermodynamic relaxation paths never cross the liquid-vapour coexistence curve or crosses it far away from the critical point. In this regime, only a small percentage (some percent) of the total amount of atoms is contained in clusters.

In conclusion, as depicted by the Two Temperature Model (eq. (1.3)), the spatial energy distribution built up inside the target by the laser irradiation and subsequent *e-ph* thermalization decreases exponentially with depth. Thus, atomic layers placed at different depths below the surface are characterized by different absorbed energy densities and, hence, by different temperature histories. The material at different depths subsequently undergo adiabatic relaxation following different thermodynamic pathways, as shown in Fig. 1.4, which depend on the initial local temperature, thus resulting in the simultaneous establishing of one or more of the processes reported above. Therefore ultrashort laser ablated plumes could be made of several species, from neutral atoms to aggregates of particles, as a consequence of the complex interplay of several different processes.

Vacuum expansion of the plume could be described by means of the three-dimensional hydrodynamic model proposed by Anisimov et al.[50] The model, which we are not going to describe in detail here, starts from the solution of the gas-dynamic equations assuming an adiabatic expansion of the plasma plume into vacuum and allows an estimation of several key parameters such as kinetic energy (temperature) of the species or plume divergence.

References

[1] B. Rethfeld, K. Sokolowski-Tinten, D. von der Linde, S.I. Anisimov, Appl. Phys. A 79, 767 (2004).

[2] J. C. Kieffer, P. Audebert, M. Chaker, J. P. Matte, H. Pépin, T. W. Johnston, P. Maine, D. Meyerhofer, J. Delettrez, D. Strickland, P. Bado, and G. Mourou, Phys. Rev. Lett. 62, 760 (1989).

[3] M. Born and E. Wolf, Principles of Optics 6th ed., Pergamon Press, Oxford, 1993.

[4] S.-S. Wellershoff, J. Hohlfeld, J. Güdde, E. Matthias, Appl. Phys. A 69 [Suppl.], S99 (1999).

[5] B. Rethfeld, A. Kaiser, M.Vicanek and G. Simon, Appl. Phys. A 69, S109 (1999); Phys. Rev. B 65, 214303 (2002).

[6] W. S. Fann, R. Storz, H. W. K. Tom and J. Bokor, Phys. Rev. B 46, 13592 (1992)

[7] C. Suàrez, W.E. Bron, and T. Juhasz, Phys. Rev. Lett. 75, 4536 (1995).

[8] S.I. Anisimov, B.L. Kapeliovich and T.L. Perel'man, Sov. Phys. JEPT 39, 375 (1974).

[9] S. Nolte, C. Momma, H. Jacobs, A. Tünnermann, B. N. Chichkov, B. Wellegehausen, and H. Welling, J. Opt. Soc. Am. B 14, 2716 (1997).

[10] K. Furusawa, K. Takahashi, H. Kumagai, K. Midorikawa, and M.Obara, Appl. Phys. A 69, S359 (1999).

[11] N. W. Ashcroft, N. D. Mermin, Solid State Physics, Holt-Saunders Tokyo (1976).

[12] M. Fox, Optical properties of Solids (Oxford University Press, Oxford, 2001).

[13] J. P. Callan, PhD thesis, Harvard University (2000).

[14] P. L. Silvestrelli, A. Alavi, M. Parrinello, and D. Frenkel, Phys. Rev. Lett. 77, 3149 (1996).

[15] Shank C. V.,Yen R. and Hirlimann C., Phys. Rev.Lett. 50, 454–457 (1983).

[16] A. Rousse, C. Rischel, S. Fourmaux, I. Uschmann, S. Sebban, G. Grillon, Ph. Balcou, E. Förster, J.P. Geindre, P. Audebert, J.C. Gauthier and D. Hulin, Nature 410, 65 (2001).

[17] K. Sokolowki-Tinten, J. Bialkowski, M. Boing, A. Cavalleri, and D. von der Linde, Phys. Rev. B 58, R11805 (1998).

[18] K. Sokolowski-Tinten, H. Schulz, J. Bialkowski, and D. von der Linde, Appl. Phys. A: Solids Surf. 53, 227 (1991).

[19] P. Stampfli and K. H. Bennemann, Phys. Rev. B 46, 10686 (1992).

[20] T.Y. Choi and C.P. Grigoropoulos, J. Appl. Phys. 92, 4918 (2002).

[21] F. Korte, J. Serbin, J. Koch, A. Egbert, C. Fallnich, A. Ostendorf, B.N. Chichkov, Appl. Phys. A 77, 229 (2003).

[22] A.P. Joglekar, H. Liu, G.J. Spooner, E. Meyhöfer, G. Mourou, A.J. Hunt, Appl. Phys. B 77, 25 (2003).

[23] S.S. Mao, F. Quéré, S. Guizard, X. Mao, R.E. Russo, G. Petite, P. Martin, Appl. Phys. A 79, 1695 (2004).

[24] M.D. Feit, A.M. Komashko, A.M. Rubenchik, Appl. Phys. A 79, 1657 (2004).

[25] A. Rosenfeld, M. Lorenz, R. Stoian, D. Ashkenasi, Appl. Phys. A 69 [Suppl.], S737 (1999).

[26] R. Stoian, D. Ashkenasi, A Rosenfeld, E.E.B Campbell, Phys. Rev. B 62, 13167 (2000).

[27] R. Stoian, A. Rosenfeld, D. Ashkenasi, I.V. Hertel, N.M. Bulgakova, E.E.B. Campbell, Phys. Rev. Lett. 88, 097603 (2002).

[28] N.M. Bulgakova, R. Stoian, A. Rosenfeld, I.V. Hertel, E.E.B. Campbell, Phys. Rev. B 69, 054102 (2004).

[29] F. Costache J., Reif, Thin Solid Films 453-454, 334 (2004).

[30] J. Reif, F. Costache, S. Eckert, M. Henyk, Appl. Phys. A 79, 1229 (2004).

[31] D. Perez and L. J. Lewis, Phys. Rev. Lett. 89, 255504-1 (2002); and Phys. Rev. B 67, 184102 (2003).

[32] G. Paltaud and H. Schmidt-Kloiber, Appl. Phys. A: Mater. Sci. Process. 62, 303 (1996).

[33] I. Itzkan, D. Albagli, M. Dark, L. Perelman, C. von Rosenberg, and M. Fields, Proc. Natl. Acad. Sci. U.S.A. 92, 1960 (1995).

[34] L. V. Zhigilei and B. J. Garrison, J. Appl. Phys. 88, 1281 (2000).

[35] C. Schäfer, H. M. Urbassek and L. V. Zhigilei, Phys. Rev. B 66, 115404 (2002).

[36] M. M. Martynyuk, Sov. Phys. Tech. Phys. 19, 793 (1974).

[37] P. G. DeBenedetti, *Metastable Liquids-Concepts and Principles* (Princeton University Press, Princeton New Jersey, 1996).

[38] R. Kelly and A. Miotello, Appl. Surf. Sci. 96-98, 205 (1996).

[39] L. V. Zhigilei, D. S. Ivanov and E. Leveugle, in High-Power Laser Ablation V, Proc. SPIE, 2004.

[40] N. M. Bulgakova and A. V. Bulgakov, Appl. Phys A 73, 199 (2001).

[41] J. K. Chen and J. E. Beraun, J. Opt. A: Pure Appl. Opt. 5, 168 (2003).

[42] V. P. Skripov and A.V. Skripov, Sov. Phys. Usp. 22, 389 (1979).

[43] F. Vidal, T.W. Johnston, S. Laville, O. Barthélemy, M. Chaker, B. Le Drogoff, J. Margot, and M. Sabsabi, Phys. Rev Lett. 86, 2573 (2001).

[44] J. A. Blink and W. G. Hoover, Phys. Rev. A 32, 1027 (1985).

[45] E. L. Knuth and U. Henne, J. Chem. Phys. 110, 2664 (1999).

[46] T. E. Glover, J. Opt. Soc. Am. B 20, 125 (2003).

[47] D. E. Grady, J. Appl. Phys. 53, 322 (1982).

[48] Ya. B. Zel'dovich and Yu. P. Raizer, *Physics of Shock Waves and High-Temperature Hydrodynamic Phenomena* (Academic, New York, 1966).

[49] L. D. Landau and E.M. Lifshitz, *Statistical Physics* Part. 1 (Pergamon, Oxford, 1960).

[50] S. I. Anisimov, D. Bauerle and B. S. Luk'yanchuk, Phys. Rev. B 48, 12076 (1993); S. I. Anisimov, B. S. Luk'yanchuk and A. Luches, Appl. Surf. Sci. 96, 24 (1996).

CHAPTER II

Experimental techniques and apparatus

Several techniques have been devised to characterize the process of laser ablation: from pump-probe measurements of the dynamical evolution of surface properties such as reflectivity, dielectric constant and so on, to spectroscopic, photographic and electrostatic characterization of the ablated plume to, finally, the morphological and structural investigation of the deposited thin films and aggregates properties.

In this chapter, the experimental techniques and the measurement apparatus employed during the present thesis will be described. Along with the different laser systems and the experimental arrangements set up to perform laser ablation of solid targets, the techniques used to characterize the ablated material (Optical Emission Spectroscopy, Fast Photography, Langmuir probe) and the deposited samples (Atomic Force Microscopy) will be reported on.

II.1 The experimental setup

A general scheme of the experimental setup showing simultaneously all the techniques employed in the present thesis is shown in Fig. 2.1.

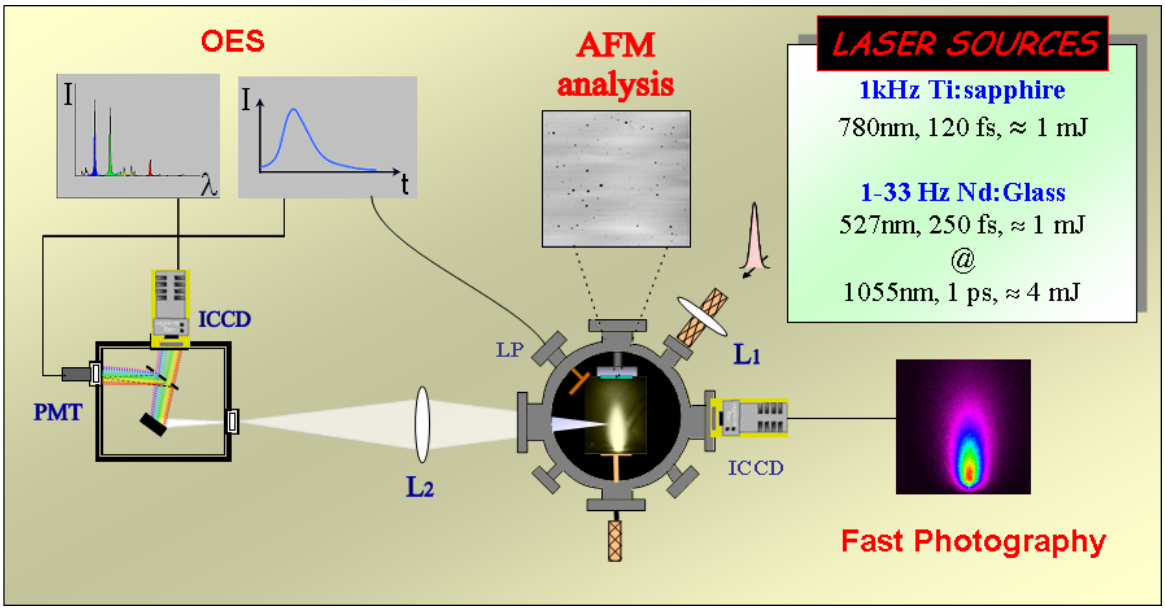

Figure 2.1: Schematics of the experimental setup.

The laser light coming from one of the available laser sources is guided to the vacuum chamber and focused onto a solid target, mounted on a rotating holder to avoid craterization. The light emitted by the excited ablated species is studied at right angles with respect to the normal to the target surface by means of two techniques. Fast Photography, through an Intensified Charged Coupled Device (ICCD), allows studying the spatial and temporal expansion dynamics of the plume emission as a whole, thus shedding a light on the properties of plume evolution. Optical Emission Spectroscopy (OES), on the other hand, is performed by means of a monochromator coupled with an ICCD camera and a photomultiplier tube (PMT), thus giving information on the spatial and temporal dynamics of the whole emission spectrum in a suitable spectral interval (ICCD) as well as of selected spectral lines (PMT). Further studies about ions yield and their temporal dynamics have been performed by a Langmuir probe placed in the vacuum chamber nearly in front of the expanding plume. Finally, the morphological and structural characterization by Atomic Force Microscopy (AFM) of deposited thin films and aggregates gives information about both the characteristics of the produced particles and the possible technological applications of ultrashort pulsed laser ablation as an advanced material processing technique. All the experiments were performed in high vacuum at a residual pressure of ~10^{-7} mbar, obtained by a turbo-molecular pump working in series to a rotative pump.

II.2 The laser sources

The laser sources used to perform laser ablation experiments were two solid-state systems:

i. A Ti:sapphire laser, with a maximum pulse output energy of ≈1 mJ, pulse duration of ≈100 fs and wavelength of ≈800 nm.
ii. A Nd:Glass laser with a maximum pulse output energy of ≈4 mJ, pulse duration of ≈1 ps and wavelength of 1055 nm, which can be frequency doubled by Second Harmonic Generation technique (SHG) to yield pulses of maximum output energy of ≈1 mJ, pulse duration of ≈250 fs and wavelength of 527 nm.

The details of each laser system are briefly described below.

II.2.1 Ti:sapphire laser system

It consists of a regenerative amplifier based on the laser action due to the Ti^{3+} ion in a Al_2O_3 (sapphire) crystal doped with Ti_2O_3, which is performed on a wavelength band extending from 670nm to over 1μm. The laser system is made of two main unities:

- Mode-locked Ti:sapphire oscillator *"Tsunami"* mod. 3941-M3S, Spectra Physics [1], whose output pulses have a maximum energy of ≈10 nJ, a repetition rate of 82 MHz and cover a wavelength range from 720 nm to 850 nm. It is pumped by the output of a CW Nd:YVO laser system (*"Millennia"*) in its turn pumped by a matrix of diode lasers.
- Regenerative Amplifier *"Spitfire"*, Spectra Physics[2]. It is made in its turn of three main unities. First of all, a "Pulse Stretcher" lowers the Tsunami pulse output power, to avoid optics damaging, by means of a 16 steps system of mirrors and gratings. The second unit, the "core" of the Regenerative Amplifier, is made of a laser cavity with a sapphire rod pumped by the output pulses of a Nd:YLF laser system ("Merlin", Q-Switched, ≈ 527nm, P ≈ 6W, ≈ 0.3μs). A Pockels cell synchronizes the seeding of the stretched pulses with the optical pumping of the rod: at each round trip the pulses are amplified until when the electronic signal of a second Pockels cell pushes them away from the cavity at a frequency of 1 kHz and an output energy of ≈ 1 mJ. Finally, the amplified pulses enter the "Compressor" unit, where they are compressed by a second set of mirrors and gratings to reach the final pulse duration of ≈ 100 fs.

To avoid target damaging due to the high repetition rate of the laser system, the ablation experiments were performed at a frequency of 3 Hz by means of a pulse picker based on a Pockels cell. A schematics of the whole system described so far is shown in Fig. 2.2.

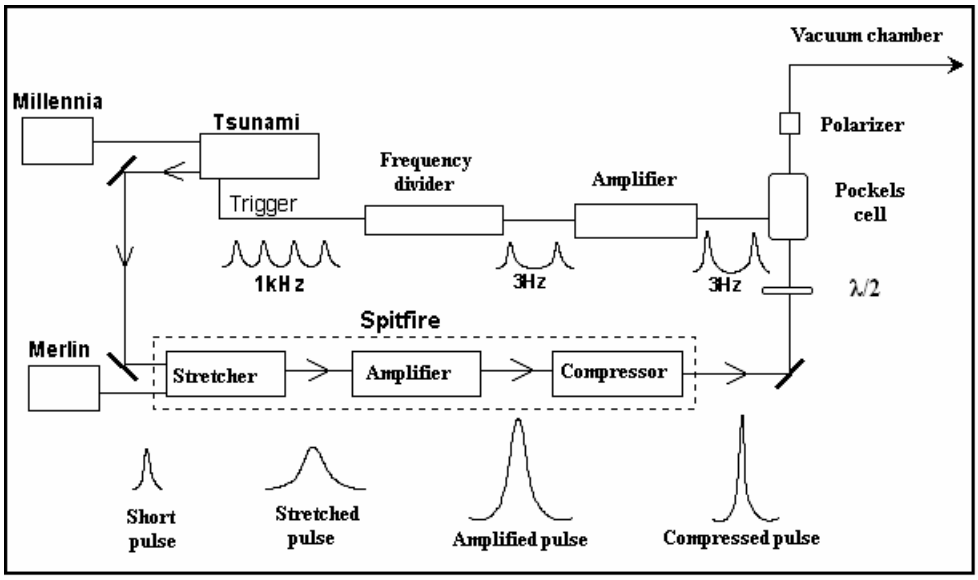

Figure 2.2: Schematics of the Ti:sapphire laser system used during the laser ablation experiments.

II.2.2 Nd:glass laser system

It is a negatively feedback active-passive mode-locked Nd:glass laser system, mod. "Twinkle" by Light Conversion Ltd. The laser action is due to the ions Nd^{3+} contained as impurities in a phosphate glass matrix. The use of an amorphous medium instead of a crystalline matrix, as in the case of the more common Nd:YAG laser systems, increases line broadening and, consequently, leads to a greater number of longitudinal modes running in the cavity, which can be properly mode-locked to yield ultrashort pulses of about 1 ps duration. The main unities of Twinkle laser system are (Fig. 2.3):

- Master Oscillator (MO)
- Pulse Stretcher
- Regenerative Amplifier (RA)
- Pulse Compressor

MO is the main resonator and contains two laser heads optically pumped by flashlamps. Here, pulses of about 1ps duration are built up by feedback controlled active-passive mode-locking. The passive mode-locker is a saturable absorber (dye) and allows phase locking of all the longitudinal modes (LM) running in the cavity thus giving pulses with FWHM of 1-1.2 ps and average energy of 1 mJ. Laser intensity is kept rather low in MO to prevent optics damaging due to self phase modulation. The active mode-locking is performed by an electro-optic modulator (Pockels cell controlled by radiofrequency), working as a fast shutter, which further

improves LM phase locking and ensures the seeding of pulses of controlled intensity in the Stretcher.

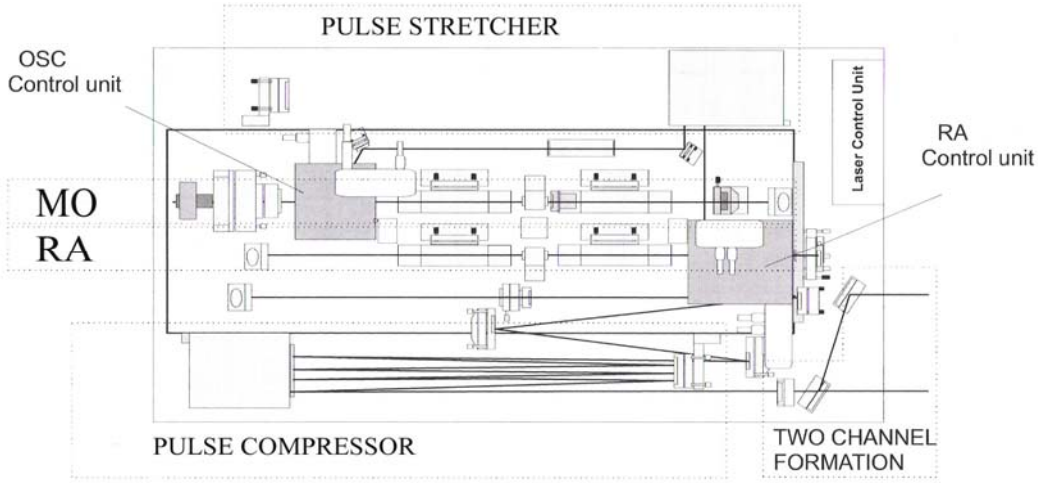

Figure 2.3: Schematics of the Nd:glass laser system used during the laser ablation experiments.

The positive group velocity dispersion stretcher expands these pulses up to ~300 ps by means of two golden coated holographic gratings with 1800 lines/mm and a diffraction efficiency greater than 95%. A Pockels cell sets the seeding of stretched pulses into the RA, which is a resonator similar to the MO, where they are amplified up to ~7 mJ with small spectral gain narrowing and negligible self phase modulation effects. The amplified pulses are then seeded by a Pockels cell to the Compressor unit where they are recompressed up to durations of ~0.8-1 ps. The output pulse energy is ~4 mJ at 1055 nm and the repetition rate is ~33 Hz.

II.2.2.1 Second harmonic generation of femtosecond pulses

The generation of femtosecond pulses starting from the fundamental infrared radiation is accomplished by the nonlinear pulse compression (NPC) technique, originally proposed for the Nd-doped lasers.[3,4] The compression idea is based on a special group velocity situation, which is attained for frequency doubling in type II phase-matching KDP crystals at wavelengths around 1 μm.

When a type II crystal slab in vacuum is irradiated simultaneously by two pulses with extraordinary (e) and ordinary (o) polarizations with center frequencies $\omega_e = \omega_o = \omega$, coalescence of the pulses during their propagation leads to the generation of a second harmonic

e-polarized pulse with center frequency $\omega_2 = 2\omega$. However, the efficiency of conversion strongly depends on the group-velocity dispersion which makes the spatial overlap to get lost more and more as the pulses propagate inside the crystal. To overcome these troubles and get a dramatically increased conversion efficiency, the *e*-pulse, with the higher group velocity ($v_e > v_o$), could be simply predelayed with respect the *o*-pulse to create conditions for longer overlap.

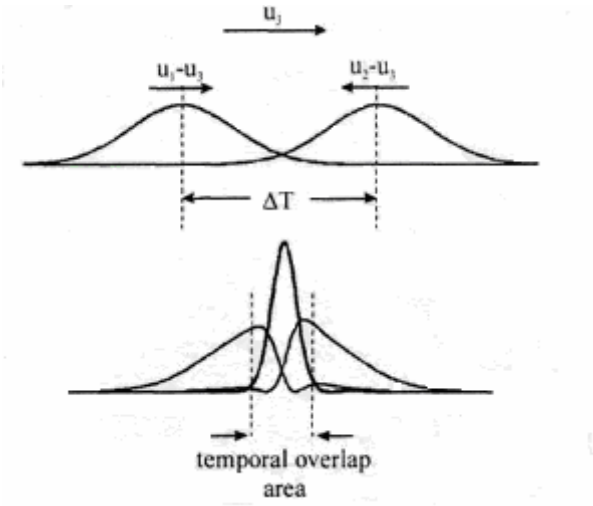

Figure 2.4: Principle of nonlinear pulse compression. Here the u_j are the group velocities, and the index 3 stands for the second compressed harmonic pulse.

Numerical simulations demonstrate that an intensity conversion efficiency of even 300% can be achieved (essentially ascribed to the simultaneous shortening of the pulse), according to the length of the crystal and to the predelay between the pulses.[3] Moreover, the spatial overlap between the *e* and *o* pulses happens in a very short time interval thus leading to a compressed second harmonic of temporal duration of even 0.25 ps, as schematically shown in Fig. 2.4.

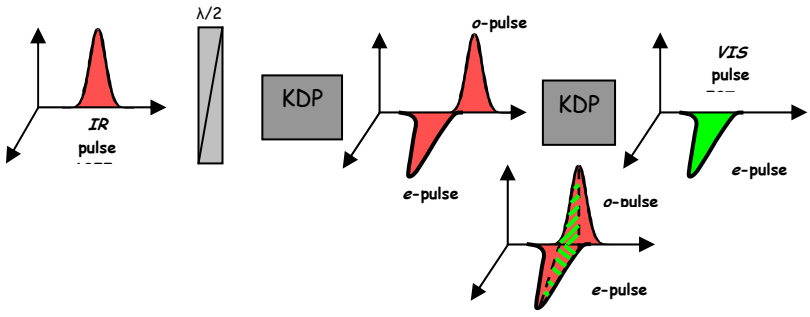

Figure 2.5: Schematics of the nonlinear pulse compression apparatus used in our Nd:glass laser system.

This peculiar non linear compression is achieved in our laser system by means of essentially three optical components, as shown in Fig. 2.5. About the 70% of the 4mJ infrared picosecond

energy is sent to a half wavelength phase plate (λ/2) which rotates its polarization. The pulse enter a 15mm long II-type KDP crystal, and propagates as a superposition of an ordinary and extraordinary pulses which gain a group velocity dispersion which dephases and delays them. The second harmonic signal generated inside this stage is negligible owing to the increasingly phase mismatch between the *e-* and *o-* pulses. Finally, the predelayed pulses enter a 20mm long II-type KDP crystal where their phase mismatch is recovered and leads to a detectable overlap in a time window of about 0.25 ps with a conversed energy of about 1mJ at 527nm.

This radiation constitutes the femtosecond light source used in all the experiments accomplished by the Nd:glass laser system. Moreover, the remaining 30% of the input infrared radiation has been used during the experiments as a light source at 0.8-1ps pulse duration, 1055nm wavelength and a maximum output energy of ≈1.2 mJ.

II.2.3 Measurements of ultrashort durations: the autocorrelator

The ultrashort pulse durations, of both the visible and the infrared radiation, have been measured by means of two distinct autocorrelators, both working on the basis of the noncollinear second harmonic generation technique (SHG), where the spatial distribution of the SH light contains information on the time behaviour of the fundamental light pulse. The basic idea is that two replicas of a fundamental ultrashort light pulse pass non collinearly through a nonlinear crystal of type I oriented for non collinear SHG. In the region where the two replicas overlap, SH intensity distribution depends on the fundamental pulse time behaviour. Thus, by recording the SH light spatial distribution is possible to get information about the time behaviour of the fundamental pulse.

We are not going to explain the details of the technique here, well described elsewhere.[5] Nevertheless, an interesting feature regarding the autocorrelation technique employed to measure the pulse duration of the fs Nd:glass visible radiation has to be noticed. Here, after the splitting of the fundamental light pulse, a suitable system of mirrors changes of 90° the polarization of one of the two replicas before they overlap in the nonlinear crystal. Thus, the autocorrelation signal is given by an elliptical pattern which is able to reveal the potential pulse front tilting of the fundamental radiation. The pulse tilting, which is caused by angular misalignment of dispersing elements in either the pulse stretcher or compressor in ultrashort pulsed laser systems based on the chirped pulse amplification, is then revealed both in

horizontal and vertical planes as a tilt in the autocorrelation ellipse and can be properly adjusted.[6,7]

II.3 The ICCD camera

In the framework of the performed ablation experiments, two ICCD cameras (Andor Technologies) were used with different purposes: one for plume imaging, the other for plume spectroscopy.

Basically, the I-CCD camera consists of a Charged Coupled Device (CCD) and an Image Intensifier (Fig. 2.6).[8] The CCD is a silicon chip made up of a two dimensional array of photodetectors (512 x 512 pixels). When photons impinge onto a pixel several photoelectrons are generated by photoelectric effect. The photoelectrons pattern is then electronically transferred to an amplifier and processed.

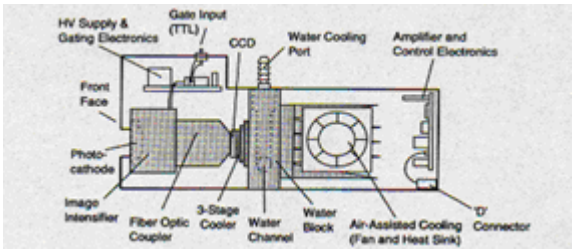

Figure 2.6: Section of the ICCD camera

To improve the signal to noise ratio, every spectroscopic measurement has been performed in *full vertical binning*, where the photoelectrons content of two or more pixel rows is first summed and then transferred to the amplifier. The noise we are dealing with is the *pixel reading noise*, and is due to the reading electronics of the ICCD. So, in full vertical binning mode, while the signal transferred to the amplifier is greater the electronic noise due to pixel reading is always the same thus increasing the signal to noise ratio. This acquisition mode cannot be worked for imaging measurements where each pixel contains the signal coming from a different region of the plume: no data can be summed since the electronic content coming from each pixel is necessary to reconstruct the plume spatial emission. On the contrary, during plume spectroscopy each pixel contains data about the whole spectrum and, thus, their electronic content can be summed without losing any plume spectroscopic information.

The Image Intensifier allows intensity amplification of the light signal, without changing its spatial structure, before reaching the CCD stage. It essentially consists of a *photocathode*, a *microchannel plate* (MCP) and a *phosphor coating* (Fig. 2.7) all placed in a vacuum tube.

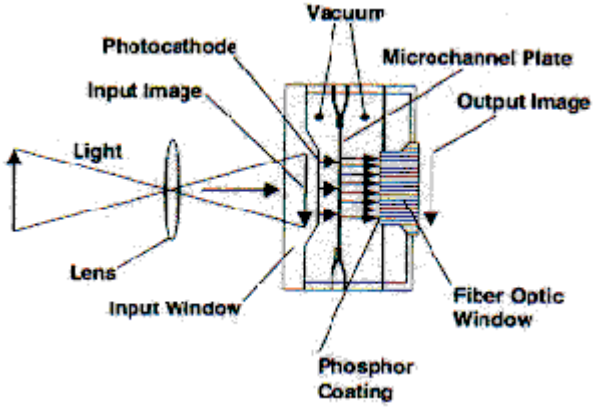

Figure 2.7: The Image Intensifier

Figure 2.7 describes the working mechanisms of the intensifier. Photoelectrons generated through photoelectric effects by photons impinging on the photocathode are accelerated by an electric field and reach the microchannel plate. This consists of a thin glass disc (~1mm thick) made of ~10^4-10^7 micro channels each with ~10μm average diameter and covered by a resistive material (typically semiconductor). The channels are biased by a high voltage (from 500 up to 1000 Volts) so that each photoelectron is greatly accelerated and generates a high quantity of secondary electrons by striking the inner walls of the channels. The signal amplification thus obtained is as high as 10^3-10^5 and may be adjusted by varying the MCP voltage by the "Gain Switch" placed on the ICCD head. The amplified photoelectrons pattern is finally accelerated by an electric field of several thousands Volts and strikes the phosphor plate thus generating a corresponding light pattern which can be processed by the CCD according to the electronic mechanisms previously described.

The state of the intensifier determines the state of the whole ICCD. If the intensifier is "on" (negative voltage gap from the photocathode to the MCP), then the measured signal reaches the CCD and is acquired; if the intensifier is "off" (positive voltage gap from the photocathode to the MCP) no light signal reaches the CCD to be detected. The electronic circuit which rules the opening and closing times of the intensifier is known as "*Gater*" and is controllable by software by varying two quantities: the "*gate delay*", which set the opening time of the ICCD, and the "*gate width*" which rules the temporal width of the "on" state of the ICCD. Thus by varying the ICCD opening time (gate delay) with respect to the laser pulse and

the ICCD opening duration (gate width) it has been possible to study the temporal dynamics of the plume features.

The ICCD noise may be divided in two main categories: pixel noise and fixed pattern noise. The latter is a fixed noise especially due to irregularities in the ICCD fabrication and can be eliminated by correcting the acquired signal for the background signal. The former, in its turn, may be divided in "reading noise", "dark shot noise" and "signal shot noise". The reading noise, as previously mentioned, is due to the ICCD electronics and may be reduced, if possible, by working in *full vertical binning* mode. The dark shot noise depends on the gate width and, being strongly temperature dependent, has been reduced during the experiments by cooling the ICCD at ~15 °C (done by software). The signal shot noise, on the contrary, depends exclusively on the signal intensity.

To further improve the signal to noise ratio, both during spectroscopic and imaging measurements the signal has been acquired in *accumulate* mode: the plume emission spectra/images are first summed over a certain number of laser shots (adjustable by software) and then electronically processed.

II.4 OES setup

Optical emission spectroscopy, as previously mentioned, was one the techniques employed to study the plume properties and dynamics. To do that, the bright plasma emission from a selected spatial region was collected through a side window at right angles to the plume expansion direction. A convex lens produced a 1:1 correspondence between the sampled area of the plume and the image, which was focused onto the slit of a 0.25-m monochromator (mod. Jobin-Yvon, HR250) equipped with a turret of two interchangeable gratings (1200 groves/mm and 100 groves/mm, maximum resolution ~0.05 nm). The low resolution grating (100 groves/mm) was used to get a look of the whole emission spectrum over the spectral range of about 200-900 nm to easily find its atomic and molecular features, while the 1200 groves/mm grating was then used to study with an higher resolution the dynamics of selected spectral lines and structures over spectral windows of about 50nm in almost the same spectral range as before. The two exit slits of the monochromator were coupled with an ICCD camera and a PMT, which could be alternatively irradiated by the signal dispersed by the grating through a rotating mirror.

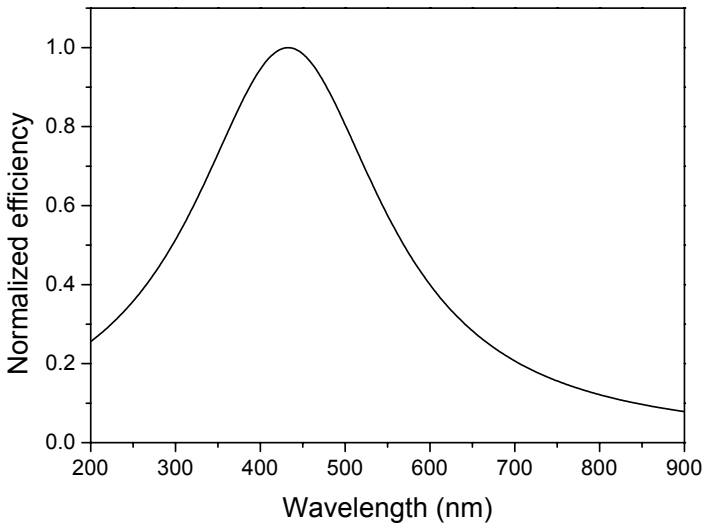

Figure 2.8: Normalized efficiency of the OES apparatus.

Thus the plasma optical emission characterization included both spectral analysis of all the emitting species in the spectral range 200–900 nm (ICCD) and the time-resolved measurements of the emission from selected lines (PMT). Both PMT and ICCD (by means of its gating specifics) allowed characterization of the temporal evolution of the plume emission; to study also its spatial evolution the target holder was mounted onto a micrometric translator, thus allowing to map the spatial dynamics of plume emission at several distances from the target.

Figure 2.8 shows the efficiency curve of the whole spectroscopic system, essentially given by the convolution of HR250 and ICCD efficiencies. While the ICCD efficiency curve is quite flat over the wavelength range 200-900 nm, the monochromator turns out to be more sensitive in the middle of the visible region thus giving the efficiency behaviour shown in Fig. 2.8. The knowledge of the spectral response of the system allowed correction of the acquired spectra and was extremely important to study some properties of the plume, as will be shown in the next chapter.

II.5 Langmuir probe

The Langmuir probe is a diagnostic device used to determine several basic parameters of a plasma, such as temperature and density, as well as the transient characteristics of the impinging flux of particles. It simply consists of a small conducting probe (typically a cylinder or

a plate) placed into the plasma to be characterized and suitably biased to measure the current signal coming from the impinging charged particles. Actually, the current signal is determined by the difference between the probe and the plasma space potential V_p, being the latter just the potential of the plasma volume with respect to the vessel wall.

Fig. 2.9 reports on a scheme of the ion probe employed in our experiments to measure the transient characteristics of the ion emission flux in the laser-produced plasma plume. We used a planar Langmuir probe, oriented at ≈ 7° with respect to the normal to the target surface and located at a minimum distance of ≈45 mm from the target (actually, the distance was variable since the target holder could be moved back and forth as previously explained). The probe consists of a 2×2mm^2 square copper plate similar to that used in [9]. During ion collection the probe was biased at a suitable constant voltage between -10V and −30V, selected to work in the ion saturation region according to the plume electrical properties, and the collected ion current is determined by the voltage signal recorded by a digital oscilloscope across a 50 Ω load resistor. The bias was maintained using a 1 μF capacitor, which was sufficient to avoid charge saturation of the system in the bias regime studied here.

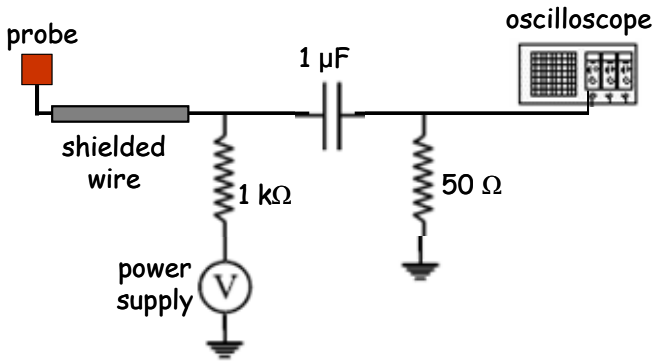

Figure 2.9: Electrical setup of the Langmuir probe used during the present experiments.

In spite of the relative simplicity of the experimental scheme, ion probes require a rather complicated theory to fully explain their current to voltage behaviour when inserted in a plasma. Here, we are not going to fully explain the details of the Langmuir probe theory, which have been already well reported by several authors.[10,11,12] In the following some general properties of a LP apparatus will be discussed.

The measured current is determined by the potential imposed on the probe and a typical current to voltage curve is shown in Figure 2.10. It is typically determined by the plasma properties in the immediate vicinity of the probe and can be generally divided into three parts.

When the probe is biased positively with respect to the local plasma potential V_p, the flux of particles reaching the probe will consist of carriers of negative charge (normally electrons), the positively charged ions being repelled.

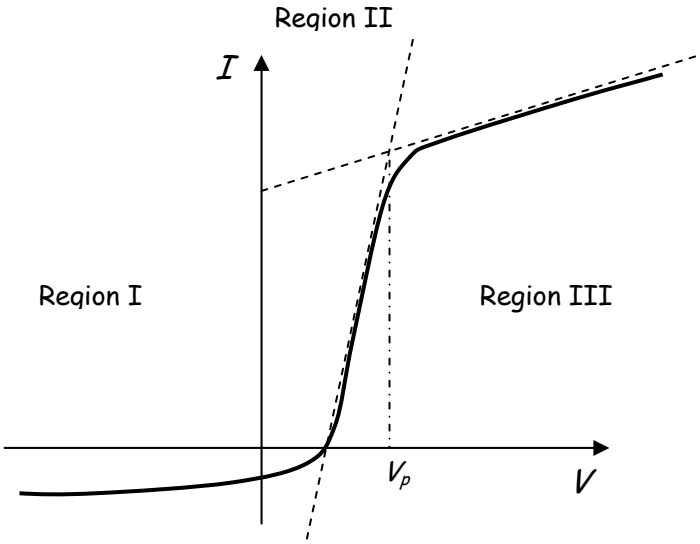

Figure 2.10: Typical I-V characteristic of a Langmuir probe.

This is generally called the electron accelerating region and is labelled as III in Figure 2.10. When the probe is biased at a potential slightly smaller than the plasma potential, only particles with enough energy to overcome the potential barrier will be collected. This region (region II in Figure 2.10) is called the electron retarding region since the probe actually acts as an energy selector, collecting only those electrons which have large enough kinetic energies to overcome the potential barrier. By evaluating the slope of the I-V characteristic in this region the electron temperature is obtained, and by measuring also the electron current at the plasma potential the electron density could be derived.[9] The third region (I) is accessed when the probe is biased increasingly negative relative to the plasma potential so that only positive ions will reach the probe. This is called the ion saturation region and all the measurements performed during the present thesis were operated in this conditions.

It is worth noticing that Langmuir probe theories generally apply to the characterization of static plasmas and not of transient laser ablated plumes which possess a forward directed velocity component of, typically, $\approx 10^6$ cm/μs. Nevertheless, Weaver et al.[13] noticed that in the typical laser ablation experimental conditions, as in our experiments, the Langmuir probe operates in almost collisionless conditions, where it has been shown that its *I-V* characteristic can be approximated to that of a static, nonflowing plasma.[14]

II.6 Atomic force microscopy

As well as optical emission spectroscopy allowed the characterization of the plume expansion dynamics, Atomic Force Microscopy collected information about morphological and structural properties of the deposited thin films and aggregates. The deposits were carried out at ambient temperature in high vacuum at a residual pressure of 10^{-7} mbar by placing a collecting substrate (mica) in front of the expanding plume.

Here we briefly review the AFM operating characteristics. An atomically sharp tip is scanned over a surface with feedback mechanisms that enable the piezo-electric scanners to maintain the tip at a constant force (to obtain height information) or height (to obtain force information) above the sample surface[15]. Due to forces acting between the surface and the tip, the cantilever is deflected away from its equilibrium position. It is possible to record the deflection as function of time and thereby form an image of the surface topography at nearly atomic resolution.

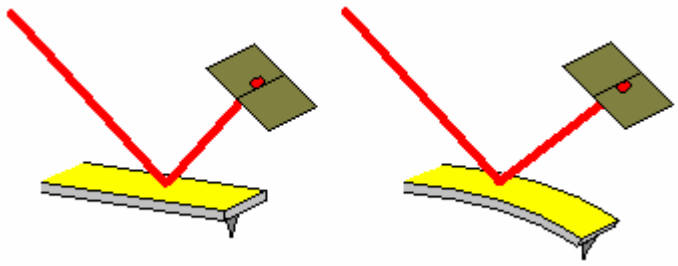

Figure 2.11: Schematics of the AFM optical detection system

Tips are typically made from Si_3N_4 or Si, and extended down from the end of a cantilever. The nanoscope AFM head employs an optical detection system in which the tip is attached to the underside of a reflective cantilever (Fig.2.11) onto the back of which a diode laser is focused[16]. As the tip scans the surface of the sample, moving up and down with the contour of the surface, the laser beam is deflected off the attached cantilever into a dual element photodiode. The photodetector measures the difference in light intensities between the upper and lower photodiodes, and then converts to voltage. Feedback from the photodiode difference signal, through software control from the computer, enables the tip to maintain either a constant force or constant height above the sample. The voltage that the feedback amplifier

applies to the piezo is a measure of the height of features on the sample surface. It is displayed as a function of the lateral position of the sample to yield a 3D topological view of its surface.

The primary purpose of these instruments is to quantitatively measure surface roughness with a nominal 5 nm lateral and 0.01nm vertical resolution on all types of samples. Depending on the AFM design, scanners are used to translate either the sample under the cantilever or the cantilever over the sample. There is clearly an important distinction between images resolved by wave optics and scanning probe techniques. The former is limited by diffraction, and latter primarily by apical probe geometry and sample geometry. Indeed, many authors have seen that it is the radius of curvature of the tip that significantly influences the resolving ability of the AFM.

There are several operating modes to work with the AFM, according to the specific measurement to perform. The *contact mode*, where the tip scans the sample in close contact with the surface, is the common mode used in the force microscope. The force on the tip is repulsive with a mean value of 10^{-9} *N*. This force is set by pushing the cantilever against the sample surface with a piezoelectric positioning element. Problems with contact mode are caused by excessive tracking forces applied by the probe to the sample. The *non-contact mode* is used in situations where tip contact might alter the sample in subtle ways. In this mode the tip hovers 50 - 150 Angstrom above the sample surface. Attractive Van der Waals forces acting between the tip and the sample are detected, and topographic images are constructed by scanning the tip above the surface. Unfortunately, the attractive forces from the sample are substantially weaker than the forces used by contact mode thus yielding a worse vertical resolution. *Tapping mode* allows high resolution topographic imaging of sample surfaces that are easily damaged or loosely hold to their substrate. Tapping mode imaging is implemented by oscillating the cantilever assembly at or near the cantilever's resonant frequency using a piezoelectric crystal. The piezo motion causes the cantilever to oscillate with a high amplitude (typically greater than 20nm) when the tip is not in contact with the surface. The oscillating tip is then moved toward the surface until it begins to lightly touch, or tap the surface. During scanning, the vertically oscillating tip alternately contacts the surface and lifts off, generally at a frequency of 50,000 to 500,000 cycles per second. As the oscillating cantilever begins to intermittently contact the surface, the cantilever oscillation is necessarily reduced due to energy loss caused by the tip contacting the surface. The reduction in oscillation amplitude is used to identify and measure

surface features. Tapping mode was used to scan the surface of all the deposits carried out by ultrashort laser ablation during the present thesis to avoid any alteration of the samples.

References

[1] *"Tsunami" Mode-Locked Ti:sapphire Laser*, User's Manual, Spectra Physics.

[2] *"Spitfire" Multikilohertz Pulsed Ti:sapphire Amplifier with Pulse Stretcher and Compressor*, User's Manual , Spectra Physics.

[3] Y. Wang, R. Dragila, *Phys. Rev. A* 41, 5645 (1990).

[4] Y. Wang, B. Luther-Davies, *Opt. Lett.* 17, 1459 (1992).

[5] C. Rullière, *Femtosecond Laser Pulses : Principles and Experiments*, Berlin (Springer) 1998.

[6] TFP Autocorrelator, User's Manual, Light Conversion.

[7] http://www.lightcon.com , Light Conversion Website

[8] Andor ICCD's, User's Manual, Andor Technology.

[9] B. Toftmann, J. Schou, T.N. Hansen, J.G. Lunney: Phys. Rev. Lett. 84, 3998 (2000)

[10] N. Hershkowitz, in Plasma Diagnostics, Volume 1, Discharge Parameters and Chemistry (eds. O. Auciello and D. L. Flamm), Academic Press, London (1989)

[11] B. E. Cherrington, Plasma Chemistry and Plasma Processing, 2, 113 (1982)

[12] J. D. Swift and M. J. R. Schwar, Electrical Probes for Plasma Diagnostics (Iliffe, London, 1970).

[13] I. Weaver, G. W. Martin, W. G. Graham, T. Morrow, and C. L. S. Lewis, Review of Scientific Instruments, 70, 1801 (1999)

[14] T. E. Sheridan and J. Goree, Phys. Rev. E 50, 2991 (1994).

[15] Binnig G., Quate C.F. and Gerber Ch., *Atomic force microscope*, Phys. Rev. Lett. 56 (9), 930-933 (1986).

[16] Meyer G. and Amer N.M., *Novel optical approach to atomic force microscopy*, Appl. Phys. Lett. 53 (12), 1045-1047 (1988).

CHAPTER III

Experimental characterization of the ultrashort laser ablation process

Up to the middle of 2003 there were few experimental investigations on the properties of the plasma plume produced by ultrashort pulsed laser ablation. As we already mentioned in the introduction, most of the experimental studies were devoted to the investigation of the excitation mechanisms and the structural changes experienced by the target material upon laser irradiation, both for fundamental physics[1] and for material science applications[2]. Investigation of carriers dynamics and relaxation paths[3], measurement of carriers to lattice coupling strengths[4], time evolution of surface reflectivity, absorption[5] as well as dielectric constant[6,7], have been performed to elucidate the physical phenomena occurring in a solid after ultrashort laser irradiation. Nonetheless, a clear understanding of all the mechanisms involved in the process is still lacking.

In this chapter the main results of the experimental investigation performed during the present thesis on ultrashort pulsed laser ablation are presented.

III.1 First insight of new physical phenomena

The experimental analysis of the ultrashort laser ablation plumes performed during the present thesis has benefited from the large experience acquired in the characterization of plasma plumes produced by nanosecond (ns) laser ablation and most of the employed techniques are similar to those applied in that case[8]. Thus, in the model of our previous studies[9], we started the characterization of the ultrashort laser ablation process by studying the spectroscopic properties of the plume produced by 100 fs Ti:sapphire laser pulses in high vacuum (residual pressure of $\approx 10^{-7}$ mbar) from a magnesium diboride (MgB_2) solid target. We followed the time evolution of the whole emission spectrum at several distances from the target by recording the ICCD signals at different gate delays after the laser pulse. But, in contrast with the spectroscopic features of MgB_2 plume produced with ns laser pulses, we found that while at short delays after the laser pulse the spectrum is made up of atomic emission lines, by increasing the ICCD gate delay a structureless broadband emission appears, which lasts for several tens of microseconds. Fig. 3.1

shows such a peculiar time evolution of MgB_2 emission spectrum recorded at d = 1mm from the target up to 10 μs after the laser pulse.

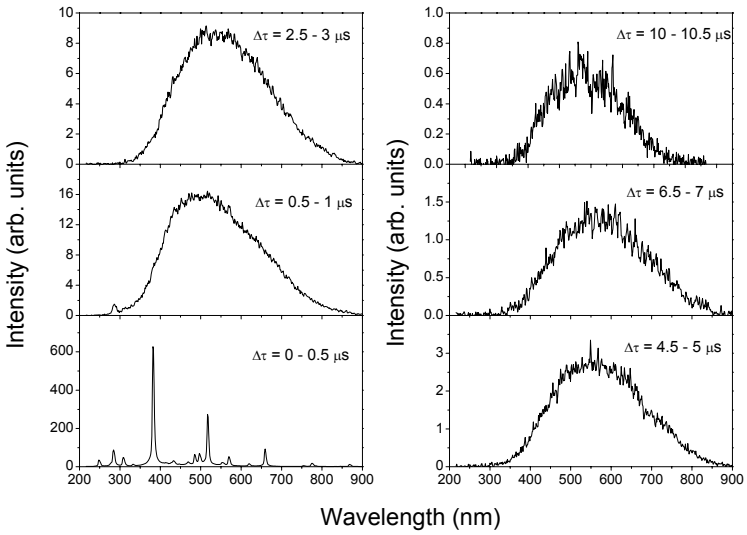

Fig. 3.1: Time evolution of MgB_2 emission spectrum in high vacuum, after irradiation with 100 fs Ti:sapphire laser pulses. The gate width was 0.5 μs, at a laser fluence of ≈2 Jcm^{-2}.

This unexpected feature couldn't be ascribed to MgB_2 molecular structures, owing both to the lack of molecular bands in the spectral range of concern here and to the duration of the emission, too long for typical atomic and molecular emission processes. Thus, we were forced to ascribe this continuum emission to non-atomic species, namely aggregates of particles produced during the ultrashort laser ablation process. This interpretation was supported by some studies describing blackbody-like photoluminescence radiation coming from nanoparticles produced by Plasma Enhanced Chemical Vapour Deposition (PECVD)[10,11] and Chemical Vapour Deposition (CVD)[12]. Besides, we found signs of such features just during femtosecond laser ablation experiments in vacuum in a paper by Albert and al.[13] appeared in the literature during our first investigations, in the middle of 2003. Here, the authors observed by time resolved spectroscopy and fast imaging three velocity populations emerging from a Ti target after fs laser irradiation, the slower of which made of nanoscale clusters.

Thus, in addition to the timeliness of ultrashort laser ablation as a novel material processing technique and to the extreme interest around the physical mechanisms governing the process, the understanding of nanoparticles production mechanisms in vacuum attracted great attention and became one of the main goals of the present thesis.

In fact, nanoparticles production by laser ablation technique is currently performed by means of ns laser systems, just by letting the plume to expand in an inert gas atmosphere: the collisions between the ablated atoms and the buffer gas give rise to vapour condensation and, then, to cluster formation. On the contrary, ultrashort laser ablation provides nanoparticles directly in vacuum (see section III.3) without any backing atmosphere, thus appearing as an extremely versatile technique to particles production.

Actually, during nanosecond laser ablation under suitable experimental conditions, production of *micrometric* particles as liquid droplets coming from the melted target material has been frequently reported,[14] while Atomic Force Microscopy (AFM) allowed us to check the actual *nanometric* character of the aggregates produced by ultrashort pulses, as reported in section III.3. The limited sizes (on average 10-20 nm of radius) and the quite narrow size distributions of nanoparticles found for each investigated material and experimental condition confirm the extreme newness of the process and open new perspectives in the field of laser-matter interaction.

Moreover, all the techniques currently employed to synthesize nanoparticles require to find for each material a set of optimal experimental parameters to get an efficient production, thus being strongly material dependent; for instance, with ns laser ablation technique is necessary to achieve time by time the right balance between the gas pressure and the target to deposition substrate distance, while chemical and electrochemical techniques need of specific reagents and reactions for a good material processing. On the contrary, as evidenced by both optical measurements (section III.2) and AFM (section III.3), ultrashort laser ablation provides nanoclusters directly from the target material, in vacuum, without any further experimental improvement, thus turning out to be an universal route for nanoparticles production from any target material (metals, semiconductors, multicomponents and so on) and appearing as a very powerful and promising technique for technological applications. Then the specific structural properties of matter turn out to weakly influence the morphological properties of the produced nanoparticles, which are ejected with similar features whatever the ablated material is.

Hence, a deep characterization of the plume properties and dynamics is of great present interest both to elucidate the main properties of all the ejected particles (ions, atoms and nanoparticles) and to shed a light on their formation mechanisms, as widely reported in the next sections.

III.2 Plume dynamics characterization

In this section, the main features of the plume dynamics after ultrashort laser irradiation are reported. In particular, subsection A deals with the experimental results by Optical Emission Spectroscopy and Langmuir probe, while subsections B and C tell about the radiative cooling processes characterizing nanoparticles expansion in vacuum and the ejection mechanisms of both ions, atoms and nanoparticles, respectively. Finally, in subsection D the plume characterization by Fast Photography technique is reported.

A. Optical Emission Spectroscopy (OES) and Langmuir Probe (LP)

The features shown in Fig. 3.1 at *d=1mm* were found also at longer distances with similar characteristics. We performed time-gated Optical Emission Spectroscopy (OES) of magnesium diboride plumes at five more distances (3, 5, 7, 10 and 13 mm); at each distance, the temporal evolution of the whole emission spectrum has been followed by recording through the ICCD camera the emitted signal integrated over 0.5 μs (gate width) at consecutive time delays with respect to the laser pulse.

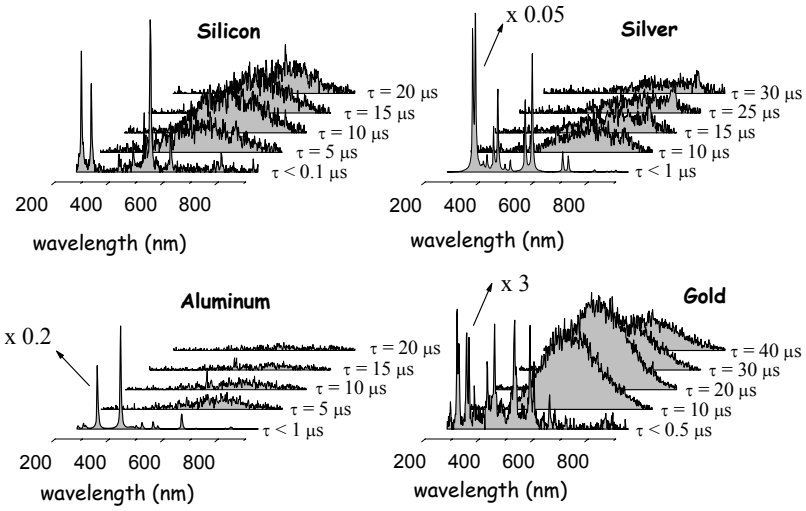

Fig. 3.2: Time evolution of emission spectra coming from 100 fs Ti:sapphire laser ablated plumes of different target materials at P = $1x10^{-7}$ mbar and a distance from the target of 1mm. The gate widths were 100ns for atomic spectrum and 5μs for continuum emission. Each picture corresponds to a fluence about twice the threshold for laser ablation. The vertical scale is the same.

The final picture is that the atomic spectrum always vanishes within about few microseconds, while the broadband emission lasts for several tens of microseconds.

To better understand the origin and the nature of this feature we investigated by time-gated optical emission spectroscopy the emission spectra of the plumes produced by ultrashort laser ablation from several elemental target materials, both metals (Au, Ag, Al) and semiconductors (Si), as the simplest systems to study. We found again the same features at several distances from the target, thus confirming the universality of the process despite the specific structural properties of the target. By choosing time by time the suitable gate width to have a good signal to noise ratio both for atomic and for continuum emission, we obtained the picture well summarized in Fig. 3.2.

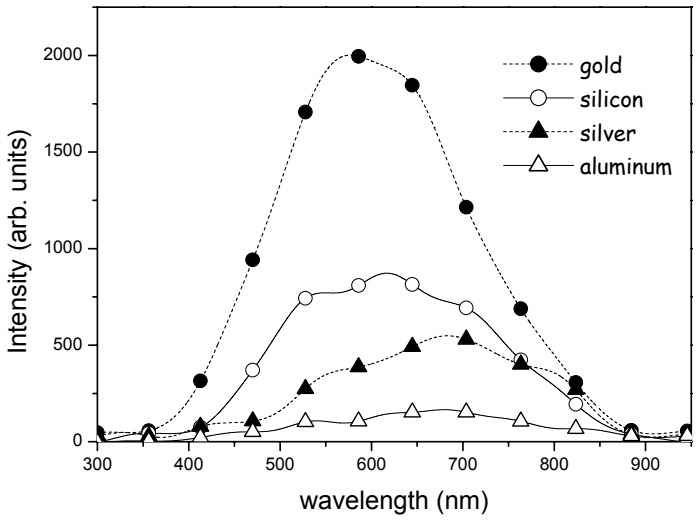

Fig. 3.3: Comparison of the non-atomic spectra emitted by different materials after 10 μs from the laser pulse and with a gate width of 5 μs, at almost the same laser fluence (0.6 <F< 0.8 Jcm^{-2}). All the curves were smoothed to reduce the noise.

As easily seen in the picture, even if the broadband emission seems to be an universal characteristic of the ultrashort laser ablation process, the specific appearance of the emitted spectra shows some material dependent features. Though atomic spectra are always stronger than the non-atomic ones (in Fig. 3.2 the broad emission is integrated over a time interval 50 times larger than for atomic spectrum thus appearing more intense), the amount of continuum emission varies with the material; among metals, in particular, gold continuum in each time window is clearly much intense than the silver and aluminum one, at almost the same fluence, in spite of their common metallic character (Fig. 3.3).

These features seem to be almost fluence insensitive, thus turning out to be strongly correlated to the parameters which rule the interaction between the laser light and the specific material more than to the particular ablation regime (which is determined only by the laser fluence). Nonetheless, it is worth noticing that even if the appearance of the broadband spectra slightly differs among the different materials, their occurrence at each investigated fluence and for whatever ablated material reveals the universality of the process of aggregates ejection and, thus, its independence from specific structural properties of solid state matter.

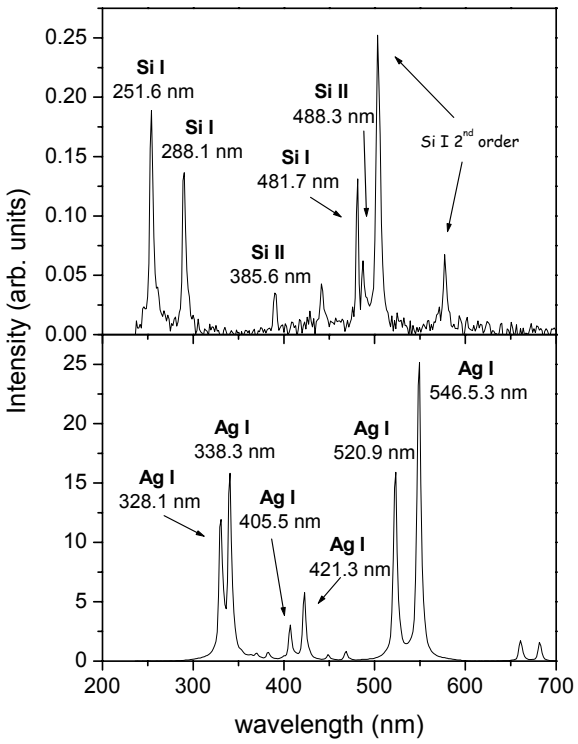

Fig. 3.4: Typical atomic emission spectrum of the plume. The case of silicon and silver are shown. The spectra refer to the first 50ns after the laser pulse.

To better characterize the plume emission, we studied the temporal evolution of both the atomic and the non-atomic spectrum, by integrating the emission of selected atomic and ionic lines as well as of the whole continuum spectra at different time delays with respect to the laser pulse. In Fig. 3.4 typical atomic spectra, with the indication of the neutral and ionic emission lines, are shown in the case of silicon and silver. The spectra show the plume optical emission integrated over the first 50 ns after the laser pulse. While the silicon plume turns out to be clearly made of both neutral and ionic lines, from Fig. 3.4 the silver emission seems to be due only to neutral atoms de-excitation. This feature was found also for all the other investigated metals. Actually, for all metals the ionic optical emission turned out to decay very fast during the first few tens of ns after the laser pulse, thus preventing a complete characterization of the ionic temporal dynamics. Thus, the temporal evolution of the ionic content of the plume was studied also by means of the Langmuir probe apparatus.

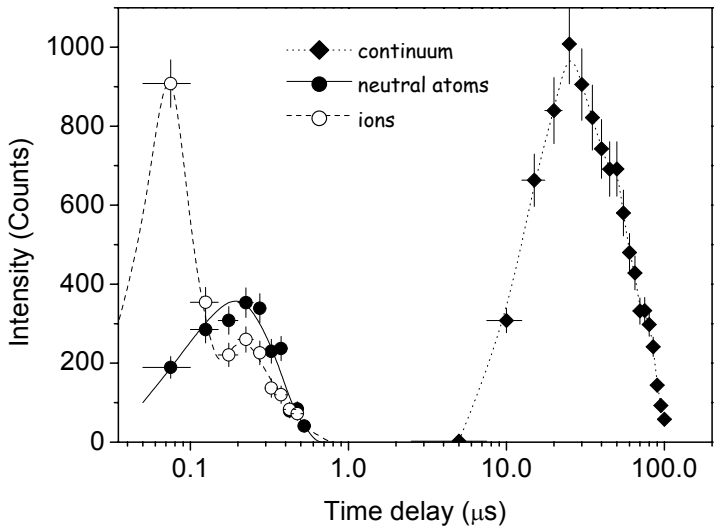

Fig. 3.5: Comparison of the temporal evolution of the species in the plume, at a fixed distance from the target (7mm), as obtained by OES in the case of silicon. The signals are normalized to their respective acquisition gate widths (50 ns for atoms and ions, 5μs for continuum). See the text for further details.

In Fig. 3.5 the temporal dynamics of the species in the plume as obtained by OES measurements is shown in the case of silicon. The points were obtained by integrating at a fixed distance from the target (7mm) the emission under selected lines for atomic species (252 nm for Si I, while 488 nm and 385 nm were summed for Si II) and the whole continuum emission for the aggregates. By plotting these points as a function of the time delay, the plume clearly turns

out to be made of several populations: a fast ionic component, with an average velocity of ≈ 10 cm/μs, a slow ionic component travelling together with the neutral atoms at an average velocity of ≈ 1 cm/μs and, finally, the slowest non-atomic component moving at an average velocity of ≈ 0.01 cm/μs.

The temporal distributions shown in Fig. 3.5 may be turned to velocity distributions. If *F(v)* is the velocity distribution of the species in the plume (so that *F(v)dv* is the number density of particles with velocity in the range *v, v+dv*), the conservation of the number of particles gives[15]

$$\int_{\infty}^{0} F(v)dv = \int_{0}^{\infty} S(t)dt \qquad \Rightarrow \qquad \int_{0}^{\infty}\left[F(v)\frac{dv}{dt} + S(t) \right]dt = 0 \tag{3.1}$$

where *S(t)* is the temporal signal measured by the detector (emission intensity in the case of OES). Since eq. (1) is valid at every time delay *t*, we simply obtain

$$F(v) = -\frac{dt}{dv}S(t) = \frac{L}{v^2}S(t) \tag{3.2}$$

being *L* the distance travelled by the particles to reach the detector and *v* their drift velocity assumed to be constant (at the investigated distances and times the plume expansion is practically already unhindered). Fig. 3.6 shows the normalized velocity distributions calculated by eq. (3.2) for gold neutral atoms and aggregates, starting from their temporal distributions obtained by OES. The velocity gap between the fast atomic and the slower cluster populations is clearly evident, ranging from about one to two order of magnitude.

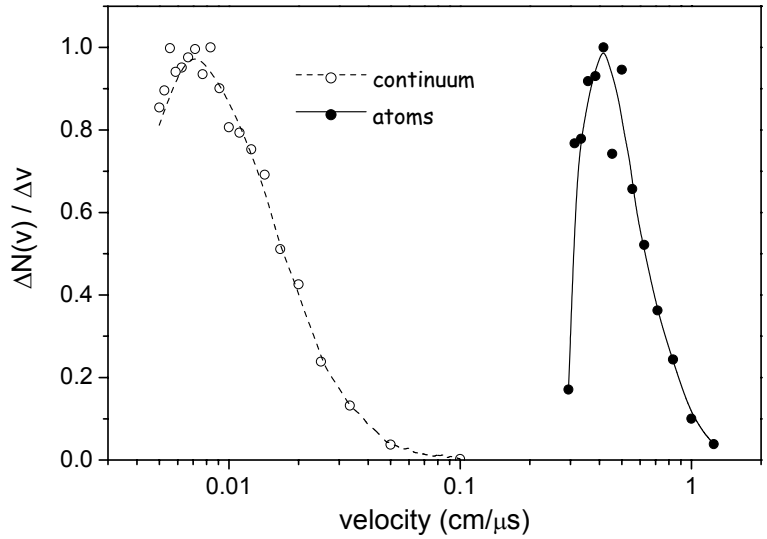

Fig. 3.6: Normalized velocity distributions of the species in the plume, at a fixed distance from the target (3mm), as obtained by eq. 3.2 from OES temporal distributions for gold.

Indeed, these different velocity patterns indirectly confirm the presence in the expanding plume of aggregates of thousands of atoms. In fact, as the emitted species gain their expansion velocity from thermal energy through collisions occurring in the Knudsen layer, this leads to an expansion velocity dependence on mass of the kind $m^{-1/2}$. Such dependence lies on the assumption of local thermal equilibrium (LTE) among different species in the plume already from the first stages of its expansion; though not exactly correct, this assumption allows to derive a rough estimation of the clusters radii. In fact, from a direct comparison between the observed velocities of the atomic and the non atomic components of the plume reported in Fig. 3.6, we can estimate the mass of the gold clusters and, then, the number of atoms in the cluster as $n_{cl} \approx 10^4$. By describing the cluster properties by means of a liquid drop model[16], we may roughly estimate the cluster radius as $a = r_W n_{cl}^{1/3} \approx 5\,\text{nm}$, where $r_W = 1.6$ is the Wigner-Seitz radius for gold[17]. Thus the non-atomic features found during OES characterization of the plume have to be ascribed to nanometric aggregates of thousand of atoms, and not to micrometric droplets as in the case of ns laser ablation. This aspect suggests the occurrence of mechanisms completely new and unusual for laser ablation experiments and which are a direct consequence of the extreme non equilibrium conditions to which the target material is driven by the ultrashort pulse irradiation, as reported also in subsection C.

The ionic velocity distributions for metals have been calculated starting from the temporal dynamics of the charge collected at the Langmuir probe. Nevertheless, while OES signals are proportional to the number of emitting particles in the investigated volume of the plume (so that *S(t)dt* is the density of emitting particles in the time interval *dt*), the Langmuir probe measures a signal *J(t)* proportional to the flux of particles crossing its sensitive area (so that *J(t)dt* is the number of ions crossing the unit surface of the probe in the time interval *dt*). Then, to employ eqs. 3.1-3.2 to obtain the ionic velocity distributions *F(v)* we may simply turn the density flux *J(t)* into the number density *S(t)* by dividing it by the velocity of the ions *v=d/t*, being *d* the target-to-probe distance.

Thus, eqs. 3.1-3.2 become

$$\int_{\infty}^{0} F(v)dv = \int_{0}^{\infty} S(t)dt = \int_{0}^{\infty} \frac{J(t)}{v} dt \qquad \Rightarrow \qquad \int_{0}^{\infty} \left[F(v)\frac{dv}{dt} + \frac{J(t)}{v} \right] dt = 0 \tag{3.3}$$

so

$$F(v) = -\frac{dt}{dv}\frac{J(t)}{v} = \frac{d^2}{v^3} J(t) \tag{3.4}$$

Figure 3.7a,b show the temporal profile of the ion signal at the probe and the corresponding velocity distribution according to eq. 3.4, respectively, in the case of gold for a target-to-probe distance of 5.8 cm. In accordance with the features shown in Fig. 3.5 in the case of silicon, the current signal points out the presence of a double ionic population in the plume, made of fast ions with velocities of tens of cm/μs and slow ions with an order of magnitude lower velocities. These velocities correspond to kinetic energies up to several keV, in contrast with the tents of eV possessed by the aggregates. From Fig. 3.7a the signal due to fast ions turns out to be stronger than the signal related to slow ions; indeed, this is due to the fact that Langmuir probes measure ion fluxes (velocity × density) thus strongly enhancing the signal of faster species. Actually, it is well known that the fast ions content is only about the 10-20% of the total ionic amount of the plume, as already reported in the literature[18,19] in similar experimental conditions.

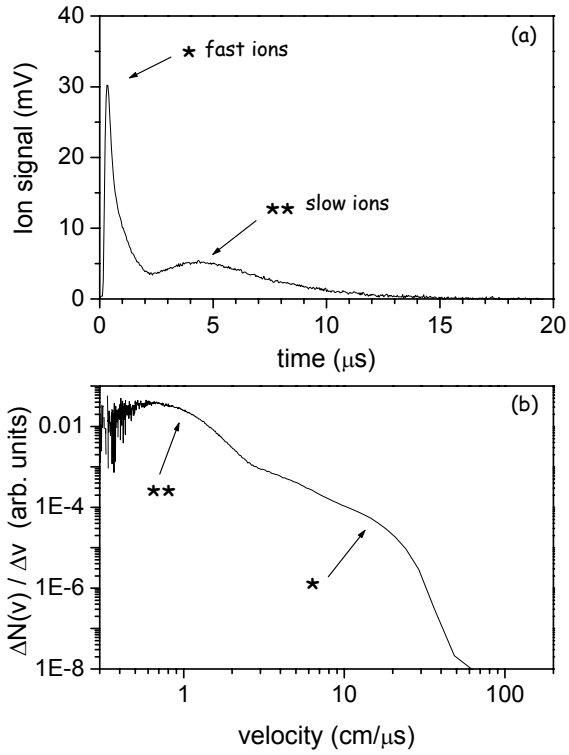

Fig. 3.7: Ions temporal dynamics (a) and corresponding velocity distributions (b) for a gold plume produced by 100fs Ti:sapphire pulses at a laser fluence of about 0.7 Jcm^{-2}, as obtained by Langmuir probe measurements.

Thus, the ion population turned out to be made of two main velocity components. Kinetic energies of faster ions may reach several keV, in contrast with the tens of eV reached by the slowest ions and which are typical ion energies reached during nanosecond laser ablation experiments as a consequence of thermal, equilibrium mechanisms[20]. This suggests that during subpicosecond laser ablation several non-thermal, non-equilibrium mechanisms affect the ablated material just after laser light absorption, thus underlining the extremely newness of the laser-matter interaction in the ultrashort duration regime[21].

The picture so far outlined of ultrashort laser ablation deals with a process where several different velocity populations are generated as a consequence of laser-matter interaction. Ultrashort pulses very rapidly heat the target to temperatures close to the thermodynamic critical point before any significant expansion starts, thus generating a high temperature-high pressure fluid whose rapid expansion leads to the generation of excited atoms, ions and aggregates. These features turn out to characterize in general the ultrashort laser ablated plumes without strong dependences upon the structural properties of the target materials, thus telling about a process almost fully determined by the properties of the extreme non-equilibrium state

to which the system is brought by the laser irradiation, where no differences exist any more among the different materials, as we are going to better explain in subsection C.

B. Nanoparticles cooling by radiative emission

As we previously mentioned, the broadband continuum emission found by OES can be ascribed to blackbody radiation emitted by incandescent nanoparticles. Thus, time-gated optical emission spectroscopy allowed us to follow also the evolution of the nanoparticles temperature inside the expanding plume by measuring their emission spectra at different time delays and distances from the target surface, and then fitting them by a Planck-like radiation curve. To do this, the collected nanoparticles emission spectra have been corrected for the spectral response of the detection system (see chapter II) to obtain power spectra as those reported in Figure 3.8, where both the measured spectrum (full circles) and the corresponding corrected spectrum (open circles) are shown.

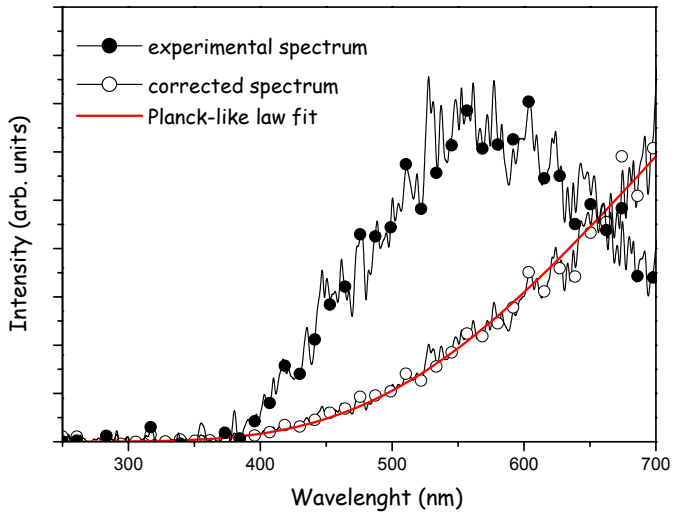

Fig. 3.8: Example of an experimental emission spectrum of gold nanoparticles (full circles), corrected by the response of the system (open circles) and fitted by a Planck-like radiation law (red line) according to eq. (3.5).

By taking into account that in the Rayleigh approximation (namely, for $2\pi a/\lambda < 0.3$, λ being the emission wavelength and a the particle radius) the nanoparticles emissivity $\varepsilon(a,\lambda)$ is proportional to a^3/λ, and that the ICCD detector measures photon fluxes, the power spectra can be reproduced by the following Planck-like function

$$I(\lambda,T) \propto \lambda^{-5}\left[\exp\left(\frac{hc}{\lambda k_B T}\right)-1\right]^{-1} \tag{3.5}$$

where h, k_B and c are the Planck and Boltzmann constants and the velocity of light, respectively. Fig. 3.9(a) shows the fits to the corrected emission spectra according to eq. (3.5) in a $I\lambda^5$ – $1/\lambda$ semi-logarithmic plot, for three different materials at a fixed distance and delay time with respect to the laser pulse irradiation. The agreement between the spectra (points) and the fits (full lines) is fairly good and confirm the thermal nature of the nanoparticles emission spectra. Moreover, eq. (3.5) allows to estimate the nanoparticles temperature as one of the fitting parameters, which turns out to be of the order of few 10^3 K at all the investigated delays and fluences. Thus, nanoparticles come out to be cooler than the excited atomic species which populate the plume, whose temperatures are typically one order of magnitude higher.

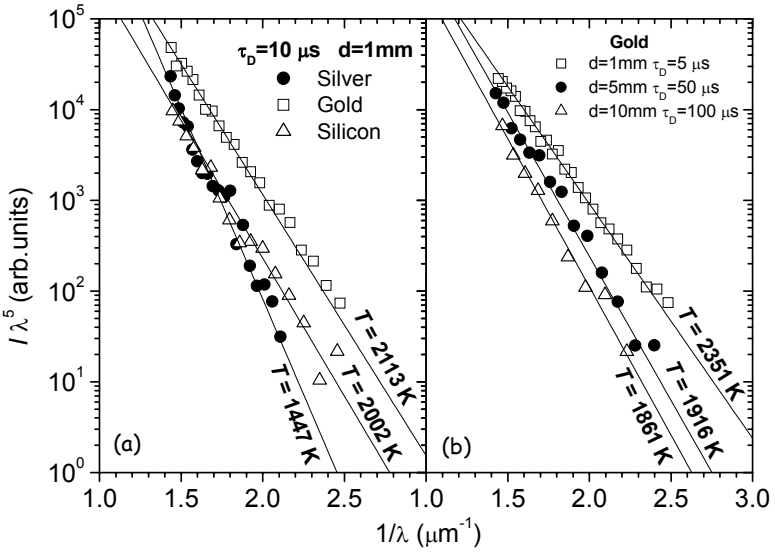

Fig. 3.9: (a) Surface temperature evaluation for three different materials at a fixed distance and delay time, and (b) cooling trends with time for a gold ensemble of nanoparticles travelling at a constant velocity of ≈9x10^{3}cm/s, in a $I\lambda^5$ – $1/\lambda$ semi-logarithmic plot. The points represent the emission spectra corrected and binned over a wavelength interval of ≈ 20nm to reduce the noise, while the full lines are the fits according to eq. (3.5).

The inspection of the time and space dependence of the estimated nanoparticles temperatures reveals the occurrence of cooling trends for almost all the investigated materials. Since nanoparticles expand at a constant velocity, as confirmed by optical emission spectroscopy

and fast photography measurements, it is possible to follow the cooling behaviour of a specific ensemble of particles moving at a constant velocity v by simply calculating their temperature at distance-related time delays $\tau = d/v$. For instance, Fig. 3.9(b) shows the cooling trend with time for a gold ensemble of nanoparticles travelling at a constant velocity of ≈ $9x10^3$cm/s. The observed cooling rate is of the order of ≈ 15 K/μs at τ = 10μs, and decreases to much smaller values at later times (*e.g.*, ≈ 2 K/μs at τ = 150μs).

Different cooling mechanisms influence the nanoparticles temperature evolution during their expansion into vacuum. At very short time delays (less than 1 ns), the plume evolution can be regarded as a one-dimensional adiabatic expansion, and the temperature evolution of the ejected material is dominated by hydrodynamic cooling, with quench rates exceeding 10^6 K/μs.[22] At later times, when the ejected material has travelled distances comparable to the laser spot diameter (typically 100 μm), the plume expansion progressively develops a three-dimensional (3D) character.[23] As the plume expands, its thermal energy is progressively transformed into kinetic energy, while its temperature and density rapidly drop down, until an inertial stage characterized by a constant expansion velocity is reached (typically at ≈ 1mm from the target surface).

At this late stage, the contribution of the hydrodynamic cooling to the temperature drop becomes negligible with respect to that of the other mechanisms.[24] In particular, the estimated hydrodynamic cooling rate drops down very rapidly from an initial value of the order of 10^6 K/μs at the beginning of the 3D expansion (less than 1 μs after the laser pulse) to values smaller than a few K/μs within 10 μs, namely, a value much smaller that those inferred by fig. 3.9b.

T (K)	Calculated cooling rates (K/μs)		
	RE	EV	TE
1000	0.9	<< 1	<< 1
1500	6.5	<< 1	1.2×10^{-4}
2000	28	1×10^{-6}	3.5×10^{-1}
2500	84	2×10^{-4}	47
3000	210	6×10^{-3}	1300

Table III.1: Cooling rates for radiative emission (RE), evaporation (EV) and thermoionic emission (TE) at different temperatures T in the case of silicon. Thermoionic emission has been evaluated for a nanoparticles final charge state of Z=+1. Radiative and thermoionic cooling rates have been obtained by averaging over the observed size distribution, while evaporation cooling rate refers to a nanoparticles with a radius of ≈10 nm.

Thus, at the longer temporal and spatial scales of concern to the present study, other cooling mechanisms such as radiative emission, particle evaporation, and thermoionic emission, have to be considered. By applying to our experimental conditions the analytical results of

nanoparticles cooling models[25,26], and by taking into account the typical nanoparticles size distribution measured by AFM (see section III.3), we have estimated the typical order of magnitude of the rates of the above cooling mechanisms at various temperatures, which are resumed in Table III.1. While evaporation cooling turns out to be negligible at all temperatures, thermoionic emission prevails over radiative emission only for temperatures higher than ≈ 2500 K. Thus, at the nanoparticles temperatures observed in our experiment (see Fig. 3.9), radiative emission is the main cooling mechanism, and the estimated cooling rates are in good agreement with the observed ones.

The radiative emission cooling can also be computed by considering a simple system constituted by an ensemble of non-interacting spherical nanoparticles in vacuum, and at temperature *T*. Then the temperature time evolution is obtained from the energetic balance

$$< C_{cl} \frac{dT}{dt} >= -\pi < \int_0^\infty J(a,\lambda) d\lambda > \tag{3.6}$$

where π takes into account the integral over the full solid angle, < > represents the average over the nanoparticles size distribution (experimentally estimated by Atomic Force Microscopy, see the section III.3), C_{cl} is the nanoparticle heat capacity, and

$$J(a,\lambda) \propto \varepsilon(a,\lambda)\lambda^{-5}\left[\exp(\frac{hc}{\lambda k_B T})-1\right]^{-1} \tag{3.7}$$

is the nanoparticles power spectrum. At sufficiently high temperature and for a large number of atoms in the nanocluster, $n_{cl} >> 1$, the particle heat capacity is given by the Dulong and Petit law, $C_{cl}=3n_{cl}k_B$. Thus, by considering a liquid drop model where $n_{cl} \propto a^3$, the balance in eq. (3.6) is independent of the particle radius *a*. Finally, the time dependence of the nanoparticles temperature can be obtained by integration of eq. (3.6) as

$$T(t) = \frac{T_0}{\sqrt[4]{1+4\beta_{cl}T_0^4 t}} \tag{3.8}$$

where β_{cl}, a dimensional parameter depending on the imaginary part of the nanoparticles volume polarizability, is the only fitting parameter. Fig. 3.10 reports on the temporal

dependence of the temperature of an ensemble of nanoparticles travelling at a velocity of ≈ $9x10^3$cm/s; the continuous line is the plot of eq. (3.8), and turns out to reproduce very satisfactorily the experimental time dependence. Similar features for the emission spectra and temperature evolution have also been observed for other sets of particles propagating with different velocities, at all the investigated fluences (up to 2.0 J cm^{-2}).

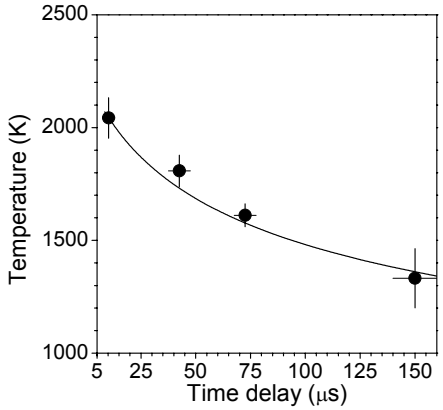

Fig. 3.10: Temporal evolution of the temperature of an ensemble of silicon nanoparticles travelling with a costant expansion velocity of 6×10^3 cm/s. Horizontal error bars indicate the temporal gate used for the spectrum acquisition, while vertical error bars give the statistical uncertainty in the temperature obtained by the curve fitting procedure. The continuous line is the plot of eq. (3.8).

Thus, nanoparticles turn out to cool very rapidly toward a temperature of about 10^3 K in a time lag of about few 10^2 μs. Notwithstanding, such a cooling behaviour has not been always observed in our experiments, as for instance happened for silver and aluminum where the estimated temperatures were almost constant around a value of 1-1.5 $x10^3$ K at all the investigated fluences.

Actually, when the nanoparticles temperature drops down the corresponding emission spectra move towards the region of higher wavelengths, according to the Wien's displacement law, thus going towards the spectral region not measurable by our OES apparatus which is able to detect the emission signals in a spectral range up to about 900 nm. Then, when the temperature becomes too low (around $1x10^3$ K), the corrected spectra belong just to the tail of the fitted Planck-like power distributions and are less sensitive to temperature changes, due to an higher signal to noise ratio. That is why further cooling of nanoparticles below these temperature values is not well detectable by our experimental setup, what happens after several tens of μs for most of the investigated materials and after few μs in the case of aluminum and silver.

Thus the observed discrepancy in the nanoparticles temperatures among the different investigated materials, in the same experimental conditions, could be considered responsible of the different emission intensities of their continuum emission spectra, as well shown in Figs. 3.2-3.3. We are currently studying why the temperature values derived by the nanoparticles power spectra are lower for some materials at all the investigated fluences and how this is linked to the mechanisms of their formation as a consequence of the laser matter interaction in the ultrashort pulse regime. Notwithstanding, these discrepancies turn out to have no influence onto the morphology of the produced nanoparticles, as clearly shown by the atomic force microscopy measurements reported in the section III.3.

C. Ablation yields and plume formation mechanisms

The ultrashort laser ablated plumes thus turned out to be a very complex physical system, being made of several species characterized by different velocity distributions. The experimental investigation of the ablation mechanisms involved in such a complicated laser-matter interaction regime is the subject of the present section. To this end we studied the behaviour of the ablation yield as a function of the incident laser fluence separately for atoms, ions and nanoparticles, both by OES and LP techniques. These trends were obtained by integrating at each fluence the optical emission spectra or the collected charge signals, respectively, over the whole plume temporal dynamics.

Nanoparticles – In Fig. 3.11 the fluence dependences of the OES ablation yield for nanoparticles and neutral atoms are compared, for a silicon target. As readily observed, in both cases two ablation regimes can be identified, each characterized by a logarithmic dependence.

Such a behaviour is well known to hold for ultrashort laser ablation experiments and can be easily depicted by means of the two temperature model.[27,28] Actually, by neglecting both electron thermal diffusion and electron to lattice coupling during the stage of laser pulse heating, the maximum attainable lattice temperature after the laser pulse is roughly given by

$$T_i^{\max} = \frac{F_a \alpha}{C_i} \exp(-\alpha z) \tag{3.9}$$

where F_a is the absorbed laser fluence, α is the material absorption coefficient and C_i is the lattice heat capacity. A significant material evaporation occurs when $C_i T_i$ becomes larger than $\rho\Omega$, where ρ is the density and Ω is the specific heat of evaporation per unit mass.

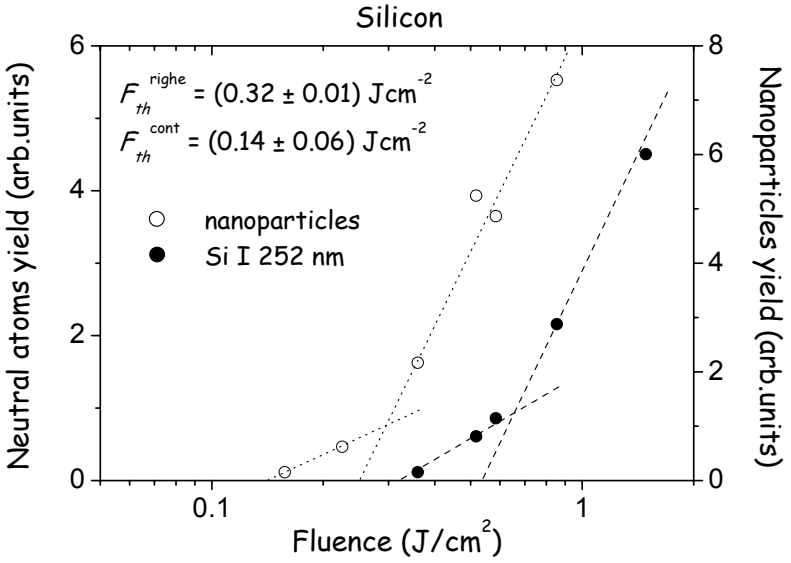

Fig. 3.11: Fluence dependence of the ablation yield for nanoparticles (open circles) and for the neutral silicon optical emission at ≈252nm (full circles) for ≈800nm, ≈120fs laser pulses and at 3mm from the target.

Using eq. (3.9) the condition for material evaporation takes the form $F_a \geq F_{th,1} \exp(\alpha z)$, where $F_{th,1} \approx \rho\Omega/\alpha$ is the fluence threshold, and hence the ablation depth per pulse is

$$L \approx \alpha^{-1} \ln(F_a / F_{th,1}) \tag{3.10}$$

Thus, the ablation depth dependence upon the absorbed laser fluence on a semi-logarithmic scale is linear, with the ablation threshold $F_{th,1}$ and the optical penetration depth α^{-1} as fitting parameters. Nevertheless, the behaviour predicted by eq. (3.10) becomes no longer valid by increasing the laser fluence, being replaced by a second logarithmic dependence

$$L \approx l_{th} \ln(F_a / F_{th,2}) \tag{3.11}$$

characterized by a higher energy penetration depth l_{th} (named the "thermal penetration depth") and a higher fluence threshold $F_{th,2}$. By assuming that the amount of excited and ionized species

in the plume is somehow proportional to the ablation depth, eqs. (3.10-3.11) can be safely used to reproduce the fluence dependences of the ablation yield obtained by OES and Langmuir probe measurements.

Actually, the occurrence of two ablation regimes was already predicted by eq. (1.3); thus, eq. (3.10) is valid in the *low fluence* regime which is determined by the absorption of the laser light just in the shallow surface layer of depth α^{-1}, as predicted by the Lambert-Beer absorption law, while eq. (3.11) describes what occurs in the *high fluence* regime where electron thermal diffusion sets in and absorption of the laser energy is accomplished across a deeper layer of depth l_{th}. It is worth noticing that the ablation threshold for material ejection to occur is given by the threshold value in the low fluence regime, $F_{th,1}$.

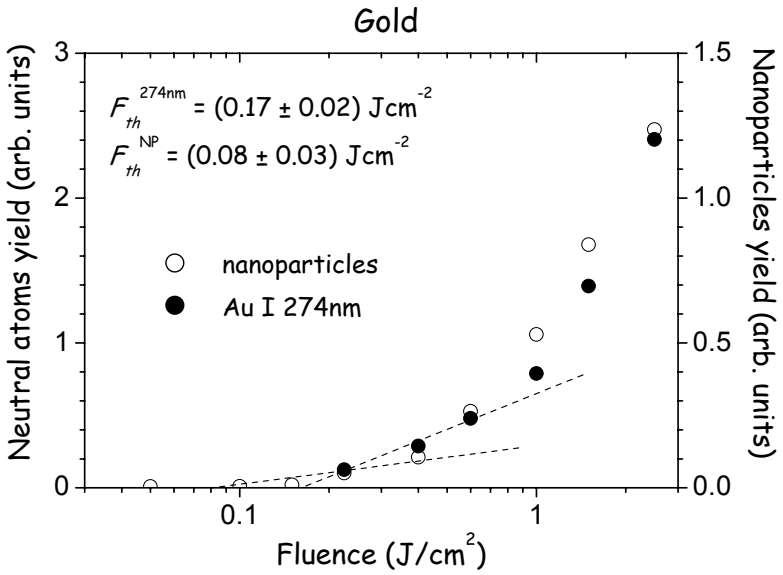

Fig. 3.12: Fluence dependence of the ablation yield for nanoparticles (open circles) and for the neutral gold optical emission at ≈274nm (full circles) for ≈800nm, ≈120fs laser pulses and at 3mm from the target. For the sake of clarity, only the fits to the low fluence trends are shown.

Thus, Fig. (3.11) clearly underlines the existence of two different ablation thresholds for nanoparticles and neutral atoms, in the low fluence regime. In particular, the threshold for nanoparticles ejection is the lowest and is very close to the so called "damage threshold" for silicon ($F_{dam} \approx 0.15$ Jcm^{-2}) reported in the literature by several authors and related to the onset of surface modifications due to several mechanisms.[29,30] In particular, an important phenomenon occurring at this energy densities is an ultrafast semiconductor-to-metal transition carried out by the high density of free carriers reached by the material upon laser irradiation, as already mentioned in chapter I. On the contrary, the threshold for atoms ejection is very close

to the fluence value for material ablation to occur ($F_{abl} \approx 0.3$ Jcm^{-2}) as reported in the literature[31].

Therefore, while atoms seem to be produced as a consequence of the thermal energy exchange inside the material over a several tens of picosecond timescale, which is then responsible of material ablation, nanoparticles turn out to come from the extreme non-equilibrium conditions set in by the laser irradiation over a few picosecond timescale, before any energy thermalization in the bulk material has occurred. Actually, Fig. 3.12 reports the same measurements as for silicon, in the case of a gold target. In agreement with the phenomenology found for silicon, we observed different low fluence thresholds for nanoparticles and neutral atoms; in particular the threshold for nanoparticles ejection is lower than that for atoms, which in its turn agrees well with the value of ablation threshold for gold of ≈ 0.17 Jcm^{-2} reported in the literature.[32]

Thus nanoparticles seem to come out always at lower fluences with respect to neutral atoms, both for metals and semiconductors. This could suggest that nanoparticles are generated by a different mechanism with respect to neutral atoms. According to the picture depicted in section I.2, different mechanisms may simultaneously contribute to ultrashort laser ablation. In particular, while complete vaporization could be considered as the main process responsible for the ejection of ions and neutral atoms, nanoparticles production may result from the simultaneous occurrence of spallation, phase explosion and fragmentation mechanisms. Actually, from Fig. 1.4 in chapter I it clearly turns out that at the lowest laser fluences, when the amount of energy delivered to the system is not very high, fragmentation processes are less probable to occur than phase explosion and spallation, and then cannot account for nanoparticles ejection at very low fluences. Moreover, phase explosion concerns the coexistence of both liquid and vapour phases[33] and, consequently, it is in its turn likely to be not responsible for nanoparticles production under the threshold for atoms ejection. Thus spallation, which does not consist of any vapour phase[33], could be suggested as one of the main processes leading to the ejection of nanoparticles at very low fluences, under the threshold for atomic laser ablation. Notwithstanding, a clear experimental evidence of this does not exist at the moment.

Certainly, the inspection of the fluence dependences of the ablation yield for nanoparticles allows to rule out any in flight condensation mechanism as responsible for cluster production; in fact, the occurrence of nanoparticles ejection under the threshold for atomic species ablation clearly indicates that clusters come directly from the target as a consequence of the extreme, non-equilibrium conditions created after ultrashort laser irradiation. Furthermore, the mechanisms

for cluster production turn out to be almost universal, that is not influenced by the structural properties of the target, and valid both for metals and semiconductors. This could be probably ascribed to the previously mentioned ultrafast metal transition occurring in semiconductors; actually, few picoseconds after the laser pulse irradiation no differences exist any more between metals and semiconductors, being more appropriated to deal with a "metallic fluid". Therefore it clearly turns out that nanoparticles are produced directly from the target in a rather general way, simply as a consequence of the peculiar laser-matter interaction in the ultrashort pulse regime, whatever the target material is, as already suggested by the optical emission characterization of the plume.

Ions - In Fig. 3.13 the ablation yield trends for the ionic content of the silicon plume are shown separately for the fast and the slow components detected by the Langmuir probe. Again, two fluence trends can be clearly distinguished and safely ascribed to the competition between the absorption in the optical skin depth and the onset of electron thermal diffusion inside the bulk material.

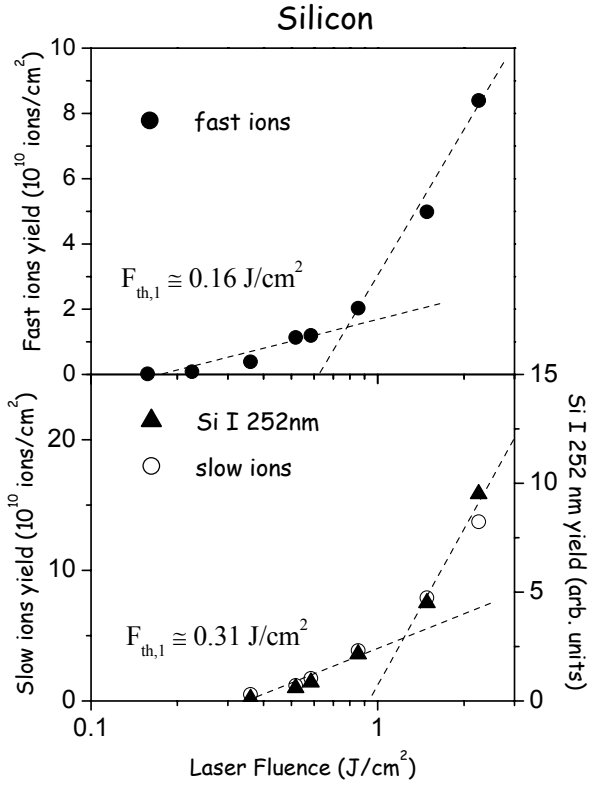

Fig. 3.13: Ablation yield dependence upon the laser fluence of the fast (full circles) and the slow (open circles) components of the silicon plume, at a probe to target distance of ≈5.8mm, for ≈800nm, ≈120fs laser pulses. The ablation yield trend for the neutral silicon optical emission at ≈252nm is also shown for comparison (full triangles).

The fluence threshold for slow ions is very close to the usual ablation threshold for silicon, as shown in the lower panel of Fig. 3.13 where the ionic signal is compared with the OES signal of the neutral silicon emission at ≈252nm.

On the contrary, the fluence threshold for fast ions production turned out to be quite lower than that for neutral atoms ejection and very close to that for non-thermal surface damage (F_{dam} ≈ 0.15 Jcm^{-2}), as in the case of nanoparticles.

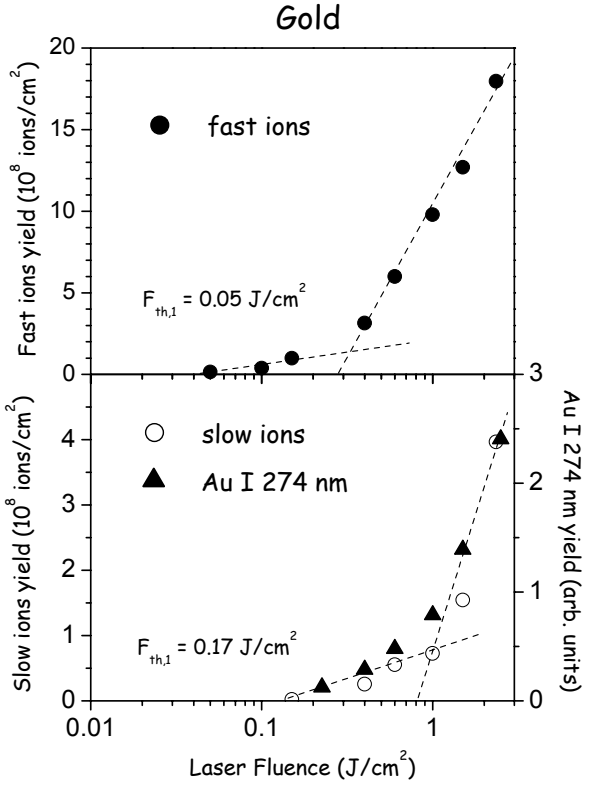

Fig. 3.14: Ablation yield dependence upon the laser fluence of the fast (full circles) and the slow (open circles) components of the gold plume, in the same experimental conditions as Fig. 3.10. The ablation yield trend for the neutral gold optical emission at ≈274nm is also shown for comparison (full triangles).

The appearance of fast, high energy ions in the ultrashort laser ablated plumes had been already reported in the literature in the case of metals.[19,21] Here, the same features have been observed in a semiconductor material.[18] A comparison of the ions temporal dynamics at the Langmuir probe for metals (gold and silver) and semiconductors (silicon) clearly underlines the occurrence of general, material insensitive, mechanisms for the ion production, as shown in Fig. 3.15; the slower peaks are distributed according to the different masses of the species (the lighter silicon

ions are the faster), while for the high energy peaks the distance to probe was probably too short to appreciate any time lag among them.

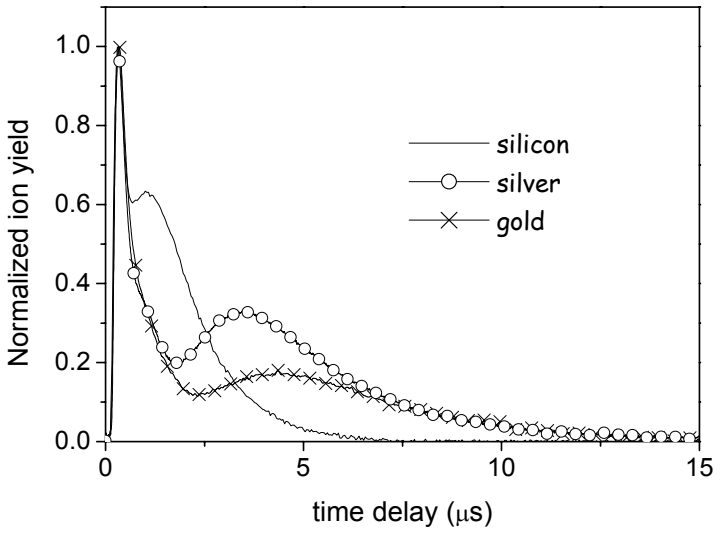

Fig. 3.15: Normalized Langmuir probe signals for three different materials at the highest investigated fluence (≈2.5 Jcm^{-2}) in the same conditions as Fig. 3.13-3.14.

Several mechanisms have been addressed to explain the appearance of a double ionic population in ultrashort laser ablation experiments, as space-charge effects[21] or coulomb explosion mechanisms.[19] Space-charge effects assume the high energy component to be a fraction of the plume ions accelerated by ambipolar fields set in by the escape of fast electrons at the plume edge, while the core of the plume remains essentially neutral; thus, such a mechanism cannot completely explain alone the appearance of a fast component below the ablation threshold, where the plume has not yet formed. On the other hand, coulomb explosion has never been widely taken into account to explain the mechanisms of ultrashort laser ablation in metals, in the fluence range of concern here, nor experimentally proved, except in few papers[34], while is sometimes addressed as one of the ablation mechanisms in the case of semiconductors.[35,36] However, our measurements suggest the occurrence of an "universal" mechanism, valid both for metals and semiconductors, and which could be probably justified again through the ultrafast metal transition occurring in semiconductors. Nonetheless, we are not able at the moment to definitively single out the right mechanism to fully explain our experimental results.

D. Fast Photography

Fast photography measurements allowed us to follow the vacuum expansion of the plume as a whole, as well as of the different velocity populations, by acquiring single-shot photographs of the plume emission in the x–z plane (axes parallel and perpendicular to the target surface, respectively), with an intensified charge-coupled device camera (ICCD), equipped with a 1024 × 1024 array, with a 3:1 magnification. To reduce the noise, a 2× binning was operated during image acquisition thus obtaining a spatial resolution of ≈100 μm. Hence, we studied the morphology and the expansion properties of the different plume populations by comparing the emission from two materials, silicon and nickel, induced by two laser sources, the fundamental and the 2nd harmonic of the Nd:Glass laser system described in chapter II.

Figs. 3.16-3.17 report a time series of the silicon plume emission at both laser excitations.

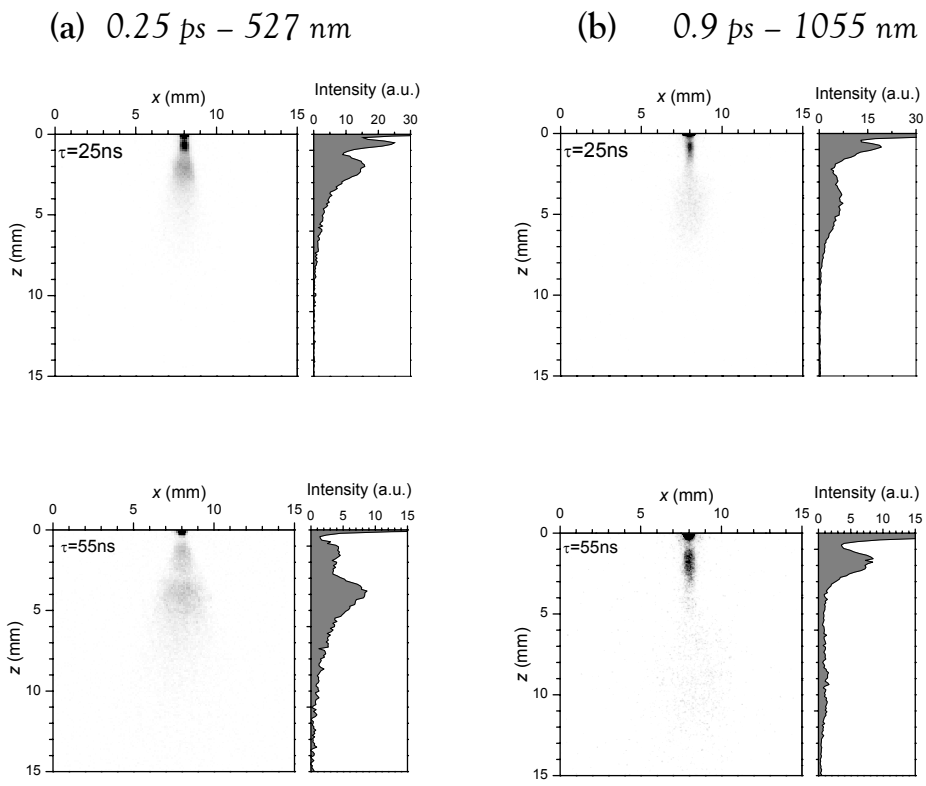

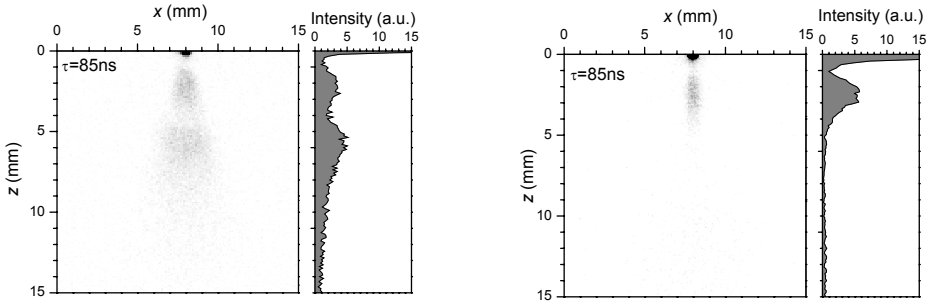

Fig. 3.16: Silicon plume expansion images at different time delays τ: (a) 0.25 ps/527 nm (left hand column), and (b) 0.9 ps/1055 nm (right hand column) laser pulses, at a laser fluence of 0.75 J/cm^2. Each image was recorded using a nominal 10 ns time gate on the intensifier of the camera. The positions at z = 0 mm define the front face of the target. Each picture is accompanied by the an intensity profile obtained by integrating the image signal along the x direction.

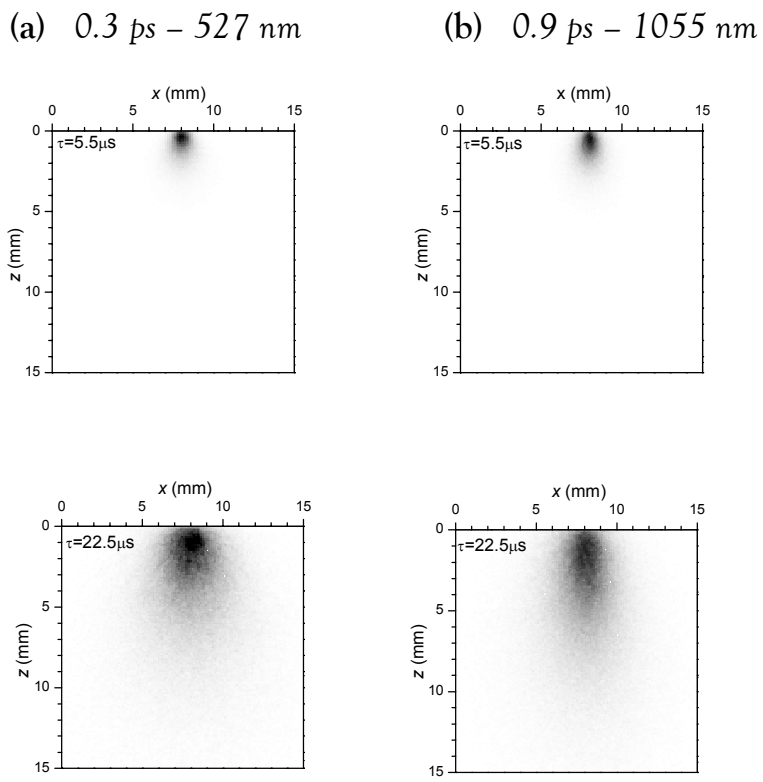

Fig. 3.17: Silicon plume expansion images at different time delays τ: (a) 0.25 ps/527 nm (left hand column), and (b) 0.9 ps/1055 nm (right hand column) laser pulses, at a laser fluence of 0.75 J/cm^2. Each image was recorded using a time gate of 1 μs (upper panels) and 5 μs (lower panels), respectively, on the intensifier of the camera. The positions at z = 0 mm defines the front face of the target.

The right panels in the images of fig. 3.16 are the spatial profiles of the plume intensity along the z-direction, obtained by integrating the emission along the x-direction. They help to follow the expansion dynamics of the different components of the plume.

As evidenced by the images, fast photography confirms the OES findings about the presence in the ultrashort laser ablated plume of essentially three different velocity populations. At short delays after the laser pulse (τ<100ns) the intensity profiles allow to clearly distinguish them, being the slowest component still close to the target surface. Then, it is natural to identify these three components with fast ions, atoms/slow ions and nanoparticles, respectively.

Notwithstanding, fast photography allows to point out some differences between the silicon plumes ablated by 0.25ps, 527nm and 0.9ps, 1055nm laser pulses. In particular, the amount of ablated material seem to be higher for the visible than for the infrared radiation, and a direct proof of this behaviour comes directly from the analysis of the fluence dependence of the ablation yields, calculated by integrating the signal of the acquired images over the whole detectable plume emission. The trends, not shown here, demonstrate the total amount of ablated material to be from twice to five times higher in the case of the visible radiation, according to the laser fluence, and becoming up to thirty times higher by considering only the emission from the fast component of the plume (ions and neutrals).

This would suggest the ablation process to be more effective in the visible than in the infrared region of the spectrum, as can be simply explained by looking at the main excitation mechanisms of a semiconductor under ultrashort laser irradiation. Actually, as we already discussed in chapter I, linear and non-linear absorption are the main processes leading to carrier excitation inside a bulk semiconductor, non linear processes becoming more and more effective as the laser intensity increases. In particular, the overall absorption coefficient for single and double absorption can be written as $\eta = \alpha + \beta I(t)$, being α and β the absorption coefficients for linear and double excitation, respectively, and $I(t)$ the laser intensity. For silicon, both α and β at 1055nm are lower than those at 527nm, thus leading to a much stronger absorption for visible than for infrared radiation; the laser light is distributed over a deeper region inside the material at 1055nm so that under the same fluence conditions the energy density in the bulk silicon is lower for infrared radiation. Moreover, the laser intensity during the performed experiments at 527nm was always more than twice that at 1055nm. All these observations could explain the experimental findings about the effectiveness of the ablation process at the two different laser wavelengths employed.

The second interesting feature coming from the silicon plume images is that the fastest component made of high energy ions at 1055nm turns out to be more energetic than the corresponding ablated at 527nm, as is clearly evidenced by fig. 3.16. Indeed, fast ions go rapidly out of the imaged region of space (15mm) after the first 50ns of expansion following infrared irradiation while it is clearly detectable still after 100ns after visible irradiation. This feature cannot be ascribed to the absorption processes described above but should be rather linked to some of the non-equilibrium processes leading to bond weakening and structure destabilization in the few ps after the laser pulse. In particular, *avalanche ionization* seems to be the dominant mechanism for dielectric breakdown in silicon especially at longer wavelengths (provided that the photon energy is greater than the material bandgap), as reported by Pronko et al.[37] Here, the breakdown seems to occur over a very short depth in silicon, about 75nm on average, much less than that for typical one or two photon absorption.[38] This implies that avalanche ionization should create a high amount of electrons in a shallow region under the material surface, thus leading to a very high density of free carriers responsible for the covalent structure destruction and the ejection of fast, high energy ions. Hence, being the process more effective at 1055nm, the velocity patterns derived from fig. 3.16 could be safely explained.

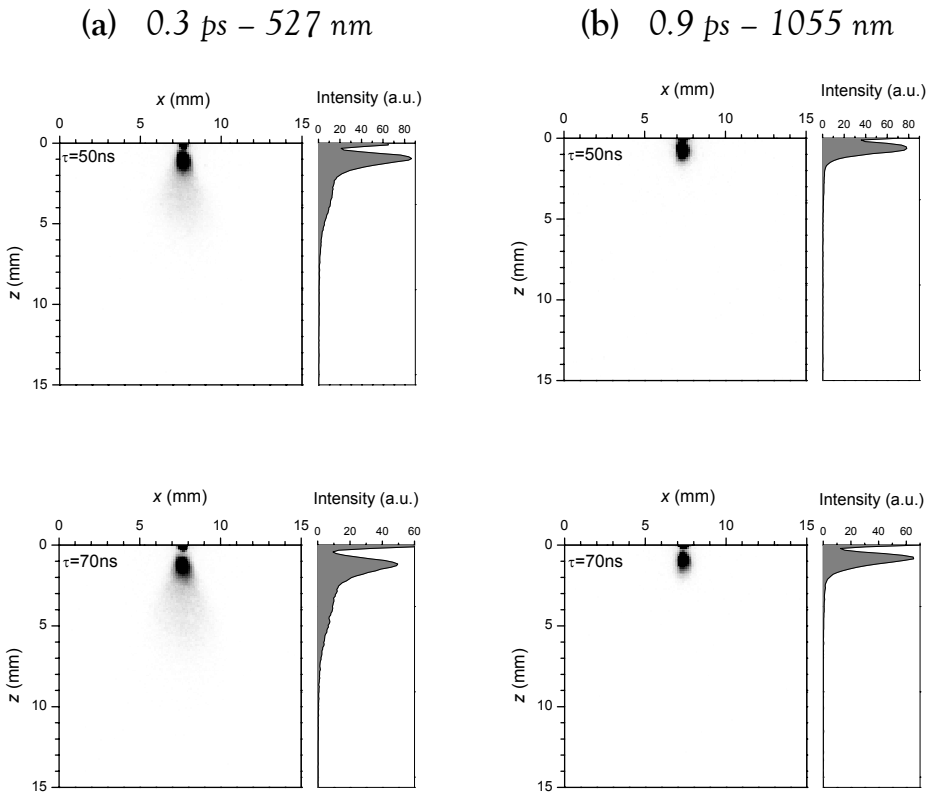

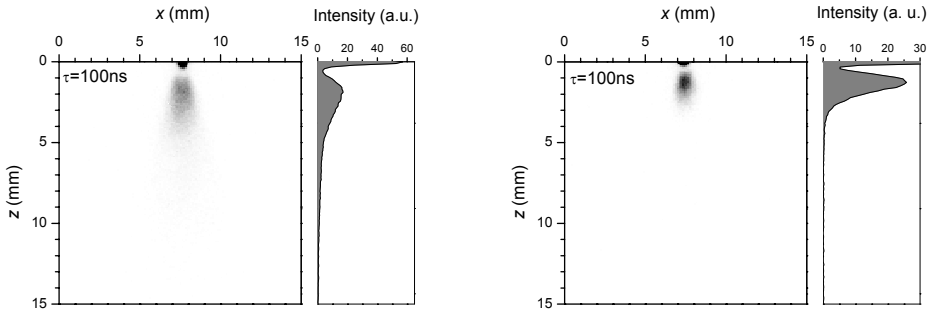

Fig. 3.18: Nickel plume expansion images at different time delays τ: (a) 0.3 ps/527 nm (left hand column), and (b) 0.9 ps/1055 nm (right hand column) laser pulses, at a laser fluence of 0.60 J/cm^2. Each image was recorded using a nominal 10 ns time gate on the intensifier of the camera. The positions at z = 0 mm defines the front face of the target. Each picture is accompanied by the an intensity profile obtained by integrating the image signal along the x direction.

(a) *0.3 ps – 527 nm* **(b)** *0.9 ps – 1055 nm*

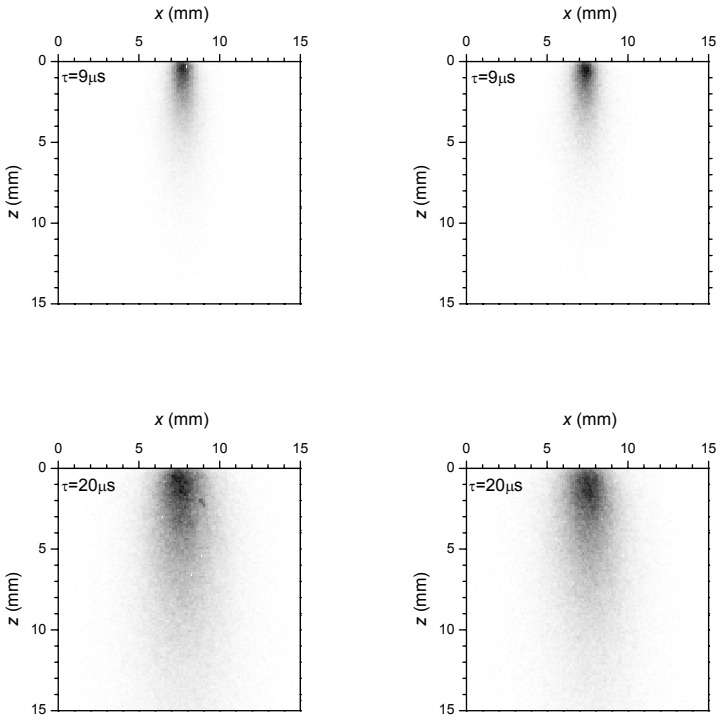

Fig. 3.19: Nickel plume expansion images at different time delays τ: (a) 0.25 ps/527 nm (left hand column), and (b) 0.9 ps/1055 nm (right hand column) laser pulses, at a laser fluence of 0.60 J/cm^2. Each image was recorded using a time gate of 1 μs (upper panels) and 5 μs (lower panels), respectively, on the intensifier of the camera. The positions at z = 0 mm defines the front face of the target.

Figs. 3.18-3.19 report on the nickel time series at both the laser excitations. Here, the three velocity populations are not yet clearly distinguishable as for silicon as a consequence of the greater mass of nickel. In fact, at the investigated distances, the fast ions population looks still more like a tail of the neutral atoms population than a well structured population itself, at both laser wavelengths. Actually, this feature is more dramatic for infrared radiation, where the fast ions population detected by the Langmuir probe at a wavelength of ≈800nm seems to be not present. Indeed, this is probably simply an indirect confirm of the lower efficiency of the material excitation process for metals at infrared wavelengths.

III.3 Atomic Force Microscopy characterization of the nanoparticles phase

To get a deeper understanding of the origin and the morphology of the aggregates produced by ultrashort laser ablation, we performed AFM analysis of deposits of several target materials. The material jet produced during fs laser ablation have been deposited onto mica substrates, at room temperature in high vacuum ($P \approx 10^{-7}$ mbar). The number of laser pulses used for deposition has been carefully selected to obtain deposits of less than one layer and to find the actual size of the free aggregates impinging on the substrate surface. Indeed, the deposition of a large amount of material may lead to particles coagulation up to film growth thus compromising the right investigation of the morphological properties of single clusters.

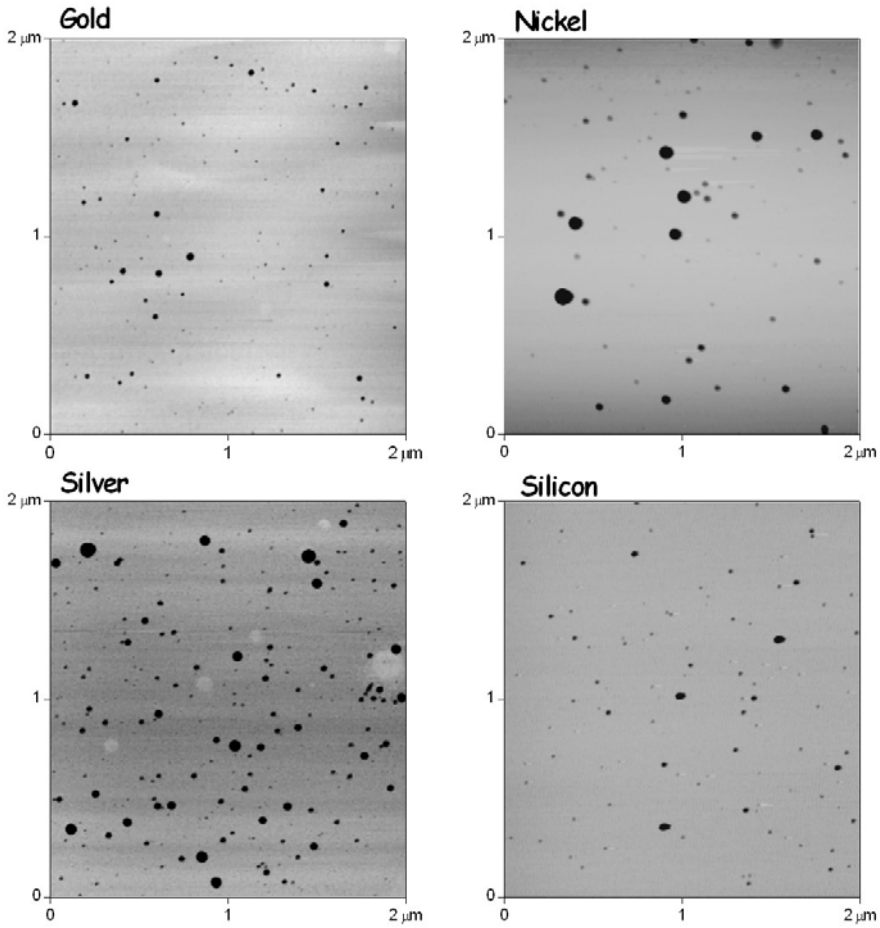

Fig. 3.20: AFM images of a 2μm × 2μm deposited area for four different target materials. Laser fluence ranges from a minimum of 0.3 Jcm^{-2} to a maximum of 1.2 Jcm^{-2}.

Such analysis has been performed for a variety of different targets (Ag, Au, Ni, Si) and at different laser fluences. The sample materials have been selected because of their importance both for basic physics and for technological applications. In fact, both silicon and noble metals constitute case studies in ultrashort laser interaction with materials. Moreover, while silicon is of wide interest in electronics, small-sized catalysts of noble metals (Ag and Au) are attracting increasing interest because of the discovery of their uncommon catalytic activity and specificity.[39,40] On the other hand, systems of fine particles of magnetic materials (Ni, e.g.) are attractive both for their technological applications in permanent magnets and magnetic recording, and for the great scientific interest in developing a better understanding of magnetic phenomena. Actually, the production and characterization of magnetic nanoaggregates have raised a great deal of theoretical and experimental interest since their macroscopic magnetic properties can be controlled through particles size and density tailoring.[41, 42]

Fig. 3.20 shows typical patterns found by AFM analysis of the deposited samples. As readily observed, in spite of the different nature of the selected target materials (noble metals: Ag, Au; transition metals: Ni; semiconductors: Si) all the deposited samples are made of dispersed particles of *sub-micrometric* dimensions, thus definitively confirming the presence in the fs laser ablated plume of a non-atomic component made of aggregates of atoms. Moreover, the AFM analysis underlines that the production of clusters during fs laser ablation is a completely different process with respect to what occurs during ns laser ablation, where *micrometric* aggregates are produced from the melted surface as a consequence of laser irradiation.

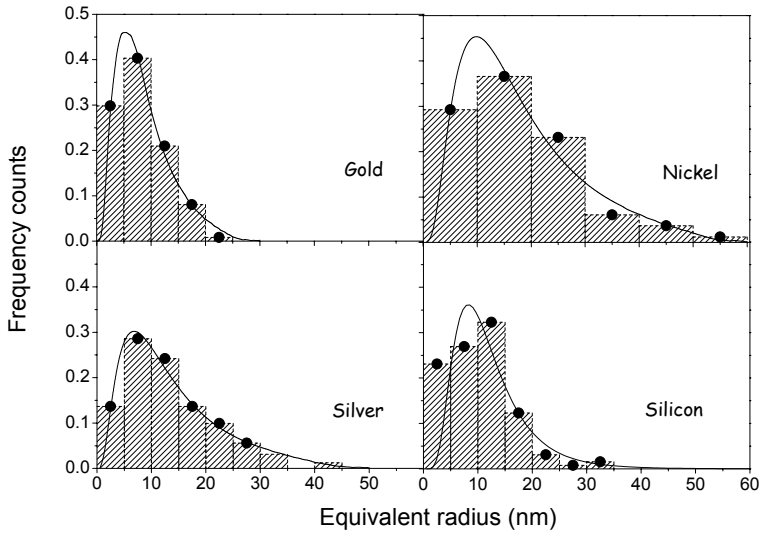

Fig. 3.21: Size distributions of the deposited clusters for the samples shown in Fig. 3.20. The solid lines are a guide for the eye. The bin size for Nickel is twice the others to obtain a significative number of counts in each bin.

The statistical analysis of the deposited samples revealed the nanometric character of the clusters, thus confirming the rough indications coming from the OES studies. A specific image analysis software, in fact, allowed us to obtain from AFM images the size distributions of the deposited aggregates and several related statistical parameters, as shown in Fig. 3.21 in the case of the images of Fig. 3.20. As readily observed, the sizes are well distributed over a not so large interval around the average radius value which is always about 10-15 nanometres, thus leading to peaked, narrow size distributions with lognormal-like aspect.

Hence, by investigating the morphology of the deposited samples, AFM allowed the characterization of the nanoparticles phase as well as of their production mechanisms by studying, in particular, the dependence of the process upon specific laser parameters[43,44]. For instance, Table III.2 well summarizes the results obtained by irradiating several target materials

at three different fluences while Table III.3(a)-(b) compare the effectiveness of the process at three different wavelengths and pulse durations in the ultrashort regime ($\tau \lesssim 1$ps) for silicon and nickel, respectively.

Table III.2: Statistical parameters of the size distributions obtained by 0.1ps, 780nm pulses for four different materials as a function of the laser fluence *F*. Here r_m is the nanoparticles mean radius, σ is the standard deviation of the distribution, r_{max} is the maximum radius defined as the value below which 90% of the particles is counted, α is the size distribution dispersion (i.e. $\alpha = \sigma / r_m$).

	F (Jcm^{-2})	r_m (nm)	σ (nm)	r_{max} (nm)	α
Au	0.3	8.0	4.7	27	0.59
Au	0.6	16.4	10.0	48	0.61
Au	1.2	14.1	10.9	55	0.77
Ag	0.3	11.8	8.5	46	0.72
Ag	0.6	13.4	8.0	45	0.60
Ag	1.2	15.1	11.6	52	0.77
Ni	0.3	19.7	13.8	60	0.70
Ni	0.6	17.4	11.0	55	0.63
Ni	1.2	24.7	19.4	100	0.78
Si	0.3	7.9	9.3	13	0.75
Si	0.6	11.6	12.6	15	0.59
Si	1.2	9.5	12.1	15	0.55

The experimental data suggest a weak dependence of the size distributions upon material and laser properties. Actually, all the statistical parameters taken into account turn out to be quite material insensitive (see Tab. III.1), even if nickel distributions are quite wider than the others and shifted to higher values of radii, while for silicon both the mean radii and the maximum radii are the lowest measured values at each fluence. Moreover, a little increase of the statistical parameters as a function of the laser fluence could be noticed for all the investigated materials. Similarly, from Table III.3, no peculiar trends upon laser pulse wavelength and duration appear, both for silicon and nickel. The independence of the process on pulse duration could be easily understood by noticing that the characteristic relaxation times between the electrons and the lattice are at least one order of magnitude greater than all the laser durations employed in the experiments (see chapter I); then, the electron bath heating by the laser irradiation and the subsequent energy exchange to the lattice are processes completely separated in time, thus ensuring the establishment of almost the same laser-matter interaction

regime. These features justify the classification "ultrashort" for the laser durations used in the present experiments to indicate their belonging to the same laser-matter interaction regime; if the laser pulses last for times shorter than the typical electron to lattice relaxation time, then the ablation regime and the whole complex phenomena generated by the light irradiation are practically the same.

Table III.3: Statistical parameters characterizing the size distributions of silicon (a) and nickel (b) nanoparticles produced with the three laser sources used in the present work, at three different values of the laser fluence *F*. The symbols are as in Table III.2.

(a)

Laser τ_L – λ	F_L (Jcm^{-2})	r_m (nm)	σ (nm)	r_{max} (nm)	α
0.9 ps - 1055 nm	0.3	5.2	4.3	8.7	0.83
	0.45	8.6	6.7	15.0	0.78
	0.6	12.2	5.3	18.4	0.43
0.3 ps - 527 nm	0.3	11.5	8.5	20.5	0.74
	0.6	14.5	10.7	25.0	0.74
	1.1	41.7	29.9	65.0	0.72
0.1 ps - 780 nm	0.3	7.9	5.1	13	0.75
	0.6	11.6	8.6	15	0.59
	1.1	9.5	5.5	15	0.55

(b)

Laser τ_L – λ	F_L (J/cm^2)	r_m (nm)	σ (nm)	r_{max} (nm)	α
0.9 ps - 1055 nm	0.3	20.8	14.2	55	0.68
	0.6	28.0	17.9	45	0.64
	0.8	27.5	18.0	53	0.65
0.3 ps - 527 nm	0.4	18.1	10.9	28.0	0.60
	0.8	17.4	9.1	27.5	0.52
	1.1	19.5	9.7	30.0	0.50
0.1 ps - 780 nm	0.3	19.7	13.8	60	0.70
	0.6	17.4	11.0	55	0.63
	1.2	24.7	19.4	100	0.78

All these results suggest ultrashort pulsed laser ablation as a powerful and versatile technique to produce nanoparticles of limited sizes and size dispersion from practically any target material. Moreover, it has a lot of advantages with respect to the more established techniques to produce nanoparticles. For instance, as already explained before, in contrast with nanosecond laser ablation it does not need the presence in the vacuum chamber of a

background gas to let the atoms in the plume condensing to yield nanoparticles, since it is worked in high vacuum; this allows avoiding to find the optimal gas pressure conditions and to take into account complex plume hydrodynamics and in flight chemical kinetics. Furthermore, the deposition of dispersed nanoparticles by ultrashort PLA is a rather instantaneous process and doesn't imply long deposition times; neither does it need to make use of chemical reagents and reactions which are specific for the material to deposit, as in the case of chemical and electrochemical deposition techniques.

Nanoparticles are thus produced in a rather easy and controllable way without specific settings related to the ablated material; the possibility to control their sizes and size dispersion is currently under study and would make ultrashort pulsed laser ablation one the most effective techniques to produce nanoparticles from any solid material.

References

[1] S. K. Sundaram and E. Mazur, Nature Materials 1, 217 (2002).

[2] B. N. Chichkov, C. Momma, S. Nolte, F. von Alvensleben and A. Tünnermann, Appl. Phys. A 63, 109 (1996).

[3] H. E. Elsayed-Ali, T. B. Norris, M. A. Pessot and G. A. Mourou, Phys Rev. Lett. 58, 1212 (1987).

[4] M. Bonn, D. N. Denzler, S. Funk, M. Wolf, S. S. Wellershoff and J. Hohlfeld, Phys. Rev. B 61, 1101 (2000).

[5] S.-S. Wellershoff, J. Hohlfeld, J. Güdde and E. Matthias, Appl. Phys A 69, S99 (1999).

[6] C. Guo, G. Rodriguez, A. Lobad, and A. J. Taylor, Phys. Rev. Lett. 84, 4493 (2000).

[7] C. Guo and A. J. Taylor, Phys. Rev. B 62, 5382 (2000).

[8] S. Amoruso, R. Bruzzese, N. Spinelli, R. Velotta, J. Phys. B 32, R131 (1999).

[9] S. Amoruso, R. Bruzzese, N. Spinelli, R. Velotta, X. Wang, and C. Ferdeghini, Appl. Phys. Lett. 80, 4315 (2002).

[10] J. Costa, P. Roura, G. Sardin, J. R. Morante and E. Bertran, Appl. Phys. Lett. 64, 463 (1994).

[11] J. Costa, P. Roura, J. R. Morante and E. Bertran, J. Appl. Phys. 83, 7879 (1998).

[12] P. Heszler, L. Landström, M. Lindstam, J.-O. Carlsson, J. Appl. Phys. **89**, 3967 (2001).

[13] O. Albert, S. Roger, Y. Glinec, J.C. Loulergue, J. Etchepare, C. Boulmer-Leborgne, J. Perriere and E. Millon, Appl. Phys. A 76, 319 (2003).

[14] D. B. Chrisey and G.K. Hubler (Eds.), *Pulsed Laser Deposition of Thin Films* (John Wiley & Sons, New York, 1994).

[15] J. F. Ready, "Effects of high power laser radiation", Academic Press London 1971.

[16] V. M. Smirnov, Physics –Uspekhi **37,** 621 (1994).

[17] M. Brandbyge, Mads R. Sorensen and Karsten W. Jacobsen, Phys. Rev. B **56,** 14956 (1997).

[18] S. Amoruso, C. Altucci, R. Bruzzese, C. de Lisio, N. Spinelli, R. Velotta, M. Vitiello, and X. Wang, *Appl. Phys. A* 79, 1377 (2004).

[19] Mengqi Ye, Costas P. Grigoropoulos, J. Appl. Phys. 89, 5183 (2001).

[20] S. Amoruso, M. Armenante, V. Berardi, R. Bruzzese, N. Spinelli, Appl. Phys. A 65, 265 (1997).

[21] S. Amoruso, X. Wang, C. Altucci, C. de Lisio, M. Armenante, R. Bruzzese and R. Velotta, Appl. Phys. Lett. 77, 3728 (2000).

[22] T. E. Glover, J. Opt. Soc. Am. B 20, 125 (2003).

[23] S. I. Anisimov, D. Bäuerle and B. S. Luk'yanchuk, *Phys. Rev. B*, **48** (1993) 12076.

[24] M. W. Stapleton and J. P. Mosnier, *Appl. Surf. Sci.*, **197-198** (2002) 72.

[25] P. Heszler, K. Elim, M. Boman and J.-O. Carlsson, *Appl. Phys. A*, **70** (2000) 613.

[26] B. M. Smirnov and H. Weidele, *JEPT Lett.*, **69** (1999) 490.

[27] S. Nolte, C. Momma, H. Jacobs, A. Tünnermann, B. N. Chichkov, B. Wellegehausen, and H. Welling, J. Opt. Soc. Am. B 14, 2716 (1997).

[28] B.N. Chichkov, C. Momma, S. Nolte, F. von Alvensleben, and A. Tünnermann, Appl. Phys. A 63, 109 (1996).

[29] A. Rousse, C. Rischel, S. Fourmaux, I. Uschmann, S. Sebban, G. Grillon, Ph. Balcou, E. Förster, J.P. Geindre, P. Audebert, J.C. Gauthier and D. Hulin, Nature 410, 65 (2001).

[30] K. Sokolowki-Tinten, J. Bialkowski, M. Boing, A. Cavalleri, and D. von der Linde, Phys. Rev. B 58, R11805 (1998).

[31] A. Cavalleri, K. Sokolowki-Tinten, J. Bialkowski, M. Schreiner, and D. von der Linde, J. Appl. Phys. 85, 3301 (1999).

[32] J. K. Chen and J.E. Beraun, J. Opt. A: Pure Appl. Opt 5, 168 (2003).

[33] D. Perez and L. J. Lewis, Phys. Rev. Lett. 89, 255504-1 (2002); and Phys. Rev. B 67, 184102 (2003).

[34] S. I. Kudryashov and V. I. Emel'yanov, JETP Letters 73, 666 (2001).

[35] A.V. Bulgakov, I. Ozerov, W. Marine, Th. Sol. Films 453-454, 557 (2004).

[36] W. G. Roeterdink, L. B. F. Juurlink, O. P. H. Vaughan, J. Dura Diez, M. Bonn, and A. W. Kleyn, Appl. Phys. Lett. 82, 4190 (2003).

[37] P. P. Pronko, P. A. VanRompay, C. Horvath, F. Loesel, T. Juhasz, X. Liu, and G. Mourou, Phys. Rev. B 58, 2387 (1998).

[38] P. P. Pronko, P. A. VanRompay, R. K. Singh, F. Qian, D. Du, and X. Liu, in *Advanced Laser Processing of Materials-Fundamentals and Applications*, edited by R. K. Singh, MRS Symposia Proceedings No. 397 (Materials Research Society, Pittsburgh, 1996), p. 45.

[39] M. Haruta, Catal. Today **36**, 153 (1997).

[40] M. Valden, X. Lai, and D. W. Goodman, Science **281**, 1647 (1998).

[41] X. Batlle and A. Labarta, J. Phys. D **35**, R15 (2002).

[42] A. A. Novakova, V. Y. Lanchiniskaya, A. Volkov, T. S. Gendler, T. Y. Kiseleva, M. A. Moekvina, and S. B. Zezin, J. Magn. Magn. Mater. **258**, 354 (2003).

[43] S. Amoruso, G. Ausanio, R. Bruzzese, M. Vitiello, and X. Wang, Phys. Rev. B 71, 033406 (2005).

[44] S Amoruso, G Ausanio, A C Barone, R Bruzzese, L Gragnaniello, M Vitiello and X. Wang, J. Phys. B: At. Mol.Opt. Phys. 38, L329 (2005).

CHAPTER IV

Numerical modelling and discussion

As depicted by the Two Temperature Model (TTM), the spatial energy distribution built up inside the target by the laser irradiation and subsequent *e-ph* thermalization decreases exponentially with depth. Thus, atomic layers placed at different depths below the surface are characterized by different absorbed energy densities and, hence, by different temperature histories. These processes, then, allow for the simultaneous appearance of different species in the ultrashort laser generated plume, going from atoms and ions formed through vaporization to nanodroplets formed through homogeneous nucleation (phase explosion), fragmentation and, eventually, spallation, as a consequence of the different thermodynamic relaxation pathways followed by the various layers placed at different depths below the surface.

In chapter I we reported on a general overview of the whole set of complex processes which may affect a target material when irradiated by ultrashort laser pulses, by means of Molecular Dynamics simulations of a two-dimensional Lennard-Jones fluid.[1] Indeed, these simulations are very powerful to investigate all the possible relaxation channels that the ablated material can experience but cannot help to single out the actual mechanisms which are responsible for nanoparticles formation; on the other hand, no experimental investigations were performed up to now which are capable to completely validate the theoretical findings, and vice versa.

In ref. 2 experimental evidence of efficient nanoparticles production for an intermediate laser intensity interval ($3x10^{12}$ - $5x10^{14}$ W/cm^2) was reported. For such intensities, the adiabatic relaxation paths of the expanding material after laser irradiation (see Fig. 1.4, chapter I) all enter the metastable thermodynamic region at supercritical or near-critical densities, but no experimental findings could help the authors to select among phase explosion, fragmentation or spinodal decomposition processes.

Thus, we performed Molecular Dynamics simulations in collaboration with the group of Prof. Petar Atanasov of the Institute of Electronics of the Bulgarian Academy of Sciences and the main results of the comparison between our numerical and experimental investigations will be reported in section IV.1[3]. The technique allows to follow the dynamics of each particle in the sample by taking into account the forces acting on it, thus returning a reliable description of the system evolution.

As it is clear from the discussion reported in chapter I, an estimation as accurate as possible of the final temperature reached by the sample at the end of the laser irradiation is of great importance since it completely determines the subsequent relaxation paths during adiabatic expansion. Thus, I employed Monte Carlo numerical techniques to get information about the spatial distribution of the temperature in the target material after the laser irradiation, and the main results of this studies are briefly discussed in section IV.2.

IV.1 Molecular Dynamics simulations

We simulated by Molecular Dynamics (MD) technique the laser ablation process from a solid aluminum target irradiated in vacuum by laser pulses of duration τ_p=0.1 ps full width at half-maximum (FWHM), and a wavelength of λ =800 nm. The laser-beam intensity was considered to have Gaussian temporal shape and an uniform spatial distribution.

The numerical model is based on the classical MD simulation technique, where the velocity Verlet algorithm was applied to integrate the equation of motion.[4] The modelled material was simulated by a number of unit face-centred-cubic (fcc) cells in the *x*, *y*, and *z* directions, respectively, *z* being the direction of the normal to the sample surface, and the total amount of simulated atoms in the computational domain was $4x10^4$.

The interaction between the atoms of the system was governed by the Morse potential and its particular parameters for Al were taken from ref. 5. In order to avoid the interaction between atoms at distances longer than the potential cutoff radius, the calculations were carried out using the cell structure and the link-list method. Moreover, periodic boundary conditions for the atoms were applied in the *x* and *y* directions of the computational domain in order to simulate an infinite medium. This means that processes occurring in the center of the laser spot were examined, while the effect of the laser spot edges was neglected.

The initial velocities were randomly ascribed to the atoms according to the Maxwell-Boltzmann distribution at room temperature. A velocity and pressure dampening technique[6] was applied at the bottom of the computational cell in order to prevent artificial ablation effects that might be caused by the shock-wave reflection from the bottom boundary of the system.

At any given laser energy, the corresponding absorbed photons are deposited in the material according to the Lambert-Beer law and to the optical parameters of the material at the laser wavelength used (reflectivity *R* = 85%; absorption coefficient α =1.25 x 10^6 cm^{-1}).

The energy of the photons was transferred to the atoms of the system within a characteristic time τ_{eq}, which corresponds to the time of electron-lattice energy transfer and the establishment of the equilibrium temperature. τ_{eq} depends on the properties of the material and, according to the two-temperature diffusion model[11], we estimated it to be 5.3 ps for Al. The electron thermal diffusion was taken into account by an increase of the effective penetration depth of the laser energy; an estimation is given again by the TTM as $l_{th}^{e} \approx (D_e \tau_{eq})^{1/2}$, where $D_e = K_e / C_e$ is the electron diffusion coefficient. The temperature dependences of the electron thermal conductivity K_e and of the electron heat capacity C_e were taken from Refs. 7 and 8.

Finally, the evolution of the ablation process was investigated up to a hundred picosecond after the laser pulse arrival time.

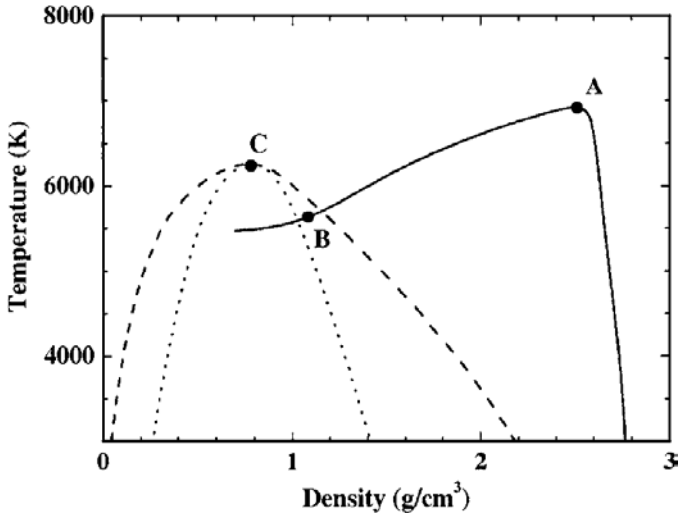

Fig. 4.1: Temperature to density phase diagram for aluminum. The dashed and the dotted lines are the binodal and the spinodal curves, respectively. The full line is the thermodynamic path followed by the ablated material at a fluence of 0.4 J/cm^2. See the text for further details.

Fig. 4.1 shows the phase diagram for aluminum in a temperature - density frame.[9,10] The solid line represents the relaxation path of the ablated material during the first ≈10 ps after the laser pulse irradiation at a fluence of 0.4 J/cm^2. During about the first 5 ps, as a consequence of the electron to lattice energy exchange occurring on a timescale of τ_{eq}, the material is heated at a nearly constant density up to a maximum lattice temperature of ≈7000 K (point A in Fig.4.1), which is higher than the critical one (C). Then, a fast adiabatic relaxation goes on towards the metastable region of the phase diagram and the point B in Fig. 4.1 is reached within the next 2 ps (i.e. after 7 ps from the laser pulse). At this point, simultaneous nucleation of the gas phase in different areas of the material takes place, and nanoparticles of the expanding material can be formed.

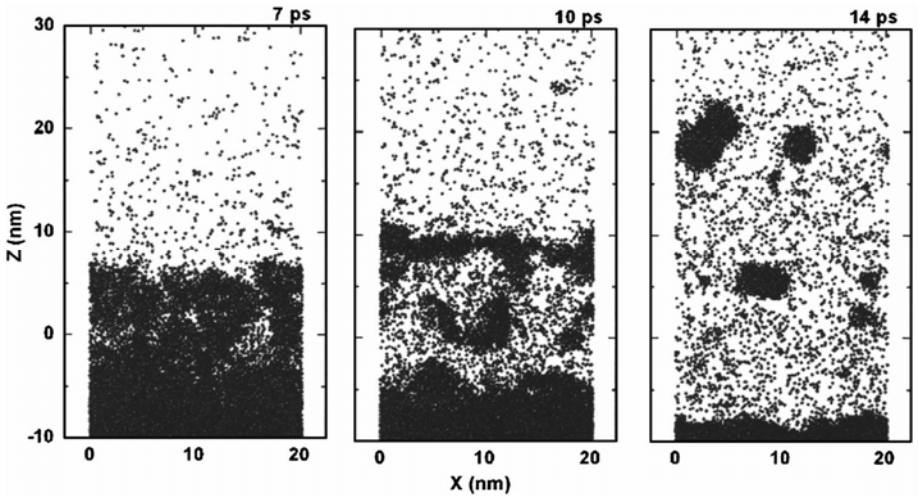

Fig. 4.2: Snapshots of the initial stage of expansion for an aluminum ablated target at a laser fluence of 0.4 J/cm^2.

This could be directly observed in Fig. 4.2, where the irradiated surface material develops a nanocluster character in the first 10ps of expansion, thus becoming a mixture of liquid and gas bubbles as typically observed as a consequence of phase explosion processes. The snapshots at later expansion stages reveal the absence of further mechanisms leading to nanoparticle formation (as for instance condensation processes), thus ensuring that at the laser fluences of concern here nanoparticles are formed exclusively as a consequence of mechanisms acting directly on the target, as explosive phase decomposition in the very early stages of material expansion[3].

We tried also to compare the MD simulations with the experimental results obtained by irradiating an aluminum target with 100fs, 800nm Ti:sapphire pulses. In particular, we estimated by time-gated optical emission spectroscopy the fluence dependence of the ablation yield; the comparison with the simulated ablation depth is shown in Fig. 4.3 and clearly underlines the agreement between the simulation and the experiment.

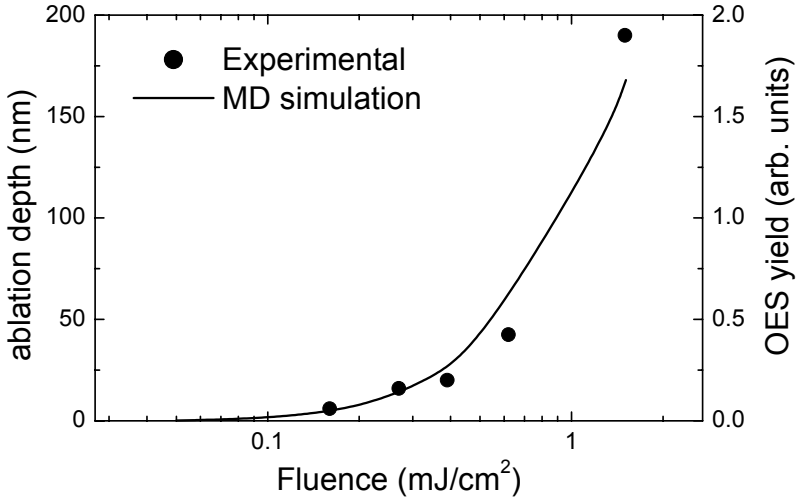

Fig. 4.3: Comparison between the fluence dependence of the calculated ablation depth (line) and the experimental optical emission yield (dots), for 100fs irradiation at a wavelength of 800nm.

Thus, MD simulations turned out to be a valid instrument to study the processes occurring during ultrashort pulsed laser ablation in vacuum and to get a theoretical explanation of our experimental results. In particular, it is capable to finely reproduce the presence in the plume of nanoparticles of limited sizes (≈10nm) thus confirming it as a prominent and very specific feature of ultrashort pulsed laser ablation. Moreover, the laser ablated plume turned out to be made of atomic species as well as of nanoparticles, which come directly from the target as a consequence of phase explosion mechanisms and not as the result of in-flight condensation processes. Hence, phase explosion turn out to be responsible for nanoparticles ejection in the fluence range of concern here, even if the occurrence of other processes, like fragmentation, spallation and so on, cannot be completely disregarded.

Actually, as already observed in chapter I, atomic layers placed at various depths inside the material are heated to different temperatures by the laser irradiation according to the spatial distribution of the deposited energy in the bulk target. Thus, the mechanisms previously cited can simultaneously contribute to the plume formation and, in particular, to nanoparticles ejection. That is why an estimation of the spatial energy distribution inside a bulk material after ultrashort irradiation is of great present interest since can help to study the influence of the different mechanisms onto the plume morphology, as we are going to explain in the next section.

IV.2 Heating and relaxation of metals under ultrashort laser irradiation

In chapter I we discussed the main processes occurring in a solid target when irradiated by ultrashort laser pulses, separately for metals and semiconductors. In both cases, the mechanisms of absorption and transport of the delivered energy inside the bulk material can be described by means of the Two Temperature Model (TTM), a system of two coupled equations for the electron and the lattice temperatures which cannot be solved analytically. Thus, according to the specific approximations used to solve the TTM equations, only an incomplete description of the complex processes set in by the laser irradiation can be achieved.

In particular we reported the details of the model proposed by Nolte et al.[11], where the spatial distribution of the electron and lattice temperatures inside the material was calculated through the TTM system by neglecting at first the electron thermal diffusion, which is then reintroduced phenomenologically to yield the final behaviour of eq. (1.3). Along this way, they succeed to well reproduce the logarithmic dependence of the ablation depth upon laser fluence and, in particular, to predict two different material excitation regimes where the absorption of the laser light is governed by the optical penetration depth α^{-1} and by the electron thermal penetration depth l_{th}, respectively, as we already reported in section III.2C in chapter III.

Actually, an estimation as accurate as possible of the energy spatial distribution inside the bulk material, as a consequence of both light absorption into the skin depth and electron thermal diffusion, is of great present interest since it determines the features of the subsequent material relaxation and expansion. However, while one-photon absorption is ruled by the well known Lambert-Beer (LB) law, there is no general law which is able to describe electron thermal diffusion along a region of depth l_{th}. The behaviour predicted by eq. (1.3) is not a general law as well, since electron thermal diffusion is taken into account only phenomenologically.

Hence, in the next subsection (IV.2.1) the main results of a Monte Carlo (MC) simulation devised to describe the process of material excitation due to both one-photon absorption and electron thermal diffusion, is reported.

Once the spatial energy distribution in the bulk material after the laser irradiation has been estimated, thermodynamics allows to follow the subsequent relaxation of the system by modelling the plume expansion as an adiabatic behaviour, as already depicted in chapter I. Thermodynamic pathways have been frequently used to describe the material relaxation at the end of ultrashort laser pulses.[1,2,10,12] Nonetheless, only MD simulations[1] or hydrodynamic

codes[10] allow a precise study of the relaxation of selected areas of the plume (and, thus, of the target material), while all the approximate descriptions based on a particular solution of the TTM equations yield only a rough and qualitative estimation of what is going on.[2,12] Thus the Monte Carlo results of subsection IV.2.1 about the spatial energy distribution after the laser irradiation can be nicely coupled with the thermodynamic description of the subsequent material relaxation to precisely follow the evolution of selected areas of the target and predict the occurrence of specific ablation mechanisms. The results of these studies will be shown in subsection IV.2.2.

IV.2.1 Spatial energy distribution in metals: a Monte Carlo approach

In this section a Monte Carlo technique is employed to estimate the spatial energy distribution inside a metal target after ultrashort laser irradiation, as a consequence of both one-photon absorption and electron thermal diffusion mechanisms.

The simulated sample was a number of unit face centered cubic (fcc) cells of nickel, thus giving a slab of ≈ 2nm x 2nm x 250nm (= 6 x 6 x 700 unit cells in the x, y and z directions, respectively, z representing the direction along the normal to the target surface; a=0.352nm is the lattice parameter for nickel), corresponding to ≈ 2 x 10^5 atoms. The laser energy, corresponding to a wavelength of 527nm (photon energy of ≈2.3 eV), was randomly delivered to the atoms in the sample through one-photon absorption according to the LB distribution, which is in its turn randomly generated by calculating the quantity $\xi = \Lambda \, \mathrm{Log}[\chi]$, where χ is a random number in the interval [0,1] and $\Lambda=\alpha^{-1}$ is the optical penetration depth[13]; by extracting N_{ph} values of χ, the corresponding ξ values are distributed according to the LB law, being N_{ph} the number of photons corresponding to the delivered energy. Absorption has been considered instantaneous, that is no coupling between the energy redistribution and the laser light has been considered, thus reproducing the phenomenology of the laser irradiation by ultrashort pulses. The optical parameters for nickel used in the simulation are taken from ref. 14.

If no electron thermal diffusion takes place after photons absorption, the LB distribution should well reproduce the final spatial energy distribution inside the bulk material.[15] Indeed, electron diffusion inside the bulk material works and is affected by both electron-electron and electron-phonon scattering, the electron relaxation time τ being thus determined by the electron-electron and electron-phonon collision frequencies, $1/\tau = 1/\tau_{e,e} + 1/\tau_{e,ph}$.[16] In case of strong overheating of the electron subsystem, as is the case of ultrashort laser ablation, the

frequencies $1/\tau_{e,e}$ and $1/\tau_{e,ph}$ become equal at the characteristic electron temperature $T_e = T^* \approx (\varepsilon_F T_l / k_B)^{1/2}$, where T_l is the lattice temperature, ε_F the Fermi energy and k_B the Boltzmann constant. For nickel $T^* \approx$ 5300K, being $\varepsilon_F \approx$8.5 eV [17] and by taking a lattice temperature value of $T_l \approx$300K, and consequently two distinct diffusion regimes are determined:

- For $T_e \geq T^*$, the electron-electron collisions determine the heat transport, and the collision frequency is given by $1/\tau \approx 1/\tau_{e,e} \approx (k_B T_e)^2 / h\varepsilon_F$
- For $T_e \leq T^*$, the electron-phonon collisions determine the heat transport, and the collision frequency is given by $1/\tau \approx 1/\tau_{e,ph} \approx k_B T_l / h$

being h the Planck's constant. As a consequence, for temperatures lower than the Fermi temperature (which is the case for the fluences of concern here), we can distinguish two regimes for the time dependence of the electron heat penetration depth:

$$l_{th} \approx \frac{v_F \sqrt{h\varepsilon_F t}}{k_B T_e} \qquad for \quad T_e \geq T^*$$

$$l_{th} \approx \sqrt{\frac{2t}{A_e T_l}} \qquad for \quad T_e \leq T^* \qquad (4.1)$$

where v_F is the Fermi velocity and A_e the electron thermal conductivity. Typical values for l_{th} are about 5-10 nm in the low temperature regime, and about 60-70 nm in the high temperature regime. Thus, a greater electron diffusion and, consequently, a more efficient material removal has to be expected at higher fluences. Actually, it is worth noticing that both diffusion regimes could be simultaneously effective at the fluences of concern here since atomic layers at different depths inside the bulk material are characterized by different energies; thus, the double regime in the fluence dependence of the ablation depth could be explained in terms of the interplay between the two diffusion regimes.

To verify this hypothesis, we simulate electron thermal diffusion by randomly redistributing the energy delivered according to the LB law, by taking into account eq. (4.1). The simulation time is divided in time steps of $\Delta t = 10^{-13}$ *s* (which is the time interval over which l_{th} is computed from eq. (4.1)); a small amount (<10%) of the photon energy is subtracted from an atom placed

at the (i_{th}, j_{th}, z_{th}) site and is randomly redistributed according to an uniform probability distribution along the i and j directions, and to a diffusion like law along the z direction, $\Delta z \propto exp(-z/l_{th})$, which is randomly generated by using the suitable value of l_{th} according to the energy possessed by the atom; the temperature T_e is computed from the energy of the atom and by comparing it with T^* the right diffusion regime can be taken into account through eq (4.1). The procedure is repeated for each atom in the simulated sample and for subsequent time steps up to when all the initial delivered energy has been redistributed. Backward electron diffusion is also taken into account by allowing energy redistribution in either the positive and the negative z directions with respect to each atom; moreover, periodic boundary conditions has been imposed at the walls of the simulated sample. Fig. 4.4 shows the energy distribution inside the nickel slab before and after electron thermal diffusion.

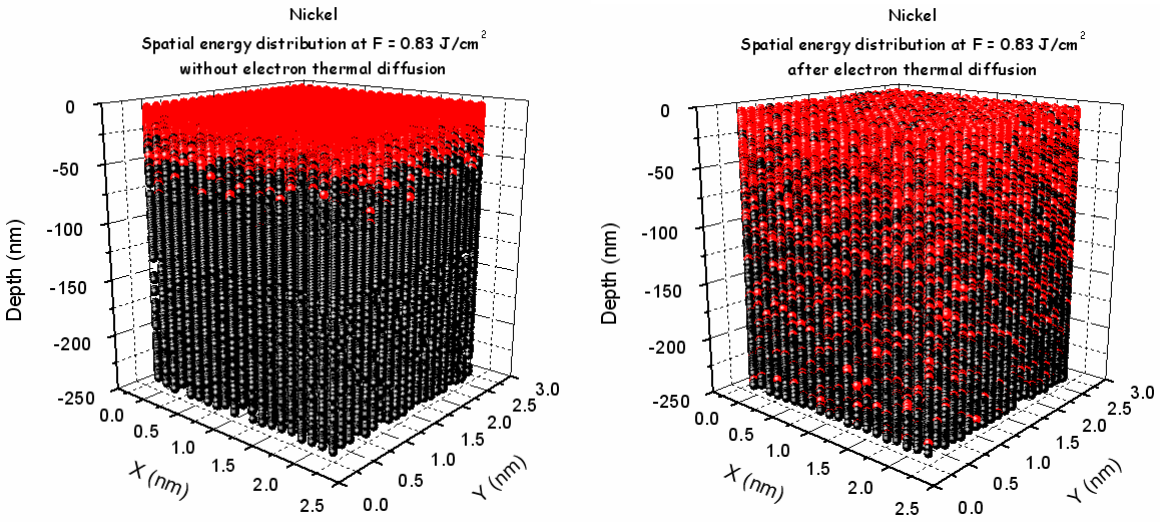

Fig. 4.4: Spatial energy distribution inside the bulk material according to the LB law (left) and after electron thermal diffusion (right), at a laser fluence of 0.8 J/cm^2. The black dots represent unaffected atoms, while the red dots are excited atoms. The unities along the x and y direction have been taken different from that along the z direction for the sake of clarity.

The red dots represent excited atoms, while the black dots are unaffected atoms. Actually, atoms at different depths possess distinct energies, since, on average, the deeper is the atom the lower is its energy. Fig. 4.5 well reproduce this behaviour, showing the average spatial distribution per layer of the normalized temperature inside the material after electron thermal diffusion, at a fluence of F=0.8 J/cm^2, obtained by averaging over the energies inside each layer; also a comparison with the initial LB energy distribution is reported. The distribution

determined by electron thermal diffusion is fitted according to the phenomenological behaviour predicted by Nolte et al.[11] (and already reported by eq. (1.3) in chapter I)

$$\varepsilon(z) \propto \frac{1}{\alpha}\exp\left(-\frac{z}{\alpha}\right)+\frac{1}{l_{th}}\exp\left(-\frac{z}{l_{th}}\right) \tag{4.2}$$

by considering α and l_{th} as fitting parameters. The estimated values are ≈11nm for $\Lambda=\alpha^{-1}$ (a value very close to that reported in the literature of ≈8nm) and $l_{th} \approx 63$ nm.

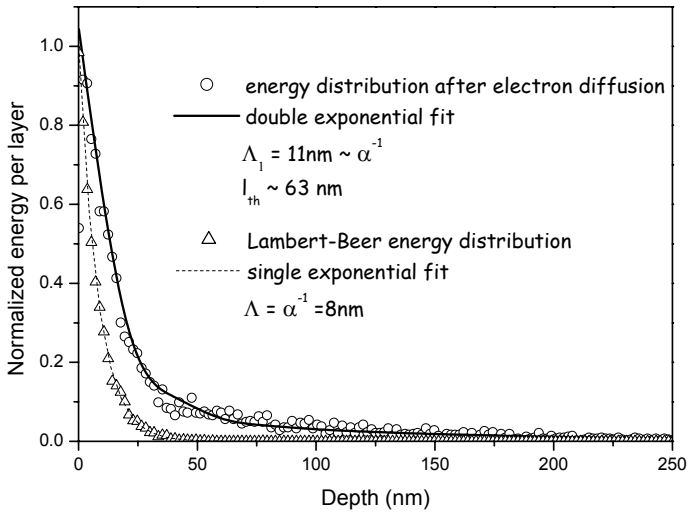

Fig. 4.5: Average spatial energy distribution per layer inside the bulk material before and after electron thermal diffusion at a laser fluence of F=0.8 J/cm^2. The corresponding energy penetration depths are estimated. See the text for further details.

As we discussed above, at the laser fluences of concern here, essentially two different diffusion regimes take place inside the bulk material. Indeed, from eq. (4.1) clearly turns out that while in the low temperature regime the electron thermal diffusion is constant (and equal to ≈ 6 nm), at higher temperatures l_{th} depends on the electron temperature T_e and thus, in our simulation, to the energy delivered to the atoms according to the LB law. Therefore, it can assume different values, ranging about from 40 nm to 100 nm at the higher fluences considered here, as shown in Fig. 4.6 where the distribution of the l_{th} values taken by the atoms for a laser fluence of F = 0.8 J/cm^2 is reported. As readily seen from the picture, the value for the electron thermal diffusion estimated by the fit according to eq. (4.2) (≈63nm) is very close to the mean value of the simulated distribution for l_{th} in the high diffusion regime (≈67nm). Thus, even if it

is not capable to describe the actual energy distribution inside each atomic layer, we can state that eq. (4.2) is a reliable representation of the average temperature spatial distribution inside a material after ultrashort laser irradiation, as a consequence of both one-photon absorption and electron thermal diffusion processes.

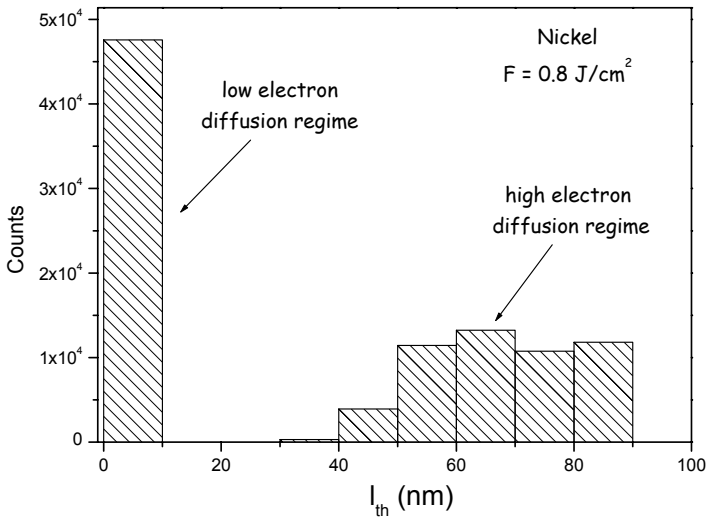

Fig. 4.6: Distribution of the values of l_{th} calculated at a laser fluence of F = 0.8 J/cm^2. The two diffusion regimes can be clearly distinguished.

Nonetheless, the MC simulation is able to provide also information about the energy content of each atom, thus giving a more precise description of the laser excitation process.

To verify the validity of the model we estimated the ablation yield for atoms and compared it with the fluence dependence of the emission yield as obtained by fast photography measurements. To do this, we can assume that only atoms whose energy exceeds the cohesion energy will undergo vaporization (actually a little bit more energy should be needed[18]). The corresponding temperature threshold is approximately given by the vaporization point, equal to 3187 K for nickel. By calculating in this fashion the number of ablated atoms at different laser energies, the fluence dependence of the ablation yield can be simulated, thus giving the behaviour reported in Fig. 4.7.

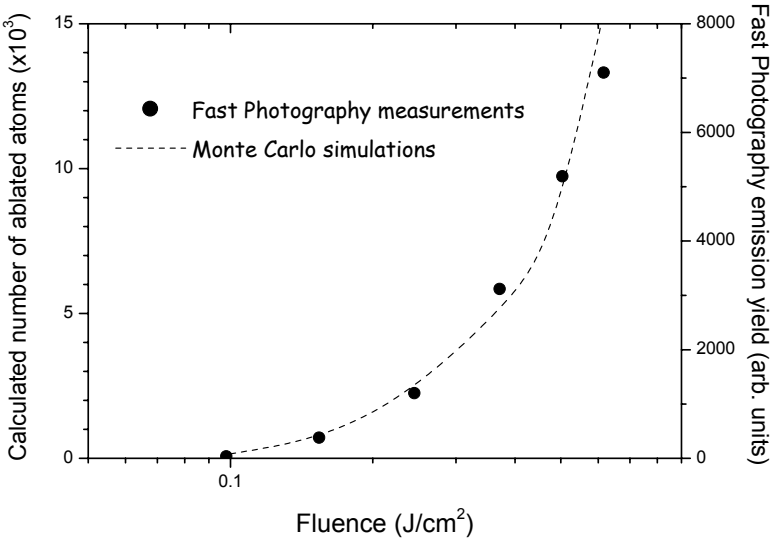

Fig. 4.7: Fluence dependence of the MC simulated ablation yield. Comparison with the experimental results for the emission yield from fast photography measurements.

As clearly shown, the agreement between the simulation and the experimental data is very satisfactory. In particular, both the measured ablation threshold for Nickel ($\approx$ 0.08 J/cm^2) and the double logarithmic regime are well reproduced, thus confirming the soundness of the developed MC simulation.

IV.2.2 Thermodynamic pathways of the expanding ablated plume

In this subsection, the results of the MC simulation about the spatial energy distribution inside the bulk material as a consequence of the ultrashort laser irradiation are used to study the subsequent thermodynamic relaxation of specific areas of the target during plume expansion.

As we already observed in sections I.2 and throughout the present chapter, irradiation of a solid by high intensity ultrashort laser pulses can heat a surface layer to temperatures even larger then the material critical temperature, T_{cr}, while keeping its solid-state density. The heated layer, then, experiences an adiabatic expansion (AE) at larger times. A liquid-vapour Van der Waals-like phase-diagram is reported in Fig. 4.8 for nickel in density-temperature (ρ, T) variables, where the isochoric heating due to laser irradiation is indicated by the vertical dashed line and AE paths for various initial temperatures are drawn as dashed lines.

The adiabatic expansion starting from the solid state density can be approximately described with the density-dependent Grüneisen coefficient[19] Γ, and reads

$$T = T_0 \left(\rho/\rho_0\right)^{\Gamma(\rho)} \qquad (2)$$

where T and ρ are the temperature and density of the expanding material, and the index 0 indicates the starting value of the variables. A good approximation of Γ for metals is $\Gamma \approx 2\ (\rho/\rho_0)$ at $\rho_0/3 < \rho < \rho_0$, while $\Gamma \to 2/3$ for $\rho << 1$ (ideal gas)[19]. For the sake of estimation here we consider $\Gamma \approx 2/3$ for $\rho \leq \rho_0/3$. Thus the adiabatic paths are obtained by joining the two behaviours at just $\rho \approx \rho_0/3$.

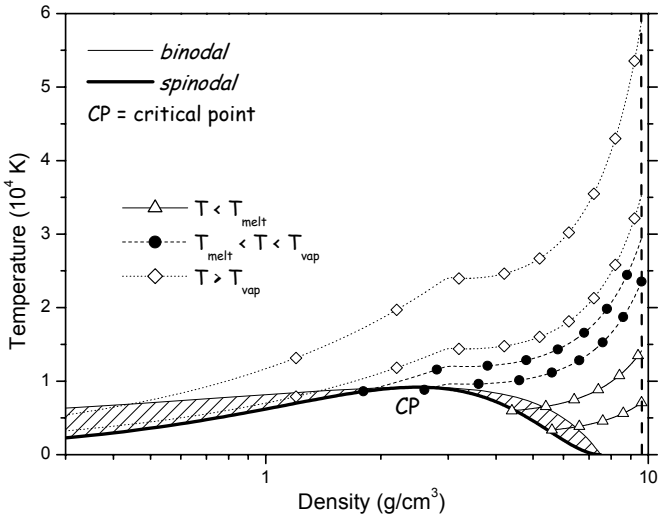

Fig. 4.8: Liquid-vapour phase-diagram in (ρ - T) coordinated for nickel. The solid lines show the binodal and spinodal boundaries, respectively. The point-lines represent AE pathways starting at the different initial temperatures. Three different relaxation regimes are shown, according to the values of the final temperature T_0 reached after absorption of the laser light with respect to the melting (T_m=1726) and the boiling (T_{vap}=3187) point of nickel. See the text for further details.

Along with the discussion reported in section I.2 in chapter I, three different relaxation regimes can be distinguished, according to the values of the starting temperature T_0 reached after absorption of the laser light, with respect to the melting and the boiling points of nickel. Actually, AE paths starting at $T < T_m$ reach the binodal line far from the thermodynamic critical point CP, then crossing the spinodal at supercritical densities during the expansion; in this case, resolidification and/or mechanical ablation (spallation) can occur. AE paths starting at T_m

< T < T_{vap} intersect the binodal and the spinodal lines very close to the critical point thus leading to nucleation and fragmentation processes. Finally, paths starting at T > T_{vap} pass above the critical point and never cross the spinodal line thus leading to material vaporization.

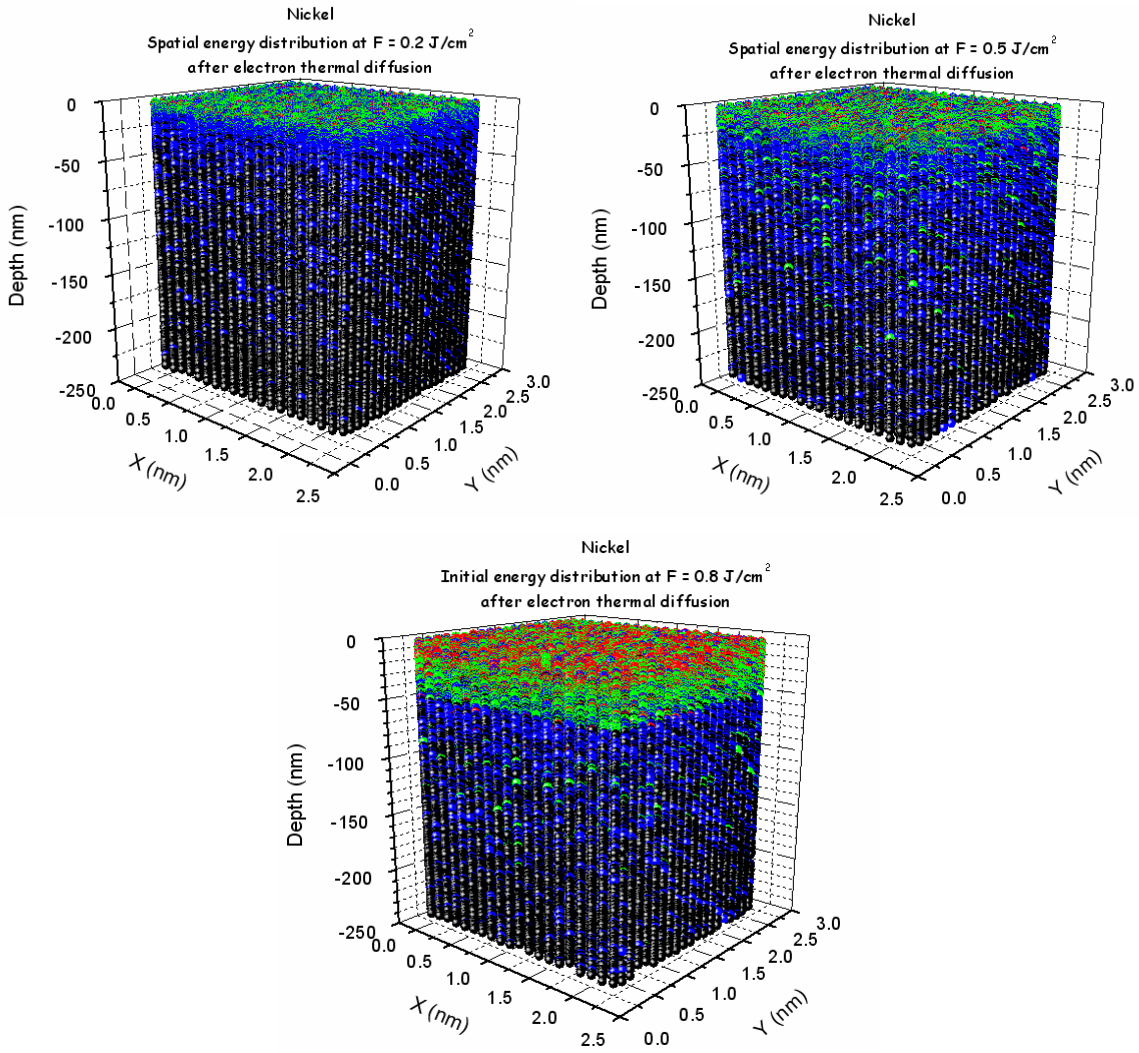

Fig. 4.9: Spatial energy distributions inside the bulk material after the laser irradiation at 0.2, 0.5 and 0.8 J/cm^2. Red dots undergo direct vaporization. Green dots are subjected to phase explosion and/or fragmentation mechanisms, while blue dots experience resolidification or spallation. Finally, black dots represent unaffected atoms.

These arguments can be used to follow and predict the relaxation paths of selected areas of the target and, thus, to argue the occurrence of different mechanisms affecting the material morphology and evolution. In fact, the knowledge of the energy spatial distribution inside the bulk material after the laser irradiation calculated through the MC technique allows to follow selectively the thermodynamic relaxation of material layers placed at different depths. Fig. 4.9 reports the pictures of the energy spatial distribution for three laser fluences of 0.2, 0.5 and 0.8

J/cm^2, respectively, where different relaxation mechanisms are single out as a function of depth. Here, red dots undergo direct vaporization; green dots are subjected to phase explosion and/or fragmentation mechanisms, while blue dots experience resolidification or spallation. Finally, black dots represent unaffected atoms. As clearly shown in the figure, only a shallow region under the surface will undergo direct vaporization, ranging from about the optical skin depth (≈ 8 nm) at 0.2 J/cm^2 to a value about three times higher at 0.8 J/cm^2. The same happens also for the region believed to lead to nanoparticles formation (green dots), which at the higher investigated fluence extends up to about 50 nm. At all the investigated fluences, most of the excited atoms will undergo resolidification (blue dots); notwithstanding, at high fluences these atoms may experience spallation-like ablation as a consequence of the mechanical stresses induced by the laser irradiation. The corresponding ablation depths (as about the sum of the vaporization depth and the phase explosion/fragmentation depth) are quite in agreement with both the numerical[20] and experimental[21] values reported in the literature.

We are not able at the moment to simulate also the expansion stage of ultrashort laser ablation to fully explain the complexity of processes occurring after laser energy delivery. In particular, it is not possible to fully single out the right mechanisms which are responsible of nanoparticles production (for instance, we cannot distinguish between phase explosion and fragmentation). Nevertheless, the possibility of well calculate the spatial energy distribution inside the irradiated target could be of great usefulness not only to reproduce some experimental results but also to move future experimental investigations for a complete understanding of all the mechanisms involved in ultrashort pulsed laser ablation.

References

[1] D. Perez and L. J. Lewis, Phys. Rev. Lett. 89, 255504-1 (2002); and Phys. Rev. B 67, 184102 (2003)

[2] S. Eliezer, N. Eliaz, E. Grossman, D. Fisher, I. Gouzman, Z. Henis, S. Pecker, Y. Horovitz, M. Fraenkel, S. Maman, Y. Lereah, Phys. Rev. B 69, 144119 (2004).

[3] S. Amoruso, R. Bruzzese, M. Vitiello, N. N. Nedialkov, and P. A. Atanasov, J. Appl. Phys. 98, 044907 (2005).

[4] M. P. Allen and D. J. Tildesley, *Computer Simulation of Liquids* (Clarendon, Oxford, 1987), pp. 71–108.

[5] I. A. Girifalco and V. G. Weizer, Phys. Rev. 114, 687 (1959).

[6] C. Schäfer, H. M. Urbassek, L. V. Zhigilei, and B. J. Garrison, Comput. Mater. Sci. 24, 421 (2002).

[7] V. Schmidt, W. Husinsky, and G. Betz, Appl. Surf. Sci. 197–198, 145 (2002).

[8] K. Dou, E. T. Knobbe, R. L. Parkhill, B. Irwin, L. Matthews, and K. H. Church, Appl. Phys. A 76, 303 (2003).

[9] D. von der Linde and K. Sokolowski-Tinten, Appl. Surf. Sci. 154–155, 1 (2000).

[10] F. Vidal, T. W. Johnston, S. Laville, O. Barthélemy, M. Chaker, B. Le Drodoff, J. Margot, and M. Sabsabi, Phys. Rev. Lett. 86, 2573 (2001).

[11] S. Nolte, C. Momma, H. Jacobs, A. Tünnermann, B. N. Chichkov, B. Wellegehausen, and H. Welling, J. Opt. Soc. Am. B 14, 2716 (1997).

[12] M. Vitiello, S. Amoruso, C. Altucci, C. de Lisio, X. Wang, *Appl. Surf. Sci.* 248, 163 (2005).

[13] F. James, Rep. Prog. Phys. 43, 1145 (1980).

[14] *CRC Handbook of Chemistry and Physics*, D.R. Lide Editor, CRC Press (1994).

[15] B. N. Chichkov, C. Momma, S. Nolte, F. von Alvensleben, A. Tünnermann, Appl. Phys. A 63, 109 (1996).

[16] A. P. Kanavin, I. V. Smetanin, V.A. Isakov, Yu. V. Afanasiev, B. N. Chichkov, B. Wellegehausen, S. Nolte, C. Momma and A. Tünnermann, Phys. Rev. B 57, 14698 (1998).

[17] D.A. Papaconstantopoulos, Handbook of the Band Structureof Elemental Solids, Plenum Press, New York, 1986.

[18] E.G. Gamaly, A.V. Rode, O. Uteza, V. Kolev, B. Luther-Davies, T. Bauer, J. Koch, F. Forte and B. N. Chichkov, J. Appl. Phys. 95, 2250 (2004).

[19] Ya. B. Zel'dovich and Yu. P. Raizer, *Physics of Shock Waves and High-Temperature Hydrodynamic Phenomena* (Academic, New York, 1966).

[20] P.A. Atanasov, N.N. Nedialkov, S.E. Imamova, A. Ruf, H. Hügel, F. Dausinger and P. Berger, Appl. Surf. Sci. 186, 369 (2002).

[21] S. Preuss, A. Demchuk and M. Stuke, Appl. Phys. A 61, 33 (1995).

CONCLUSIONS

The process of laser ablation generated by high intensity, ultrashort laser pulses (≈ sub-picosecond duration) has been investigated by both experimental and numerical techniques. Optical Emission Spectroscopy as well as Fast Photography measurements reveal the presence in the ultrashort laser ablated plume of three different populations: high energy ions, atoms and nanoparticles. The latter are characterized by featureless blackbody-like emission spectra; by fitting them through a Planck's-like radiation law, the spatial and temporal evolution of the nanoparticles temperature was obtained. Nanoparticles turned out to be cooler (few $\approx 10^3$ K) than atoms (typically few $\approx 10^4$ K) and to cool down while expanding essentially by radiative emission.

Optical measurements allowed also to investigate the mechanisms of nanoparticles formation, by studying the fluence dependence of the optical emission yield. Then, nanoparticles turned out to be ejected from the target material at all the investigated fluences and, in particular, also under the threshold for atomic ablation (the fluence value for atoms ejection). This feature is an indirect confirm that nanoparticles are ejected directly from the target material, in vacuum, and are not the consequence of in-flight condensation mechanisms as in the case of nanosecond laser ablation, where nanoparticles are produced as a result of the plume expansion into an inert gas atmosphere. These features strongly underline the absolute newness of the nanoparticles formation mechanisms with respect to the well known ejection processes occurring during laser ablation experiments. In fact, while atoms are ejected as a consequence of energy exchange on a timescale of typically few tens of picoseconds (ps), the threshold for nanoparticles ejection is very close to the value for surface damaging to occur, as a consequence of the extreme, non-equilibrium conditions set in by the laser irradiation on a timescale of typically few ps. Thus, at the lower investigated fluences, nanoparticles are likely to be produced as a consequence of the strong stresses induced by the laser irradiation inside the target material (mechanical ablation). Notwithstanding, at higher fluences several others mechanisms could be simultaneously effective (phase explosion, fragmentation and so on) as a result of the spatial energy distribution inside the bulk material after the laser irradiation, as clearly shown by our Monte Carlo simulations: the energy absorbed into the material skin depth is then redistributed by electron thermal diffusion mechanisms inside the bulk solid, thus leading to a final spatial energy distribution exponentially decreasing with depth.

Therefore, atomic layers placed at different depths will be charged of a different amount of energy and the subsequent relaxation paths may lead to material ablation through several, different processes.

Atomic Force Microscopy confirmed the *nanometric* character of the produced aggregates, with limited sizes (≈ 10-20nm) and quite narrow size distributions, thus suggesting the occurrence of extremely new and unexplored mechanisms in laser ablation; in fact, non atomic features are typically observed during nanosecond (ns) laser ablation as liquid droplets of *micrometric* dimensions coming directly from the melted surface material as a result of an equilibrium phase transition from the solid to the liquid and, then, to the vapour state.

This also suggests the occurrence in ultrashort laser ablation of non equilibrium phase transitions: the system is heated by the laser light at almost the solid density to temperatures very close or higher than the thermodynamic critical point; then it relaxes very fast through adiabatic expansion thus undergoing a phase decomposition into a mixture of ions, atoms and nanoparticles. Molecular Dynamics simulations finely reproduced this phenomenology, thus predicting the presence of nanoparticles in the ultrashort laser ablated plumes as a result of the extreme conditions to which the material is brought by the high intensity laser irradiation.

All these features turned out to characterize ultrashort laser ablated plumes disregarding the particular target material and the specific laser parameters (as laser fluence, wavelength and pulse duration) employed, thus suggesting ultrashort pulsed laser ablation in vacuum as a powerful and versatile technique to produce nanoparticles of limited sizes and size dispersion from practically any target material. These observations directly confirmed an almost unchanged phenomenology when using laser systems of pulse durations shorter than about few ps, the time for the electron to the lattice subsystems energy exchange; they all belong to the "ultrashort" laser regime.

Langmuir Probe as well as optical techniques revealed also the presence in the ultrashort laser ablated plume of high energy ions with average kinetic energies of several keV, in contrast with the tens of eV typically possessed by ions ejected during ns laser ablation, as a further confirm of the extreme newness of the ablation process in the ultrashort laser-matter interaction regime.

Thus, the main features of ultrashort laser ablation plumes have been studied by means of several experimental techniques and numerical methods. A wide experimental and theoretical characterization of the plume properties and dynamics has been performed on a variety of different target materials and for three different ultrashort laser systems, with particular

attention to the main features of the nanoparticles phase. Ultrashort laser ablation turned out to be an extreme versatile technique to produce nanoparticles from any target material, in vacuum, without further material or plume processing thus appearing as an extremely interesting deposition technique for technological applications in the field of nanoscience.

APPENDIX A

Magnetic films of nanoparticles by ultrashort pulsed laser deposition

In order to explore the potentiality of ultrashort laser ablation as a powerful and versatile technique for applications in the field of nanotechnologies, we realized films of nanoparticles (NPs) from magnetic materials (Ni, Fe, and $Tb_{0.3}Dy_{0.7}Fe_2$ named "Terfenol-D") to study the structural and magnetic properties as a consequence of their nanogranularity. These studies were all performed in collaboration with the group directed by Prof. Luciano Lanotte, of the University of Naples "Federico II". Here, we briefly review the main results of our investigation performed so far (see ref. 1, 2, 3 and refs therein cited).

Films were produced by collecting the ablated material onto substrates located about 30 mm away from the target surface and hold at room temperature, after a suitable deposition time (according to the desired film thickness). The morphology of the deposited films was studied by atomic force microscopy (AFM). The AFM images were acquired in tapping mode (scan rate 1 Hz, scan size 1 μm) by using a sharpened silicon tip with a radius of less than 5 nm. In particular, less than one layer deposits on freshly cleaved mica substrates were considered to measure the sizes of the NPs produced during the femtosecond ablation process, while the size of the NPs in the aggregate film were obtained by AFM analysis of the film surface at different stages of the deposition process. The structural analysis of the deposited films was performed by X-ray diffraction (XRD), while the magnetic properties were characterized by a vibrating sample magnetometer at a vibration frequency of 55 Hz, and a fixed temperature of 300 K.

The theoretical and experimental interest around the production and characterization of magnetic nanoaggregates is strictly linked to the possibility of controlling their macroscopic magnetic properties through particles size and density tailoring. In fact, it is possible to fabricate magnetic materials made of isolated nanoparticles behaving as single magnetic domains, as well as of densely packed clusters with magnetic properties governed by the reciprocal exchange. Among magnetic nanomaterials, nanoparticles films form an important class of materials for applications in magnetic storage media and modern electromagnetic devices.

The first interesting feature evidenced by AFM analysis was the nanogranularity of the produced film. Nanoparticles turned out to retain their morphology, without merging each other to yield a "bulk" film of the deposited material. This feature is clearly shown in Fig. A.1, where the AFM images of both dispersed nanoparticles and a film of nanoparticles deposited in

the same conditions are reported, respectively, in the case of nickel. Here the deposits were carried out at a laser fluence of about 0.4 J/cm^2 and a repetition rate of 33Hz.

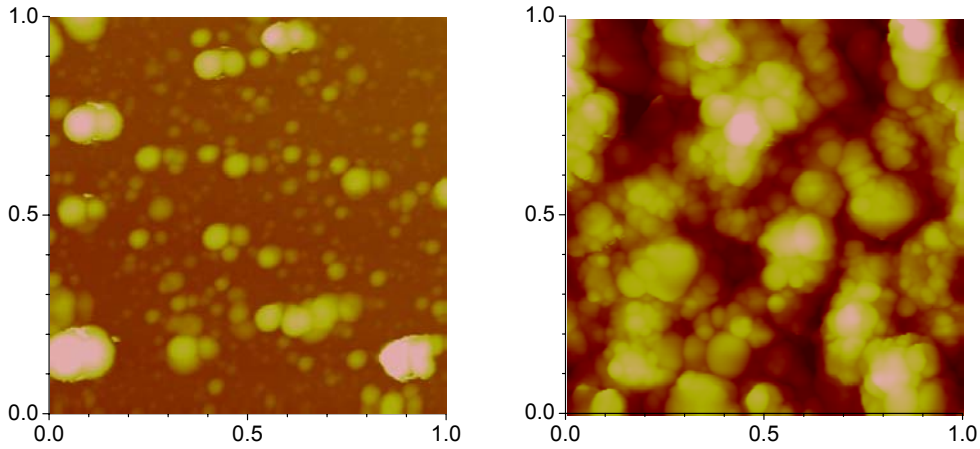

Fig. A.1: AFM images of nickel nanoparticles: (a) less than one layer deposit; (b) film.

Panel A.1(a) shows a large number of disperse NPs and some islands where NPs have stuck together. For less than one layer samples, the sizes of the isolated NPs range from few nm to tens of nm. Panel A.1(b) refers to a film of NPs with a thickness of ≈350 nm. The density of NPs in the film appears rather large, with most individual NPs sticking to one another. However, where the NPs density is thinner, it is possible to observe and measure the size of individual particles, which results fairly similar to those obtained for isolated NPs in less than one layer deposits. Similar images were obtained for thinner and thicker films, indicating a good uniformity of the morphology in the volume of the deposit. Similar results have been obtained in the case of iron and terfenol. Therefore, we can conclude that the basic structure of the film deposited by ultrashort laser ablation in vacuum, and at room temperature, is that of a cauliflower-like, granular agglomerate of nanoparticles sticking each other while maintaining their own individuality.

XRD technique allowed the investigation of the structural properties of the deposited nanoagglomerates. X-ray diffraction spectra obtained from nanogranular films of NPs in the case of nickel and iron clearly present diffraction peaks located in positions consistent with those expected for the elemental target material. This indicates that the film is composed mostly of random oriented crystallites.

These features lead to unique magnetic properties of the deposited film, as it clearly turns out in the case of nickel where the nanogranular samples showed very interesting features as

compared with bulk nickel or with a sample of dispersed nanoparticles embedded in a silicone matrix.

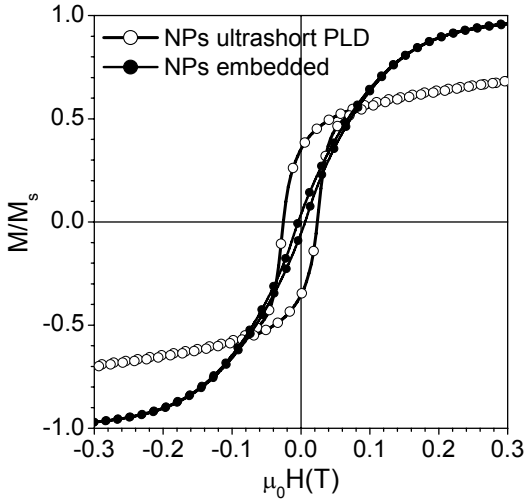

Fig. A.2: Hysteresis curves for a film of nanoparticles produced by ultrashort laser ablation (open circles) and a sample of nanoparticles embedded in a silicone matrix.

As clearly shown in Fig. A.2, the hysteresis curve of the nanoparticles film is characterized simultaneously by a greater coercitive field and an higher remanence ratio, which make them particularly attractive for nanodevice applications. These features have been correlated to the peculiar shape anisotropy of the constituent nanoparticles, and to their strong preferential orientation. We ascribed the very interesting magnetic properties of the fs PLD films to these anisotropies and to the occurrence of a size-dependent tensile stress anisotropy brought about by the specific fs laser deposition technique.

All these findings clearly underline the extreme powerfulness of ultrashort pulsed laser deposition in vacuum as a technique to synthesize materials with absolutely new and unique structural and transport properties. Further investigations on both magnetic and non-magnetic materials are currently going on to fully explore all the potentiality of the technique.

References

[1] Ausanio G., Barone A.C., Iannotti V., Lanotte L., Amoruso S., Bruzzese R., Vitiello M., *Appl. Phys. Lett.* 85, 4103 (2004).

[2] G. Ausanio, A. Barone, V. Iannotti, L. Lanotte, S. Amoruso, M. Vitiello, P. Scardi and M. D'Incau, *"Morphology, structure and magnetic properties of* $(Tb_{0.3}Dy_{0.7}Fe_2)_{100x}$ Fe_x *nanogranular films produced by ultrashort pulsed laser deposition"*, accepted for publication in *Nanotechnology* (2005).

[3] S. Amoruso, G. Ausanio, C. de Lisio, V. Iannotti, M. Vitiello, X. Wang, L. Lanotte, *Appl. Surf. Sci.* 247, 71 (2005).